UC San Diego

UC San Diego Electronic Theses and Dissertations

Title

Sensing and Rendering in Human-Machine Interfaces for Biomedical Applications

Permalink

https://escholarship.org/uc/item/2k94676j

Author

Becerra, Laura Lynn

Publication Date

2024

Peer reviewed|Thesis/dissertation

eScholarship.org Powered by the California Digital Library
University of California

UNIVERSITY OF CALIFORNIA SAN DIEGO

Sensing and Rendering in Human-Machine Interfaces for Biomedical Applications

A dissertation submitted in partial satisfaction of the
requirements for the degree Doctor of Philosophy

in

Electrical Engineering (Medical Devices and Systems)

by

Laura Lynn Becerra

Committee in charge:

Professor Tse Nga Ng, Chair
Professor Darren Lipomi, Co-Chair
Professor Patrick Mercier
Professor Tania Morimoto
Professor Romke Rouw

2024

Copyright

Laura Lynn Becerra, 2024

All rights reserved.

The Dissertation of Laura Lynn Becerra is approved, and it is acceptable in quality and form for publication on microfilm and electronically.

University of California San Diego

2024

DEDICATION

To my sister Alex, who is not only my sibling but my best friend—thank you. Throughout the roller coaster journey of my PhD, your unwavering support and trust have been my anchors. Your love and understanding made the difficult moments more bearable and I was always reminded that everything would be okay. This accomplishment, while mine in name, is ours in spirit. I am so grateful for your love and companionship on this journey and always.

EPIGRAPH

Imagine all the people
Sharing all the world
You may say I'm a dreamer
But I'm not the only one
I hope someday you'll join us
And the world will live as one

John Lennon

TABLE OF CONTENTS

Dissertation Approval Page iii

Dedication iv

Epigraph v

Table of Contents vi

List of Figures viii

List of Tables x

Acknowledgements xi

Vita xiii

Abstract of the Dissertation xv

Introduction 1

Chapter 1 Bidirectional Venturi Flowmeter Based on Capacitive Sensors for Spirometry 6
1.1 Introduction 6
1.2 Experimental Section 9
1.2.1 Spirometer Design 9
1.2.2 Sensor Fabrication Materials 13
1.2.3 Sensor Fabrication 13
1.2.4 Spirometer Tube Fabrication 15
1.2.5 Ethical Committee Approval 15
1.3 Results and Discussion 15
1.3.1 Characterization and Calibration of Capacitive Sensor 15
1.3.2 Simulations of Respiratory Flow Rate Characteristics through Finite Element Analysis 17
1.3.3 Breathing Tests 21
1.4 Conclusion 25
1.5 Acknowledgements 26

Chapter 2 Decoupling Coldness and Softness in Tactile Wetness Perception using Tunable Hydrogels 28
2.1 Introduction 28
2.1.1 Touch perception of heat extraction rates 32
2.1.2 Softness/compliance of materials 33
2.2 Results 36
2.2.1 Sample design and characterization 36

2.2.2 Psychophysical studies . . . 39
2.3 Methods . . . 43
2.3.1 Hydrogel synthesis . . . 43
2.3.2 Hydrogel characterization . . . 44
2.3.3 Psychophysical experimental design . . . 46
2.4 Discussion . . . 47
2.5 Acknowledgements . . . 49

Chapter 3 Enhanced Dye-Sensitized Mechanosensation utilizing Pulsed and Digitally Modulated Light . . . 50
3.1 Introduction . . . 50
3.1.1 The photoacoustic effect . . . 50
3.1.2 Tactile perception and articulation . . . 52
3.2 Results . . . 55
3.2.1 Psychophysical experimental design . . . 55
3.2.2 Miniature diode laser (MDL) experiments . . . 59
3.2.3 Incoherent light experiments . . . 62
3.3 Discussion . . . 65
3.4 Conclusion . . . 68
3.5 Experimental Section . . . 69
3.5.1 Psychophysical design . . . 69
3.5.2 Characterization . . . 77
3.6 Acknowledgements . . . 80

Appendix A Appendix . . . 81
A.1 Chapter 1 Supplementary Information . . . 81
A.2 Chapter 2 Supplementary Information . . . 89
A.3 Chapter 3 Supplementary Information . . . 92

Bibliography . . . 100

LIST OF FIGURES

Figure 1. Layers in Engineered Material Perception 3

Figure 1.1. Spirometer Overview 10

Figure 1.2. Capacitive Sensor Characterization 16

Figure 1.3. Device Geometry and Flow Simulations 18

Figure 1.4. Pressure and Simulation Scaling Factors 20

Figure 1.5. Respiratory Airflow Output 22

Figure 1.6. Summary of Respiration Measurements 23

Figure 2.1. Wetness Study Overview 31

Figure 2.2. Hydrogel Characterization 35

Figure 2.3. Transitivity and Bradley-Terry Ability Scores 39

Figure 2.4. Wetness Judgement Prediction Model 41

Figure 3.1. Photoacoustic Mechanosensation Overview 53

Figure 3.2. Optical Parametric Oscillator (OPO) Laser Experiment Results 56

Figure 3.3. Mechanically-Chopped Light Experiment Results 60

Figure 3.4. Digitally-Chopped Laser and Incoherent Light Experiment Results 63

Figure 3.5. Absorbance and Thermography Characterization Data 64

Figure A.1. Sensor Performance with Humidity Exposure 82

Figure A.2. Sensor Response Time 83

Figure A.3. Flow Rate Adjustment 85

Figure A.4. Spirometer Fluid Density from Simulation 86

Figure A.5. Flow Rate Scale Factor 87

Figure A.6. Hydrogel Thickness Measurements 89

Figure A.7. Hydrogel Porosity 90

Figure A.8. Thermal Conductivity Pilot Experiment Results 90
Figure A.9. Skin-Hydrogel Temperature Curves 91
Figure A.10. Function-fitted Skin-gel Temperature Curves 91
Figure A.11. OPO Audio Pulses 92
Figure A.12. Psychophysical Experiment Design Flowcharts 93
Figure A.13. Photographic and Optical Microscopy of Spin-cast Dye Films 94
Figure A.14. Photographic and Absorbance Spectrum representations of Black Ink 95
Figure A.15. Digital Light Processing (DLP) Projector Green Light Absorbance Spectra 95
Figure A.16. Handheld Chopper Photos and Schematics 96
Figure A.17. Chopped Miniature Diode Laser (MDL) Light Detection Accuracy 97
Figure A.18. OPO Laser Power Pulse Signal 97

LIST OF TABLES

Table 2.1. Stock Solution Concentrations for Hydrogel Synthesis 43

Table A.1. Commercial Peak Flow Meter Data 84

Table A.2. Simulation Values of FEA Differential Pressure Peaks 86

Table A.3. Exp. C: General Linearized Mixed Model (GLMM) Results 98

Table A.4. Exp. C: GLMM Estimated Marginal Means (EMMs) of Each Condition . . . 98

Table A.5. Exp. E: GLMM Estimated Marginal Means (EMMs) of Each Condition . . . 98

Table A.6. Exp. F (Mechanically chopped): GLMM Estimated Marginal Means (EMMs) of Each Condition 99

Table A.7. Spin-cast Dye Film Thicknesses Obtained by Ellipsometry 99

Table A.8. OPO Laser Beam Area 99

ACKNOWLEDGEMENTS

I would like to acknowledge Professors Tse Nga Ng and Darren Lipomi for their support as my advisors and as the co-chairs of my committee. Their guidance and advice throughout my program has been invaluable.

I would also like to acknowledge my colleagues in the Ng lab and Lipomi lab, especially Tarek Rafeedi, without whom my research would have no doubt taken five times as long. I am incredibly lucky to have been working alongside such funny and supportive colleagues/friends.

I would like to acknowledge the various sources of funding throughout my program. Specifically, the National Science Foundation Graduate Research Fellowship Program, the Achievement Rewards for College Scientists (ARCS) San Diego chapter, and UC San Diego for my first-year fellowship and for the UC San Diego Dissertation Year Fellowship.

Lastly, I would be remiss without thanking my friends and family who have always believed in my success and whose support means the world. I am extremely grateful for their constant love and words of encouragement. My parents have always supported my academic and personal flourish, and for that I am grateful. I would especially like to thank my sister, Alex, who has been my rock and my best friend throughout my entire journey.

The Introduction, in part, contains material that will be submitted for publication as it may appear in Accounts of Materials Research, 2024, Becerra, Laura L.; Lipomi, Darren J. The dissertation author was the primary investigator and author of this paper.

Chapter 1, in full, is a reprint of the material as it appears in Advanced Materials Technologies 2023, vol. 8, Becerra, Laura L.; Rafeedi, Tarek; Ramanarayanan, Sankaran; Frankel, Ian; Miller, Juliana; Chen, Alexander X.; Qie, Yi; Lipomi, Darren J.; Garudadri, Harinath; Ng, Tse N. The dissertation author was the primary investigator and author of this paper.

Chapter 2, in full, has been submitted for publication of the material as it may appear in Nature Human Behaviour, 2024, Becerra, Laura L.; Root, Nicholas; Clark, Ainsley; Rafeedi, Tarek; Brown, William; Chen, Alexander X.; Qie, Yi; Blau, Rachel; Miller, Juliana; Kapadia,

Kabir, Ng, Tse Nga; Rouw, Romke; Lipomi, Darren J. The dissertation author was the primary investigator and author of this paper.

Chapter 3, in full, has been submitted for publication of the material as it may appear in Advanced Science, 2024, Rafeedi, Tarek*; Becerra, Laura L.*; Root, Nicholas; Qie, Yi; Brown, William; Qi, Baiyan; Fu, Lei; Esparza, Guillermo; Sasi, Lekshmi; Kapadia, Kabir; Rouw, Romke; Jokerst, Jesse; Lipomi, Darren J. The dissertation author was one of the co-primary investigators and author of this paper, along with Tarek Rafeedi.

VITA

2019	Bachelor of Science/Bachelor of Arts, University of San Diego
2021	Master of Science, University of California San Diego
2024	Doctor of Philosophy, University of California San Diego

PUBLICATIONS

L.L. Becerra, N. Root, A. Clark, T. Rafeedi, W. Brown, A.X. Chen, Y. Qie, R. Blau, J. Miller, K. Kapadia, T.N. Ng, R. Rouw, D.J. Lipomi, "Decoupling Coldness and Softness in Tactile Wetness Perception using Tunable Hydrogels," Nature Human Behaviour, Submitted.

T. Rafeedi*, L.L. Becerra*, N. Root, Y. Qie, W. Brown, B. Qi, L. Fu, G. Esparza, Y. Qie, L. Sasi, R. Rouw, J. Jokerst, D. Lipomi, "Enhanced Dye-sensitized Mechanosensation utilizing Pulsed and Digitally Modulated Light," Advanced Science, Submitted.

R. Blau, A. Abdal, A.X. Chen, Y. Qie, T. Rafeedi, L.L. Becerra, T. Kim, N. Root, D.J. Lipomi. "Conformable Conductive PEDOT-based Electrode for Tunable Tactile Perception." Science Robotics, Under Revisions.

N. Vreugdenhil, E.H.F. de Haan, N. Root, L.L. Becerra, D.J. Lipomi, R. Rouw, "Exploring Touch-Colour Associations in Achromatopsia: A Case Study," Cortex, Submitted.

E.H. Shinn, A.S. Garden, S.K. Peterson, D.J. Leupi, M. Chen, L.L. Becerra, T. Rafeedi, J. Ramirez, D. Rodriguez, F. VanFossen, S. Zehner, E. Kamunyo, P. Mercier, J. Wang, K. Hutcheson, E. Hanna, D.J. Lipomi. "Iterative patient testing of a stimuli-responsive swallowing activity sensor to promote extended user engagement during the first year after radiation," JMIR Cancer, 2024.

L.L. Becerra, T. Rafeedi, S. Ramanarayanan, I. Frankel, J. Miller, A.X. Chen, Y. Qie, D.J. Lipomi, H. Garudadri, T.N. Ng, "Bidirectional Venturi Flowmeter Based on Capacitive Sensors for Spirometry," Advanced Materials Technologies, 2023.

B. Polat, T. Rafeedi, L.L. Becerra, A.X. Chen, K. Chiang, V. Kaipu, R. Blau, P.P. Mercier, C.K. Cheng, D.J. Lipomi. "External Measurement of Swallowed Volume During Exercise Enabled by Stretchable Derivatives of PEDOT:PSS, Graphene, Metallic Nanoparticles, and Machine Learning," Advanced Sensor Research, 2023.

R. Blau, A.X. Chen, B. Polat, L.L. Becerra, R. Runser, B. Zamanimeymian, K. Choudhary, D.J. Lipomi. "Intrinsically Stretchable Block Copolymer Based on PEDOT:PSS for Improved Performance in Bioelectronic Applications," ACS Applied Materials & Interfaces, 14, p. 4823-4835,

2022.

B. Polat, L.L. Becerra, P. Hsu, V. Kaipu, P.P. Mercier, C. Cheng, D.J. Lipomi. “Epidermal Graphene Sensors and Machine Learning for Estimating Swallowed Volume,” ACS Applied Nano Materials, 4, p. 8126-8134, 2021.

ABSTRACT OF THE DISSERTATION

Sensing and Rendering in Human-Machine Interfaces for Biomedical Applications

by

Laura Lynn Becerra

Doctor of Philosophy in Electrical Engineering (Medical Devices and Systems)

University of California San Diego, 2024

Professor Tse Nga Ng, Chair
Professor Darren Lipomi, Co-Chair

The disparity in healthcare access is a large issue in medical deserts, where essential medical resources are distant from the communities they serve. This dissertation advances human-machine interfaces (HMIs) in biomedical applications to facilitate remote medical diagnosis and treatment. The first study is a bi-directional spirometer with flexible capacitive sensors for cost-effective, remote respiratory monitoring. This point-of-care device made of a 3D-printed

tube interfacing with the user's mouth and its airflow, successfully measured tidal and deep breathing signals, and highly accurate peak expiratory flow rates compared with commercial device readings.

To enhance the efficacy of virtual healthcare, this work also refines haptic feedback in telemedicine platforms to achieve realistic touch sensations that improve the immersion and accuracy of remote healthcare technologies. It includes a study on wetness perception using a tunable organic hydrogel, achieving a 90% prediction model for human wetness judgment. The results identified that the most effective metrics for high prediction accuracy were those that were the most human-adjacent and enabled the creation of a perceptual space capable of seven distinct levels of wetness. The study demonstrates that the physical characteristics at the skin-stimulus interface are sufficient for simulating wetness without reliance on specific material types.

Additionally, the dissertation investigates contact-free haptic stimulation using thermoelastic and photoacoustic effects. By applying a thin dye layer to the skin, the study demonstrated significant enhancements in the perception of different pulsed light sources, varying in wavelength and pulse width. Notably, it achieved robust tactile stimulation using incoherent light from a commercial Digital Light Processing (DLP) projector. Across all sources, vibration was the predominant felt sensation at the two tested locations: the distal phalanx (i.e., fingertip, 55.21-57.29%) and the proximal phalanx (41.67-44.79%). This contact-free haptic stimulation modality enables convenient, effective transmission of haptic information to human users, potentially at great distances. Collectively, the innovations in this dissertation contribute to the development of virtual technology platforms that enable and enhance remote healthcare delivery.

Introduction

Healthcare disparities are a large issue for communities that are far from healthcare facilities. These communities, called medical deserts [1], primarily affect individuals of low socioeconomic status. Large distances to healthcare facilities require long bouts of travel which are difficult for those who need to work or do not have the financial means to do so. As the recent COVID-19 pandemic demonstrated, public access to medical equipment can be very limited when the global healthcare system is under stress. Reduced availability of equipment are caused by supply-chain issues and the added caveat of in-person visits restricted to those who require immediate treatment to contain illness transmission.

To mitigate the supply chain constrictions in healthcare, point-of-care (POC) devices can be used as an alternative to in-person doctor visits for monitoring and diagnosing conditions and illnesses while at home. A critical aspect in patient monitoring and diagnosis is the use of sensor technologies to transduce physiological signals into electronic data [2]. Flexible sensors, in particular, have emerged as an optimal choice in sensor diagnostic tools as they allow for conformability and versatile use for patient monitoring, especially in wearable devices. In this dissertation thesis, I developed a low-cost portable spirometer device using custom flexible capacitive sensors to measure respiratory activity in humans. Aside from its financial affordability, the device does not have any moving parts that require regular cleaning, and does not require extensive calibration making it easy to use for naive individuals. Unlike most cheap at-home spirometers, this device is capable of measuring respiration flow in both directions (inhalation and exhalation), providing more comprehensive diagnostics not currently done in other POC devices.

Another solution to increasing access to medical resources, is through expanding the use of virtual healthcare. Alternatives to in-person doctor visits, such as remote visits or teleoperations, provide another option for patients to receive care without physically being present with a physician. Virtual care has additional advantages, as it also proves useful in platforms for surgical training simulations and other medical skill assessment platforms. Virtual technology for such important medical applications requires effective transmission of haptic information to its users. For example, if a surgeon is required to use mechanical cues to properly tie a suture on a human body remotely, a stiff robotic device would remove realistic physical cues. Inadequate haptic feedback reduces the consistency, precision, comfort, and immersion of the operation experienced by the surgeon.

Haptic materials, and their physical properties, are crucial for realistically conveying sensory information to its users. The first step in developing material interfaces is understanding how the human brain perceives certain material properties and how they are interacted with. The best suite of tools to explore this area is the field of psychophysics, which studies the relationship between stimuli and the perceived sensation [3]. More specifically, psychophysical experiments can be designed to explore detection limits, accuracy, and discrimination thresholds of samples with different properties. Materials engineering allows for tuning of bulk and surface properties, whether it's through changes in chemical synthesis, microstructure architecture, or conductive properties of materials. Combining insights from psychophysical analyses with the study of haptic perception in touch interactions, novel avenues for eliciting target sensations in humans, particularly for human-machine interfaces, can be unveiled.

In touch psychophysics, different layers of touch interactions factor into shaping dimensional structures in perceptual space (Figure 1). One layer is the composition or ingredients that make up the stimuli. Closely related is the layer associated with the stimuli/material itself, embodying its inherent properties that result from the composition and synthesis of the previous layer, which can be tuned and quantitatively assessed. Adjacent to this layer lies the skin-stimuli interface, where alterations in thermal, mechanical, or electrical attributes, among other types,

upon contact can be observed and measured. Finally, the psychological layer encompasses the perception and response of the human user following interaction with the stimuli. By considering each of these layers in tandem, a comprehensive perceptual space can be delineated, paving the way for the development of predictive models to elucidate human perception of stimuli characterized by specific properties.

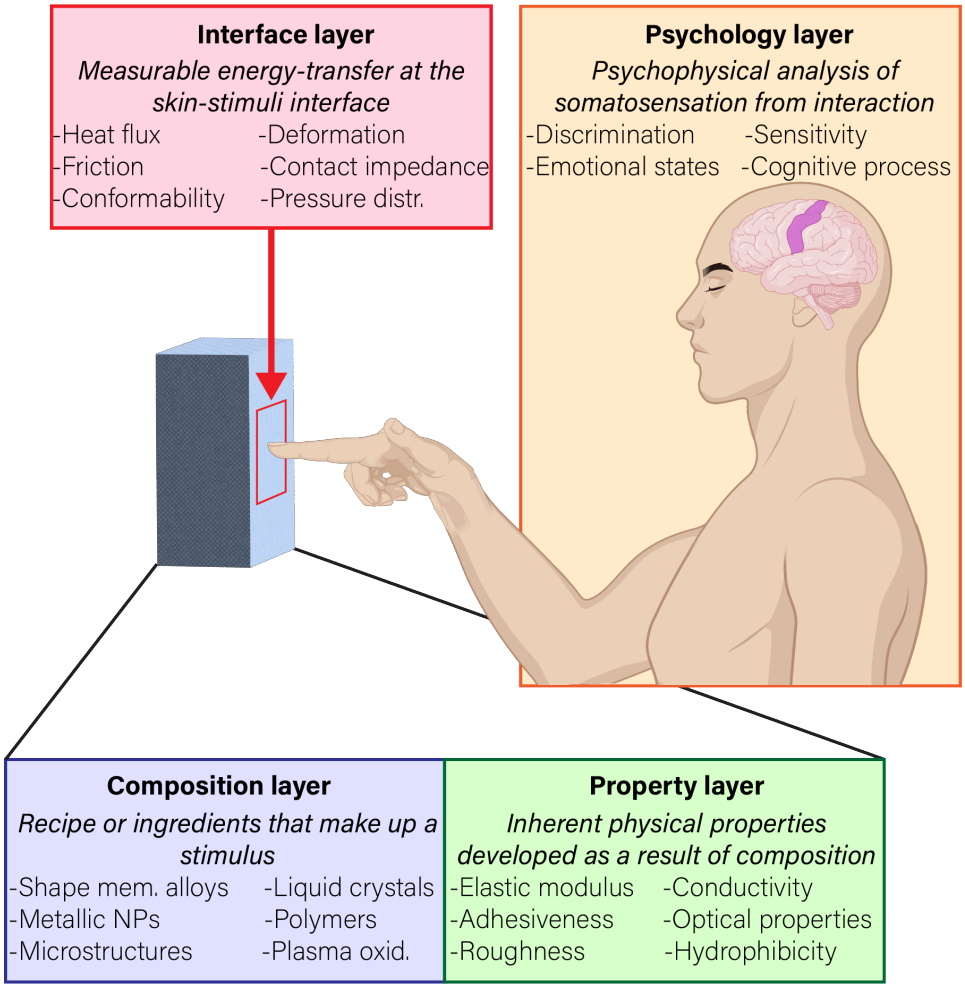


Figure 1. Effective material design for haptic perception involves four main layers. The composition layer consists of the individual components that make up the material. The property layer is the inherent physical properties that manifest as a result of the material composition. The interface layer is the quantitative energy transfer characteristics at the user-stimuli interface. The psychology layer is the primary perceptual component, where psychophysical analysis and cognitive processes from the touch interaction are evaluated.

In this dissertation, I conducted a study that developed a perceptual space for the sensation

of moisture or wetness by strategically designing each of the layers presented in Figure 1. Wetness is what is known as a touch-blend sensation, characterized by a combination of mechanical and thermal cues, and was selected as the sensation of interest since it has been one of the more investigated touch-blend sensations in literature. Previous studies in literature investigating softness and coldness in wetness perception, stacked cloth layers and used peltier elements to modulate wetness cues [4, 5]. To control softness and perceived coldness in a more controlled manner, I used polyacrylamide hydrogels covered by a thin polymer film to develop a matrix of stimuli of varying mechanical and thermal properties via chemical composition. Using in-depth psychophysics and characterization of properties within the material and at the skin-stimuli interface, we developed a perceptual space with reliably distinct wetness levels. We also compared input parameters for wetness judgment prediction models and demonstrated an all-in-one organic material capable of eliciting wetness without physically touching any liquid.

Lastly, another consideration in effective haptic feedback for virtual reality platforms is how its form factor affects realistic immersion. Generally, haptic feedback devices come in one of three form factors: as a graspable device, a wearable device, or a touchable device [6]. All three of these form factors require interaction with physical objects. Often times, these devices are bulky, inconvenient, and can be difficult to isolate rendered sensations as all physical objects inherently have other irrelevant properties (thermal, mechanical, etc.). Over the last two decades, contact-free haptic modalities have been in development and are of increasing interest given the recent progress of virtual technology platforms. Some of the contact-free haptic methods are based on air pressure [7], plasma [8], magnetic fields [9], focused ultrasound [10], and high-power lasers, among others. Most of these methods are limited in spatial resolution and in distance between the user and source. High power lasers, however, have capabilities to overcome these limitations.

High-power pulsed lasers have been shown to produce mechanical sensations in human skin from a distance[11]. The laser pulses generate pressure waves in the skin from thermoelastic expansion and contraction in a process called the photoacoustic effect [12]. Most studies to date

have demonstrated the use of high power, coherent light on bare skin to produce a sensation that is perceivable at most ≈70% of the time [11, 13, 14]. To produce a more robust sensation, an elastic medium has been adhered to the skin to absorb the laser light, removing the "contact-free" aspect [15]. In this dissertation, a more robust tactile sensation is achieved using a thin layer of light-absorbing dye on the skin. In depth psychophysical experiments were conducted to show enhanced tactile perception with a variety of light wavelengths and light sources, including incoherent light (a standard Digital Light Processing (DLP) projector). The DLP projector as a source provides easy digital control of the light parameters and greatly reduces the cost needed to achieve contact-free stimulation. Lastly, an advantage of a commercial projector is additional safety for use compared to traditional high-power laser sources. All of these advantages combined, increase accessibility of contact-free haptic stimulation for artificial touch at a distance and with versatile light parameters.

The research in this dissertation strives to promote equitable access to medical resources through development of POC devices and enhanced haptic feedback technology for virtual healthcare platforms. Together these tools can have profound impacts for medical desert communities and meet the high demands for medical resources in the wider population. POC healthcare will improve accessibility to medical resources, enable prompt diagnoses, timely treatment, and enhanced monitoring of chronic conditions. The overall impact is a step towards bridging the gap in remote healthcare across all socioeconomic classes.

Chapter 1

Bidirectional Venturi Flowmeter Based on Capacitive Sensors for Spirometry

1.1 Introduction

Accurate and in situ measurement of pulmonary function is a crucial aspect of the diagnosis and treatment of chronic respiratory illnesses. Spirometry is a common tool used to measure lung capacity and diagnose respiratory illnesses, such as asthma and chronic obstructive pulmonary disease (COPD) [16, 17]. Medical grade spirometers that provide real-time continuous breathing data are typically located in hospitals, and thus are limited in access for the public. As a result, use of spirometer devices require referrals from doctors and are typically restricted for patients in immediate acute respiratory distress [18]. When the global healthcare system is under stress, (e.g., the COVID-19 pandemic), access to medical instrumentation can become scarce and pose a bottleneck for medical treatment due to increased demand from the patient side as well as decreased supply from healthcare shortages and supply chain disruptions. Thus, there is a need for low-cost, accessible spirometer devices to increase public access to respiratory diagnostic devices.

The American Thoracic Society and European Respiratory Society have established international standard for spirometry devices to ensure suitability for clinical grade pulmonary function tests (PFTs) [19]. Among the recommended measurements, one of the most useful values is the peak expiratory flow rate (PEFR), which is the maximum flow rate achieved from a

forced full exhalation. PEFR measurements are one of the most important and widely used tests for PFTs, as they provide information regarding constriction in major lung passages and minute bronchus branches [20, 21]. This spirometric index is widely used to monitor and diagnose COPD and, more commonly, asthma.

Spirometers are generally categorized as either volumetric or flow-measuring[22]. Volumetric spirometers measure lung capacity by quantifying the inhaled and exhaled volume of air, while flow-measuring spirometers measure the air velocity of the exhaled and inhaled air. Volumetric spirometers are generally low-cost but are primarily used as incentive spirometers. Incentive spirometers use a piston that moves based on the volume of air exhaled into the spirometer. Thus, volumetric spirometers are typically used to help patients with asthma[23] or those recovering from a surgery[24] reach a target volume, as it allows them to watch the piston move closer to a target volume as they breathe forcefully. Conversely, flow-measuring spirometers can obtain multiple spirometric indices, providing more useful information for disease monitoring and diagnoses. Flow-measuring designs include turbine sensors, hot-wire anemometers, and ultrasonic flowmeters [25, 26, 27, 28]. While many of these architectures have been validated, there are advantages and disadvantages to a given sensing mechanism. For example, ultrasonic and hot-wire anemometry flow detection are generally costly and require complex calibration [29]. Differential pressure-based spirometer designs are potentially inexpensive and portable, however, most studies run into the limitation of measuring flow rates in one direction only [30]. For example, Zhou et al. developed a wireless pneumotachometer, which measured differential pressure across a flow restrictor in a configuration known as the Lilly-type sensing unit, but the system was limited to only measuring positive flow rate (exhalation) values [31]. Flow-restricting designs also require more maintenance, since the restrictors need to be replaced as particulates from the breath build up from use. Alternatively, face masks have also been used with embedded triboelectric nanogenerators for real time respiration measurements [32, 33]. There have also been use of wearable 3D-printed sensors for measuring respiration rate directly on the stomach [34]. Other designs, such as the venturi tube, were limited to measuring flow rate for exhaled air

[34, 35], and only used to compare lung function between individuals with and without COPD [36].

The venturi tube is a widely used device to measure the flow rate of a fluid passing through the tube [37]. Outside of respiratory measurements, the venturi tube is seen in several consumer products such as industrial vacuum cleaners, atomizers, wine aerators, clarinets, among many others [38, 39, 40, 41]. The venturi design approach for spirometry specifically was originally evaluated by Titheradge and Robergs in a study that tested the performance of the venturi design under static and dynamic conditions [42]. A pneumotachometer and turbine flow sensor were used in series with the venturi meter, as reference measurements. In this configuration, the authors were able to compare signal-to-noise ratio (SNR), response time, air fluid-state transitions, and other device characteristics between the connected spirometers using paired t-tests. Overall, the authors found no significant difference in signal quality or response time between the venturi meter and the pneumotachometer. However, they observed that at lower air velocity and flow rates ($<$0.5 L s^{-1}), there was distortion in the differential pressure readings because of transitions between laminar and turbulent states of flow. This overestimation was attributed to the fact that the flow could not reach a steady state of full turbulence in the venturi flow meter. Barring this limitation for lower flow rates, the venturi design was deemed adequate to detect parameters attributed to respiration by normal humans. However, one of the disadvantages of a venturi flowmeter is its limitation to unidirectional measurement. This unidirectional constraint is due to complications with flow separation at the divergent sections of the tube. Divergent geometries can cause chaotic flow separation at high Reynolds numbers, which would exert unsteady pressure on the pipe walls and yield unreliable, fluctuating measurements. Given this performance evaluation of venturi tubes as spirometer devices, in this work, we designed a bidirectional venturi tube to measure respiratory flow rate via differential pressure measurements for both inhaled and exhaled air in human respiration.

1.2 Experimental Section

1.2.1 Spirometer Design

A common way to calculate fluid flow through a tube utilizes Bernoulli's principle on fluid flow. This principle states that a fluid exerts less pressure on its surroundings when it is flowing at a faster rate compared to a slower rate [37, 43]. The venturi effect can be used to experimentally estimate internal fluid flow through a constriction using Bernoulli's principle for a fluid with a known density. This principle assumes the fluid is both inviscid and incompressible (i.e. neglects viscous/friction losses and fluid compression).

In this work, a symmetrical venturi tube of a slender geometry with three sensing points to measure air flow in both directions was designed (Figure 1.1a). The pressure transducers were embedded into the tube walls to avoid obstructions to air flow. To measure respiratory exhalation, the differential pressure measurement was taken between sensors S1 and S2, with the assumption that there was minimal flow separation moving from the mouthpiece inlet to sensor S2. During this time, sensor S3 would experience chaotic flow due to separation and, consequently, was not used in the measurement. Flow analysis, as discussed later in this section, indicated that the flow over sensor S3 would have sufficient time to settle before the inhalation measurement. During inhalation, the pressure drop was measured between sensors S3 and S2, while flow separation was present at sensor S1 but would likewise dissipate before the subsequent exhalation in the next breathing cycle.

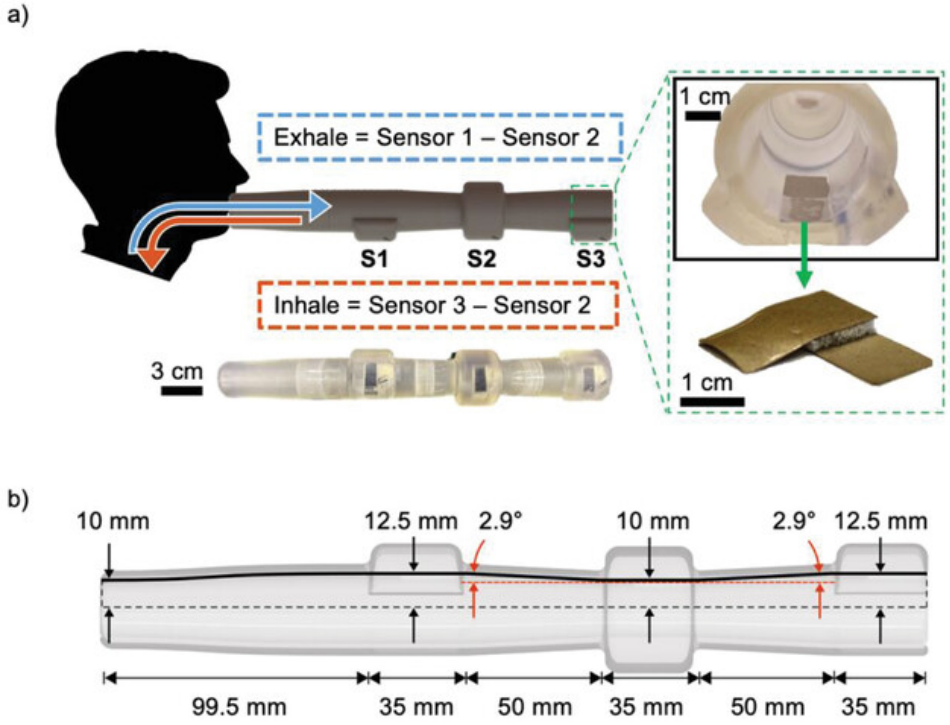


Figure 1.1. Overview of the bidirectional venturi spirometer a) User inhaling and exhaling into the tube. The blue line represents exhalation that is measured by subtracting the pressure of sensor S2 from the pressure of sensor S1. The orange line represents inhalation, which is measured by subtracting the pressure of sensor S3 from the pressure of sensor S2. The 3D-printed spirometer tube is embedded with 3 capacitive foam sensors in the tube wall. The green box shows the embedded sensor inside the tube wall with a close-up picture of the capacitive sensor. **b)** Spirometer dimensions.

The conservation of mass, for constant density internal fluid flow, dictates that the volumetric flow rate (Q in $m^3\ s^{-1}$) through a tube is equivalent to the velocity (v in $m\ s^{-1}$) of the flow multiplied by the cross-sectional area of the tube (A in m^2), where the subscripts indicate the tube segments:

$$Q = v_1 A_1 = v_2 A_2 = v_3 A_3 \tag{1.1}$$

$$p_1 - p_2 = \frac{\rho}{2}(v_2^2 - v_1^2) \tag{1.2}$$

$$Q = A_1 \sqrt{\frac{2}{\rho} \frac{(p_1 - p_2)}{(\frac{A_1}{A_2})^2 - 1}} \tag{1.3}$$

The pressure drop at the constriction was measured in the venturi tube and calculated according to Bernoulli's principle (Equations 1.1 and 1.2). The differential pressure $p_1 - p_2$ (in units of Pa or N m^{-2}) was proportional to the difference in the squares of the velocities. The fluid density (ρ) of this system was approximated as the density of air, 1.22 kg m^{-3}. Equation (1.3) was derived from Equations (1.1) and (1.2) to calculate the ideal exhalation volumetric flow rate using the cross-sectional areas and pressure drops; a constant of 1000 (not shown in Equation 1.3) was applied for unit conversion from m^3 s^{-1} to L s^{-1}. Since the flow direction was reversed for inhalation, Equation (1.3) was multiplied by -1 to denote inhalation data. For a continuous flow rate profile, whenever $p_1 - p_2$ was positive, it was used as the differential pressure signal to calculate the flow rate. On the other hand, when $p_1 - p_2$ was negative, $p_3 - p_2$ was used as the differential pressure signal for the flow rate calculation. The negative differential pressure signals were discarded in the calculation of the flow rate. Simulation-based correction factors were applied to the pressure (S_p) and flow rate (S_f) values, as elaborated on later in the discussion section.

To enable bidirectional measurements, this system was designed assuming unidirectional flow for inhalation and exhalation individually. This condition could be met by choosing a tube geometry that was as slender as possible, illustrated in Figure 1.1b. To mitigate flow separation and consequently unstable pressure measurements at the sensor locations, the changes in diameter were minimized, decreasing from 25 mm at the inlet/outlet cross-sections (locations of sensors 1 and 3) to 20 mm at the constricted section (location of sensor 2). Likewise, the transition in diameter was minimized and fileted with a 2.9° angle in the interior. Past the inlet, the tube was made symmetric about the central sensor to allow for the measurement of airflow in both directions. The three sensors were placed equidistant from each other and centered in each fixed-diameter section. The dimensions of the tube were optimized in simulations to maximize

sensor pressure changes in each direction.

To assess the viability of the bidirectional measurements, another consideration was the Reynolds number (*Re*) [44], which is the ratio between the inertial and viscous (frictional) forces of the fluid. The Reynolds number was calculated using Equation (1.4):

$$Re = \frac{\rho u L}{\mu} \tag{1.4}$$

where ρ is the fluid density (kg m^{-3}), u is the flow speed (m s^{-1}), L (m) is the characteristic linear dimension, and μ (kg m^{-1} s^{-1}) is the dynamic fluid viscosity. The density and dynamic viscosity (1.849×10^{-5} kg m^{-1} s^{-1}) were approximated to be that of air at room temperature for human respiration [45]. The characteristic linear dimension (L) was approximated to be the diameter of the tube inlet, which was 20 mm. Human exhalation has been reported to range in velocity from $\approx$2 up to 10 m s^{-1} [46]. These parameters yielded Reynolds numbers of 2600 and 13200, respectively. Other studies have suggested a laminar-turbulent transition with *Re* values of 2300 and 4000, with an $Re > 4000$ implying fully turbulent flow [47]. At high *Re* values, the fully developed turbulent state creates a boundary layer with more inertial force near the wall compared to viscous force, making it harder to separate. Because of the gradual changes in diameter and high *Re* values at higher flow rates, the flow did not separate early in the convergent sections. Even if separation did occur, it would be limited to a small region inside the tube as opposed to conditions outside the tube, which could cause much more disruption. As such, we expect some unstable pressure measurements for lower velocity breathing (tidal breathing) and stable measurements for higher velocities (deep breathing and PEFR measurements).

The third consideration made was the consideration of the Strouhal number (*St*), which describes the mechanism of flow oscillations [48]:

$$St = \frac{fL}{u} \tag{1.5}$$

where the characteristic length was the same value as the linear dimension (L) used in

Equation (1.4). The vortex shedding frequency (f) of this system was assumed to be 0.25 Hz (a rate of 15 breaths per minute), as the typical respiration rate for adults was between 10 and 20 breaths per minute [49]. The flow velocity range of human exhalation 2-10 m s^{-1} yields Strouhal numbers of 2.5 $\times$ 10^{-3} and 5 $\times$ 10^{-4}, respectively. Such low magnitude Strouhal numbers associated with human breathing indicates that the flow developed at any given time reached quasi-steady state. For this reason, that one flow direction can be assumed to have no impact on the other was determined, thus allowing our venturi spirometer to operate bidirectionally. The resulting spirometer design was realized with a stereolithography 3D printer in combination with additive fabrication techniques as explained below.

1.2.2 Sensor Fabrication Materials

Ag/AgCl ink (Ercon), Sylgard 184 poly(dimethylsiloxane) (PDMS) (Dupont), PELCO fast drying silver paint (Ted Pella Inc), NaCl, and 28 AWG shielded twisted pair cable (Amazon) were used to fabricate the capacitive foam sensors.

1.2.3 Sensor Fabrication

The capacitive foam sensors were reproduced from a work by Zhai et al [50]. The electrodes were fabricated on a 75 mm $\times$ 50 mm glass slide sprayed with mold release spray (Smooth-On). First, two thin pieces of 100 µm thick aluminum tape were adhered to each longer side of the slide, leaving the slide area between the tape pieces bare. Poly(dimethylsiloxane) (PDMS) (Sylgard 184, 1 g, 10:1 ratio of PDMS:curing agent) was prepared and left under vacuum for 5 min to remove air bubbles, while the mold release spray was left to dry. The PDMS mixture was then blade coated onto the prepared glass slide to create a 100 µm thick layer of PDMS. This film was cured on a hotplate for 30 min at 90 °C. The 10:1 PDMS mixture was mixed with Ag/AgCl ink (Ecron) at a ratio of 7:1 (Ag/AgCl ink: PDMS mixture) for forming flexible conductive electrodes. On each of the long sides of the glass slide, five additional pieces of silver tape were put down to make a confinement wall with an overall thickness of 500 µm

above the underlying PDMS layer. The (Ag/AgCl):PDMS mixture was left under vacuum for 10 min then blade coated on top of the partially cured PDMS layer on the slide. This film was then cured on a hotplate for 1 h at 100 °C. Once cured, an X-Acto knife blade was used to cut along the edges between the tape and electrode area, and the electrode sheet was carefully peeled from the slide, from which smaller electrodes (1 cm × 2 cm) were cut.

To make the porous foam dielectrics, PDMS (1 g, 10:1 ratio of PDMS:curing agent) was prepared and mixed with sodium chloride (NaCl) in a 17:20 ratio (85 wt% NaCl/PDMS). Once well mixed, the mixture was poured onto a 75 mm × 50 mm × 1 mm mold and cured on a hotplate for 30–60 min at 90 °C. Then, the cured mixture was removed from the mold and submerged in a dish filled with deionized (DI) water for 24 h to leach out the NaCl. The DI water was replaced the following day and again left overnight for a total of 48 h. The following day, the PDMS foam was warmed on a hotplate at 80 °C to evaporate the DI water from the foam. Once all water was evaporated, the foam was cut into 1 cm × 1 cm squares.

To assemble the sensors, one silver electrode was placed on a glass slide with the PDMS encapsulation layer facing down. A small amount of 10:1 PDMS mixture was placed in a 1 cm × 1 cm area on the electrode and a PDMS dielectric foam was placed on top of the PDMS mixture. This structure was cured on a hotplate at 90 °C for 30 min. Once cured, another silver electrode was placed on the glass slide, with the PDMS encapsulation layer faced down, and another small amount of the PDMS mixture was placed in a 1 cm × 1 cm area on the electrode. The other side of the dielectric was placed on top of the PDMS mixture, sandwiching the foam dielectric between the two electrodes. This device was cured for an additional 30 min at 90 °C.

To form electrical connections, a shielded twisted pair of 28 AWG wires was stripped to expose the two metal wires. Each wire was contacted and adhered to a silver electrode of the sensor using fast-drying conductive silver paint (Ted Pella, PELCO). The paint was cured on a hotplate at 90 °C for 5 min. A small amount of 10:1 PDMS mixture (PDMS/curing agent) was painted on top of this connection and on the rest of the exposed contacts of the silver electrode. This process was repeated for the second exposed wire to connect the other silver electrode on

the capacitive sensor.

1.2.4 Spirometer Tube Fabrication

The spirometer tube was 3D printed using a resin 3D printer (Form Labs, Form 3). The tube design was printed using a photopolymer resin (Clear V4). The print was cured at 60 °C for 15 min, which were the recommended curing conditions to fully cure the resin and non-toxic.

1.2.5 Ethical Committee Approval

The testing of this device was covered under Institutional Review Board study #804551 at the University of California, San Diego. Informed consent was obtained from the subject in this study.

1.3 Results and Discussion

1.3.1 Characterization and Calibration of Capacitive Sensor

The capacitance-to-pressure conversion was calculated using compression measurements using a Mark-10 force gauge (Figure 1.2a-c). The linear regime ($<$10 kPa) of the pressure-capacitance plot was used for the calculation of the capacitance-to-pressure conversion (Figure 1.2d). After comparing multiple sensor calibration curves, we used the most common trendline slope for the linear regime. The sensor was compressed cyclically to 400 Pa, and a very small drift of 0.3 fF was observed over 500 compression cycles (Figure 1.2e). We also looked at 1 compression cycle to calculate sensor hysteresis (Figure 1.2f). The hysteresis effect was found to be $\approx$43% at 100 Pa and decreases to $\approx$28.5% at 400 Pa. The change in pressure observed for tidal breathing falls in the $<$250 Pa range, while PEFR and deep breathing measurements yield pressures up to 1 kPa. Therefore, we expected to see more uncertainty in the tidal breathing measurements due to the hysteresis effect.

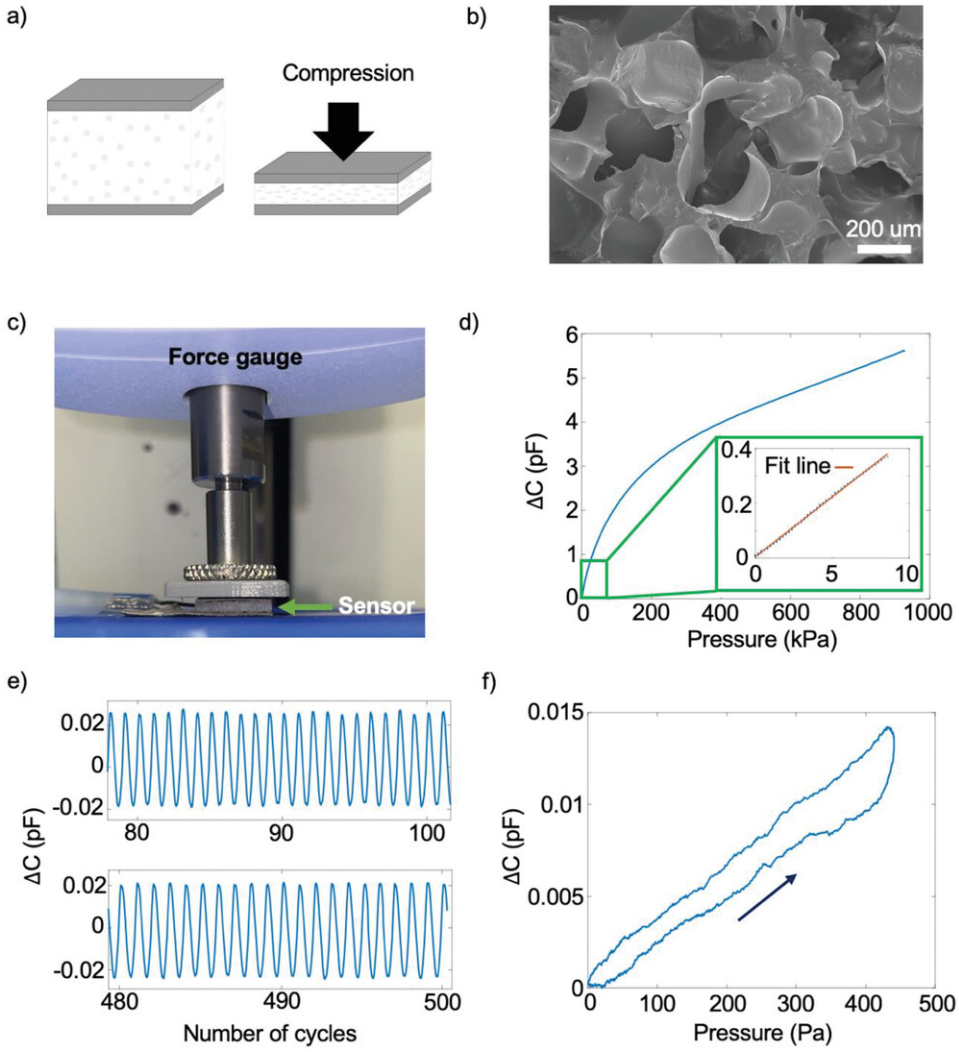


Figure 1.2. Mechanical characterization and calibration of capacitive sensors a) Diagram of capacitive foam sensor under compression. **b)** SEM image of PDMS dielectric foam cross section. **c)** Photograph of a sensor underneath a force gauge for compression measurements. **d)** Calibration curve showing the change in capacitance (instantaneous capacitance minus baseline capacitance) as a function of compression pressure. The green box shows a zoomed-in plot of the low-pressure regime with the corresponding fit used to determine a capacitance-to-pressure conversion factor. **e)** Cyclic compression of the pressure sensor. The top plot shows the capacitance during the 80th-100th cycles and the bottom plot shows the response during the 480th-500th cycles. **f)** Capacitance as a function of pressure for one compression cycle, showing slight hysteresis in the sensor readout.

As moisture accumulates from human breath inside of the spirometer, we looked at sensor stability before and after humidity exposure for 30 min. The humidity of human exhaled breath has been reported to range from 41.9% to 91.0% [51]. After exposing our sensors to 50%–88%

humidity, we saw negligible changes as shown in Figure A.1. The small, reported differences in sensor readout with and without humidity exposure justified use of this sensor in the device as it can withstand moist conditions. Lastly, we also looked at sensor response time via a ramp compression experiment on two different sensors (Figure A.2). The delay in reaching the peak capacitance after reaching peak compression for the two sensors was 148 and 563 ms. As a full cycle of breathing is typically from 2.5 to 3.5 s, the response delay can be from 14% to 20% of a full breathing cycle, which is an important factor to consider when looking at output breathing signals.

1.3.2 Simulations of Respiratory Flow Rate Characteristics through Finite Element Analysis

To calculate the expected response of the pressure sensors, Finite Element Analysis was performed using the acoustics module in COMSOL Multiphysics v5.6. An acoustic module was chosen given the oscillating profile of the input signal (breathing cycles). The interior wall of the tube was set as a hard boundary. The outlet of the tube was treated as an open boundary to atmosphere and was given an impedance value of 420 (Pa $\cdot$ s) m^{-1} for air at standard temperature and pressure. The mouthpiece of the tube was given a harmonic flow rate profile with a frequency that matched previous data sets for breathing [52]. The simulation was run for an airflow period of 12 s, and the pressures at the locations of the 3 sensors were recorded and exported to MATLAB R2021a for post-processing.

The local pressure inside the venturi tube showed the pressure decreasing from the inlet to the outlet for the exhale and the opposite trend for the inhale, validating that we should see a pressure drop for the 2 sensors in each respective direction (sensors 1 and 2 for exhale and sensors 2 and 3 for inhale) (Figure 1.3a,b). The differential pressure at the sensors was calculated for exhalation and inhalation (positive and negative flow at the input, respectively) for tidal breathing (Figure 1.3c). The exhale signal (blue line) was sensor 2 pressure signal subtracted from sensor 1, and the inhale signal (orange line) was sensor 2 signal subtracted from sensor 3.

The inhalation and exhalation sinusoidal peaks in Figure 1.3c were 180° out of phase from each other, as inhalation stopped once exhalation started and vice versa. The average peak-to-peak amplitude for tidal breathing from previous studies was approximately 0.1 L s^{-1} [53]. We chose to emulate tidal breathing in this simulation based on the amplitude of the input flow rate profile of this same value (0.1 L s^{-1}). Finally, the venturi flow Equation (1.3) was then used to calculate the flow rate from the differential pressure values (Figure 1.3d).

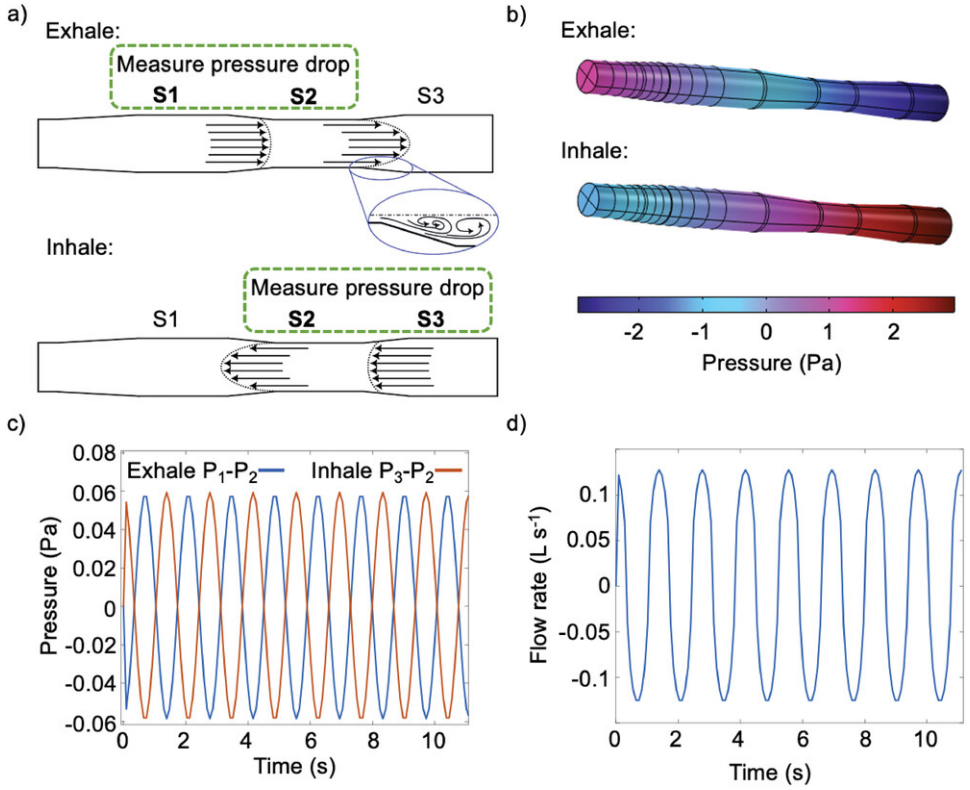


Figure 1.3. Simulated respiration flow behaviors a) 2D pressure profiles along inner walls. **b)** 3D simulation of pressure for inhale and exhale time points, which are the minima and maxima of the inlet flow rate profile, respectively. **c)** Differential pressure signals (orange and blue) at the sensor locations. The exhale signal (blue) is the signal of sensor 2 subtracted from that of sensor 1, while the inhale signal (orange) is the signal of sensor 2 subtracted from that of sensor 3. **d)** Flow rate plotted over time calculated from differential pressures in **c)**.

The FEA simulation calculated the flow rate at the sensor locations for a range nominal inlet flow rates (0.1 and 2-6 L s^{-1} in step of 1 L s^{-1}). As demonstrated in Figure A.3a, we found a discrepancy between the nominal input flow rate and the calculated flow rate at the

sensor locations. The discrepancy is possibly since an acoustics module was used, rather than a computational fluid dynamics (CFD) module. The acoustics module assumes compressibility of the fluid, while Bernoulli's principle in Equation (1.3) does not, likely causing an underestimation of pressure at the sensor locations due to variable fluid density throughout the tube (Figure A.4). The fitting function comparing the nominal flow rates to the calculated flow rates was found to be:

$$y = 6.1527x^2 + 5 \times 10^{-6}x + 3 \times 10^{-7} \tag{1.6}$$

where x represents the flow rate from the pressures at the sensor locations and y represents the nominal flow rate. This equation was used to convert the flow rate calculated from the sensor pressures measured in the device to the nominal flow rate, using Equation (1.6) to obtain the adjustment factor S_f as explained in the Appendix section A.1. The pressure values were calibrated to match those of the expected flow rates for the respective breathing types in simulation (tidal, deep, and forced), following steps shown in the flowchart of Figure 1.4a. The trendline for the relationship between peak pressure and nominal flow rate is shown in Figure 1.4b. The linear fit line from this plot is:

$$y = 0.5827x \tag{1.7}$$

where x is the nominal flow rate in L s^{-1} and y is the pressure peak in Pa.

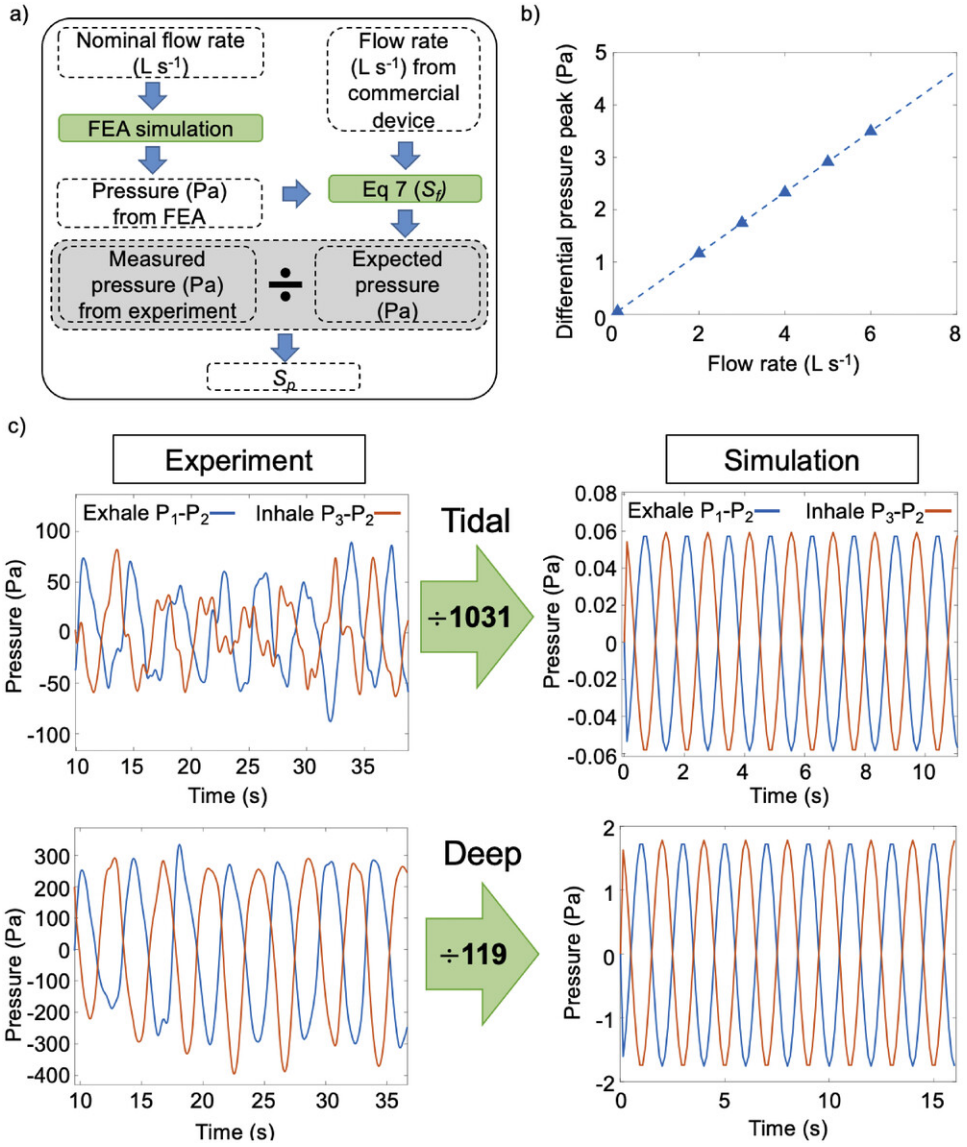


Figure 1.4. Pressure scaling factor calculations a) Flow chart for finding the differential pressure scale factor S_p. **b)** Differential pressure peaks as a function of nominal flow rate with dashed trendline. **c)** Rows 1 and 2 correspond to tidal and deep breathing, respectively. The plots on the left show the differential pressure waveforms as gathered from experimental measurements, while the plots on the right show the differential pressure waveforms calculated from simulations. The scaling factors are shown in the green arrows between the left and right plots.

For tidal breathing, the pressure values were scaled to those simulated using a flow rate of 0.1 L s^{-1}, based on previous literature reports for tidal breathing [53]. Our data thus this required a scaling factor S_p of 1,031 (using Equation 1.7) to get peak pressure values of ≈0.05 Pa,

matching the peak pressure value for tidal breathing simulations (Figure 1.4c). The same scaling method was used to calculate the scaling factors S_p for deep breathing (119) and PEFR (158) measurements (Figure A.5). The only difference is that the simulation flow rates did not include the high PEFR flow rate measured from a commercial spirometer. The differential pressure peaks, therefore, were extrapolated for higher flow rates to include the PEFR measurement range to calculate the scaling factor for PEFR measurements (Figure 1.4b). Together the scaling and adjustment factors, yielded results matching simulation and reasonable ranges to match commercial device readings for deep breathing and PEFR values, elaborated on further in the discussion section.

1.3.3 Breathing Tests

The spirometer was tested on a healthy individual for three different types of breathing exercises: tidal, deep, and peak expiratory flow. To reduce germ contamination and as an extra precaution for ensuring no contact with toxic materials, we covered the mouthpiece of the device with 3M Tegaderm film. We also wiped down the interior of the tube with an antiseptic wipe prior to use. For data analysis processing, the first step consisted of smoothing the capacitance data in the three sensors (Figure 1.5a). The corresponding differential pressure values were then calculated after the capacitance (pF) was converted into pressure (Pa), for which only the positive portions of each inhale and exhale signal were used in the flow rate calculation (Figure 1.5b). The negative portions of the respective signals were discarded, as these indicated timepoints at which flow separation was occurring. The exhalation and inhalation waveforms were separated by a phase shift of 180°, as predicted in the COMSOL simulations. Finally, the corresponding flow rate was calculated from the differential pressure values (Figure 1.5c). The calculated flow rates were higher than the values shown in Figure 1.3d, because these data corresponded to measurements taken while deep breathing, while the simulations in Figure 1.3d were given input parameters for tidal breathing.

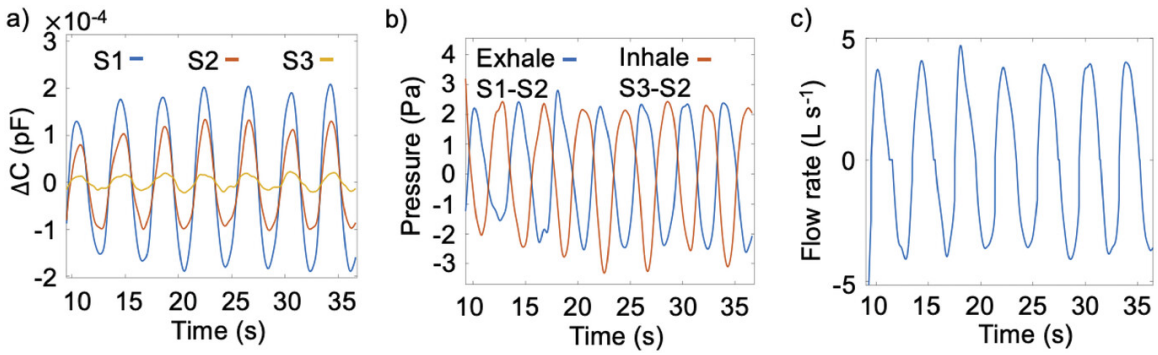


Figure 1.5. a) Plot of capacitance over time for all three sensors during deep breathing. **b)** Differential pressure waveforms for deep breathing, calculated from the plot in **a)**. **c)** Corresponding flow rate over time, calculated from the waveforms in **b)** using Equation (1.3).

Figure 1.6a–c shows flow rate as a function of time for tidal breathing, deep breathing, and a PEFR measurement, respectively. Flow volume loops for each breathing type were calculated by integrating the flow rate over time. The flow rate obtained from the differential pressure signals was negative in value for inhalation and positive for exhalation.

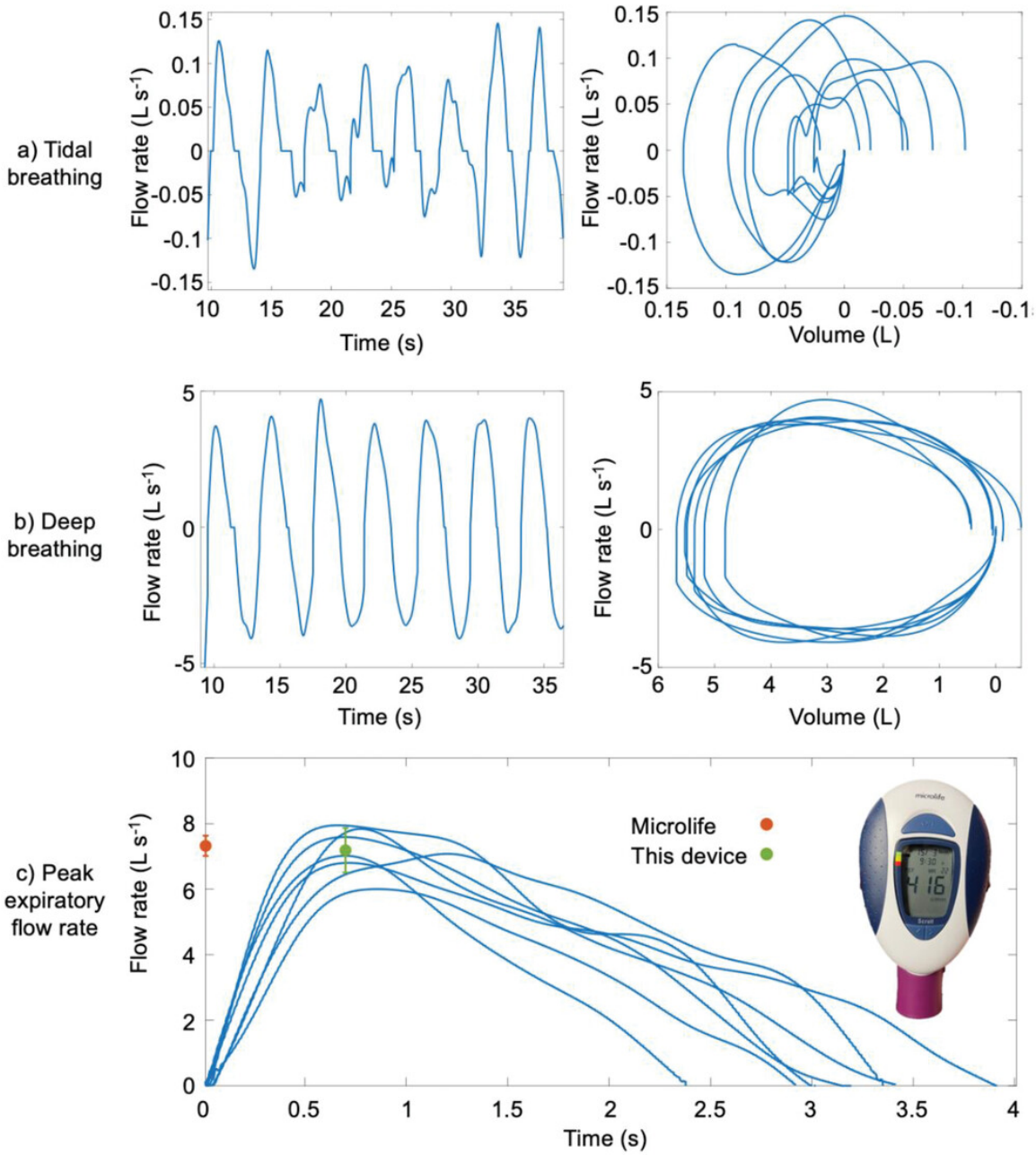


Figure 1.6. Each row shows measurements for each of the 3 types of breathing exercises recorded: **a)** tidal breathing (row 1), **b)** deep breathing (row 2), and **c)** PEFR measurement (row 3). The right plots in **a)** and **b)** depict flow volume loops calculated from the flow rate plots (left). The PEFR measurement plot depicts 7 individual measurements. The average PEFR value is shown in green for the 7 measurements taken on our bidirectional venturi spirometer and compared to values measured by a commercial peak flow meter (orange) and shown in the inset photograph.

In general, tidal breathing cycles show that the subject did not inhale and exhale the same

volume of air within each cycle. Therefore, the start and end points of the flow volume loops were often offset. This offset is due to the inability for human subjects to exert precise control over their breathing volume in shallow tidal breathing. Some of the mismatch between cycles is also likely due to distortion from the laminar-turbulent fluid transition at low flow rates during tidal breathing [42], as well as hysteresis of the sensor. The observed hysteresis implies that pressure values recorded during decompression were higher than expected, as it took longer for the sensor to return to its zero state. The higher uncertainty from hysteresis for the tidal breathing regime, in conjunction with the laminar-turbulent fluid transition (Re = 2300-4000) occurring more frequently for tidal breathing flow rates, yielded less accurate measurements, a result in agreement with those Titheradge and Robergs [42]. Some tidal breathing measurements also show flat line regions on the x-axis (Figure 1.6a). This is attributed to the exhalation and inhalation signals not crossing the x-axis at the exact same time point, causing negative values under the square root in Equation (1.3) when the inhalation signal is expected to be positive but is still negative. This could be a result of fluid transition delay, or also on the response time of the sensors.

For deep breathing cycles in Figure 1.6b, the subject was instructed to deliberately exhale forcefully, resulting in more controlled air flow. As such, the flow volume loops derived from deep breathing measurements tended to meet at the start and end points, with more similarities across multiple measurement cycles (resulting in overlapping loops). The average peak flow rate of the deep breathing measurements in Figure 1.6b was 4.028 ± 0.295 L s^{-1}. We compared this value with a commercial peak flow meter (Microlife PF100), obtaining an average peak flow rate (n = 10) of 3.800 ± 0.399 L s^{-1} (Table A.1). Our spirometer only measured the change in the pressure due to flow, and thus could not quantify absolute residual volume (i.e. lung capacity), which is typically 1 to 1.2 L in healthy adults [54]. However, it is possible that the difference between the inhalation and exhalation volume was in part due to the relative change in residual volume.

The PEFR measurement (Figure 1.6c) recorded the highest flow rate that could be forcibly

exhaled after taking the deepest breath possible. It is different from deep breathing in that it is generally recorded in 1 cycle increments and requires an exhale at the highest possible velocity [19]. From PEFR measurements, we obtained an average PEFR (n = 7) of 7.187 $\pm$ 0.679 L s^{-1} for the female subject. This value was checked against the commercial peak flow meter used by the same individual and determined to be within the same range (7.32 $\pm$ 0.31 L s^{-1} in the peak flow meter) (Table A.1). Both measurements were consistent with typical PEFR values for women (5.3-7.8 L s^{-1}) [55]. For reference, PEFR values for men typically range between 7.5-9.2 L s^{-1}.

Flow resistance was measured without fudge factors across all breathing types and yielded values of 49.51 $\pm$ 4.04 Pa L^{-1} s^{-1}, 32.07 $\pm$ 1.11 Pa L^{-1} s^{-1}, and 14.83 $\pm$ 2.53 Pa L^{-1} s^{-1} for PEFR, deep breathing, and tidal breathing, respectively. Flow resistance requirements by the American Thoracic Society are less than 49 Pa L^{-1} s^{-1} for 0-14 L s^{-1} [56]. The overall flow measurement range of the device in this study ranged from 0.1 L s^{-1} to 7.96 L $^{-1}$. We calculated an average standard deviation of sensor noise to be 0.037 pF. With a limit of detection criterion of an SNR of 3:1, this yields a device limit of detection of 0.09 pF. The above measurements demonstrated the capability of a bidirectional venturi spirometer to provide detailed flow rate information for both tidal and deep breathing, as well as PEFR values consistent with peak flow meter devices.

1.4 Conclusion

In this work, we demonstrate a venturi flow meter capable of measuring respiratory flow in two directions, for inhalation and exhalation, using capacitive foam sensors. We show that the bidirectional spirometer can monitor the flow rate continually for both tidal and deep breathing and obtained a useful metric (PEFR) for evaluating human lung function. The spirometer was made from a 3D printed resin body and capacitive foam sensors, and thus is both low cost and highly portable. Simulations using FEA and experimental testing validate the use of a symmetric

design for measuring both positive (exhalation) and negative (inhalation) respiratory flow using one device.

Future work entails multiple human subjects' evaluations to characterize the variability across individuals. From a design aspect, the pressure and flow rate correction factors (S_p and S_f, respectively) likely arise from the use of an acoustics module in the FEA simulations, as this module does not calculate turbulent flow and assumes no viscous forces are in effect. As such, simulations calculate much lower pressure values compared to experimental measurements. Future improvements to this venturi spirometer could be made possible by more detailed simulations to analyze the flow separation over time during breathing cycles, to determine the cause of the correction factor and potentially eliminate it. Another potential aspect for optimization is the length of the spirometer tube. Our calculations suggest that the distance from the inlet to the first sensor necessary to guarantee a fully developed flow would require a tube that is at least 29 cm long [57]. For practical use of the device, we chose a much shorter distance (9.95 cm), which likely caused some flow separation during measurements (explanation in Appendix section A.1). Thus, future geometry optimizations can be applied to ensure fully developed flow in the sensing regions. With improvements to device design and performance, other useful spirometric indices could likely be derived from breathing measurements, such as forced expiratory volume after 1 s (FEV1) and forced vital capacity (FVC). Overall, the low-cost, portable spirometer design we demonstrate here offers the potential to increase access to lung function testing. While future work is needed to examine the reliability issues of the device for point-of-care monitoring of respiratory illnesses, the compactness and ease of manufacture make our design amenable to rapid prototyping and validation.

1.5 Acknowledgements

Chapter 1, in full, is a reprint of the material as it appears in Advanced Materials Technologies 2023, vol. 8, Becerra, Laura L.; Rafeedi, Tarek; Ramanarayanan, Sankaran;

Frankel, Ian; Miller, Juliana; Chen, Alexander X.; Qie, Yi; Lipomi, Darren J.; Garudadri, Harinath; Ng, Tse N. The dissertation author was the primary investigator and author of this paper.

Chapter 2

Decoupling Coldness and Softness in Tactile Wetness Perception using Tunable Hydrogels

2.1 Introduction

Cutaneous wetness is a sensation felt by humans on a daily basis and plays a critical role in behavioral and autonomous adaptation[58]. While this sensation is commonly experienced, there is little attention focused on how the brain perceives this complex sensation on a single scale. The finger has a variety of touch receptors embedded in the epidermal layers. Each class of receptor responds to different types of tactile stimuli depending on its temporal response characteristics, conduction velocity of the nerve fiber, and receptive fields[59, 60]. Stimuli include pressure, temperature, vibration, skin stretching, among others[61]. While there are receptors specific to these stimuli, there is no touch receptor in humans specific to detecting wetness. For this reason it has been hypothesized that wetness is a learned human sensation from tactile experience, triggered by a combination of thermal and mechanical tactile cues[62, 63, 64]. Most studies that previously investigated the perception of tactile wetness used stimuli to target one of the two cues (thermal and mechanical)[65, 66, 67, 68]. Of the studies that have investigated both thermal and mechanical cues, most have required bulky moving parts to apply pressure for mechanical cues. Or, alternatively, they have used stimuli arising from textiles with variable water content[58].

Thus, a standalone material capable of being altered by intrinsically tuning both mechanical and thermal properties has yet to be tested for tactile wetness perception using the methodologies of psychophysics.

One of the first investigations of moisture perception in humans was described in the Victorian-era work of I.M. Bentley. In this study, the author posed the "blend" hypothesis, which states that wetness perception can be attributed to a combination of temperature and pressure cues[69]. This hypothesis was developed by having participants submerge their finger into a beaker of liquid covered with a thin layer of rubber. Thus, participants were asked to report their sensation of wetness without direct contact with the water. Since Bentley's blend hypothesis, other works have investigated the roles of mechanical pressure and temperature in wetness perception[58, 70, 71, 65, 66]. Tiest et al. studied static versus dynamic exploration of wet fabrics, where static touch consisted of no mechanical cues, yielding only thermal cues, and dynamic touch included both cues[70]. Their findings concluded that dynamic exploration and, consequently, mechanical cues improve discrimination of wetness in materials compared to only thermal cues. Other studies have focused on the role of surface properties specifically, such as stickiness and friction, on wetness perception[64, 66, 72]. Others have investigated moisture perception relative to levels of sweat production, which psychophysically showed that humans sense skin wetness on their feet primarily from tactile interactions, such as pressure and stickiness, given that thermal cues from skin temperature did not play a role in their wetness perception[73, 74].

Nearly all studies of wetness perception in humans, however, have used textiles with water content as the test material, where participants can come into contact with the water at the interface. To the best of our knowledge after an extensive search, there have only been two studies that looked at temperature and softness (not exerted pressure onto the subject) in wetness perception [4, 5]. The psychophysical results from both studies showed that decreasing temperature of the material led to increased wetness perception in humans. Similar to most of the studies in wetness perception, textiles were used as the test material. To modulate softness, the

authors stacked multiple layers of cloth on top of the other, changing overall thickness—and thus stiffness—across samples. One of the studies[5] found that changing thickness of the textiles only resulted in slightly increased softness perception and did not have a significant difference in wetness perception, in disagreement with [4]. Altering softness by stacking samples together can alter heat transfer rates due to inconsistent geometry thickness across samples [75]. To modulate thermal cues, the authors used Peltier elements to directly increase or decrease temperature of the cloth. Although the temperature of the interfaces in these cases was quantified and controllable, the material selection did not offer intrinsic and quantifiable softness nor thermal tunability. Here, we use an organic hydrogel that can be chemically altered to vary inherent softness in a more controlled manner, with similar thicknesses across all samples (1.01 cm +/- 0.12 cm) (Figure 2.1a,b and Figure A.6). Additionally, we control perceived coolness by varying the intrinsic thermal conductivity of the material, as opposed to changing the temperature. Thus, a Peltier element is not required, and inconsistent heat transfer is mitigated with near-identical gel thicknesses across samples. This study, therefore, demonstrates precise control and manipulation of hydrogel composition and corresponding material properties to influence human wetness perception. We use in-depth psychophysics to accurately measure how humans perceive and discriminate between distinct levels of wetness given the varied hydrogel parameters.

Polyacrylamide hydrogels are networks of cross-linked acrylamide units which are swollen in the presence of water (Figure 2.1c) [76]. Once solidified, these hydrogels are considered biocompatible and safe for handling. These materials have been used for a variety of applications from cell culturing, strain sensing, and drug delivery to the components of flexible batteries[77, 78, 79]. Of note for this current study, the mechanical and thermal properties of hydrogels can be easily manipulated. For example, when the fraction of crosslinker relative to the monomer content is increased, the porosity of the gel decreases and stiffness increases[80]. While the liquid component of gels normally consists primarily of water, alternate liquids can be used as well. For example, the viscosity of the liquid can affect the mechanical properties of the gel[81]. We hypothesized that the thermal conductivity of the liquid might also have an effect

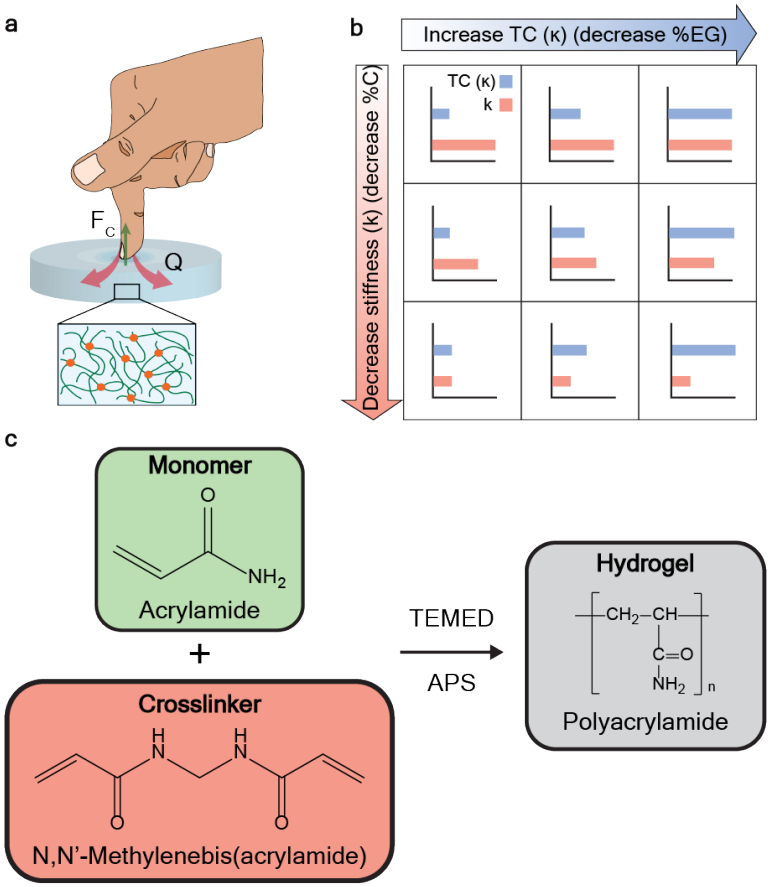


Figure 2.1. Overview of the experimental methodology a) Schematic diagram of tactile interaction. F_c is the compression force exerted onto the finger from the hydrogel. Q is the heat flux across the skin-gel interface. **b)** Matrix of variable properties for each material tested. There are three degrees of thermal conductivity (TC κ) in the gel soaking solvents: the increase in TC is achieved by decreasing the percentage of ethylene glycol (EG) relative to water in the gel. There are three degrees of stiffness (k), characterized by the ratio of crosslinker-to-monomer ratios . **c)** Chemical structures of the components making up the hydrogels. The polymerization is catalyzed by tetramethlethylenediamine (TEMED) and the initiator is ammonium persulfate (APS).

on the perceived wetness of a gel. Water has a relatively high thermal conductivity compared to most (non-metallic) liquids. Media which are more thermally conductive are perceived as colder than those that are less so, due to their ability to dissipate heat faster from the skin into the medium upon contact[82]. Therefore, hydrogels soaked in liquids with different thermal conductivities should elicit different temperature sensations, at least upon initial contact with the skin. Here, we aimed to evaluate the perception of tactile wetness using gels with varying stiffnesses and containing liquids with a range of thermal conductivities. Our hypothesis was that it would be possible to disentangle the individual contributions of mechanical and thermal cues in the perception of tactile wetness. It should thus be possible to create distinct levels of wetness perception in polymeric solids by modulating the crosslinking density and thermal conductivity.

2.1.1 Touch perception of heat extraction rates

It has been shown that humans are actually better at judging temperature differences rather than absolute temperature[83]. This is due to heat exchange between the skin and object temperature, causing an adaptation to temperature. Adaptation occurs when sensory receptors become less sensitive to a stimulus that was constantly perceived for some time. Detection thresholds for temperature changes are even higher when there are subsequent changes (i.e. heat-cool cycles)[84]. In psychophysics, the increased discrimination abilities with changes in temperature supports using free exploration of physical stimuli as dynamic interactions can yield more information about thermal cues compared to static interactions.

Thermal conductivity is a measure of the ability of a material to conduct heat[85]. It plays an important role in thermal contact conductance[86]. To estimate heat extraction across the skin-gel interface, we can use Fourier's law for calculating heat flow between two bodies in thermal contact, where Q is the heat flow (shown in Figure 2.1a), κ is the thermal conductivity, A is the area of the interface, and $\frac{dT}{dx}$ is the temperature gradient across the interface [87] (Eq. 1).

$$Q = -\kappa A \frac{dT}{dx}. \tag{2.1}$$

In this study, the heat (Q) is traveling from the finger into the gel, which is at ambient temperature in all experiments. Given this direction of flow, we can estimate that the thermal conductivity (κ) is dominated by the thermal conductivity of the gel. The interface area is the area of the finger which is in contact with the sample. On average this area has been measured at 2-2.3 cm^2[88].

The change in temperature across the interface can be determined by measuring the interface (or contact) temperature over time upon contact between the finger and the sample. There are two distinguishing characteristics of the temperature curve: the initial rate in temperature drop and the overall change in temperature during the measured period of contact, both of which have been noted as factors influencing the human ability to discriminate temperature [89, 90]. One previous study showed that while thermal cues from initial cooling rates played a prominent role in discriminating materials, thermal cues from total change in temperature also played a role after some time[90]. However, most studies focused on cues from rate of cooling[91, 92, 68]. Interestingly, in this study, we varied thermal conductivity of the gels and show that total change in temperature over 20 seconds to a quasi-steady state temperature resulted in the best prediction model for thermal inputs in wetness perception.

2.1.2 Softness/compliance of materials

Besides perceived temperature, mechanical compliance ("softness") also influences the perception of wetness. To understand what physical properties influence compliance perception, it is important to identify the measurable characteristics of soft materials. In mechanics of materials, the compliance of a material is the inverse of its stiffness (k), which is the ability of a material to resist deformation when applied with a compressive force, shown in Eq. 2, where F is the applied force, and δ is the displacement of the material caused by the applied force.

$$k = \frac{F}{\delta}. \tag{2.2}$$

The exploration of haptic perception regarding compliance has undergone extensive study, utilizing stimuli of various stiffness levels[93, 94]. Our group has previously showed that this perception is loosely related to a Hertzian contact model[95]. Metzger et al. revealed that the perception of softness can be influenced by adaptation, suggesting that prior haptic engagements with an object can influence how we perceive the softness of subsequent objects[96]. The susceptibility of adaptation for any sensation suggests that there are neural pathways specialized to detecting different levels of the sensation. Therefore, softness must have distinct neural pathways linked to different softness levels, reinforcing the notion that softness stands as a unique and fundamental aspect of perception. Other studies have highlighted the importance of cutaneous and kinesthetic cues in softness perception[97, 98], and even developed multi-layered perceptual models with high accuracy for softness[99]. A commonly reported conclusion is that surface deformation cues provide the most information for compliance perception[100]. Taking these findings into account, we can incorporate the role of stiffness modulation in stimuli used for wetness perception, and characterize the compression force needed for degrees of surface deformation.

Polyacrylamide hydrogels are considered viscoelastic solid materials[101]. By changing the crosslinker loading in a hydrogel (see Figure 2.1b), it has been shown that the elastic modulus, and hence stiffness, of the gel can be tuned[80]. Given the established positive correlation between softness and wetness perception[4], in this study we modulated the softness of hydrogels via different degrees of crosslinking. We characterized differences in compliance via measurements of elastic modulus from shear force, and axial compressive force at a fixed indentation depth.

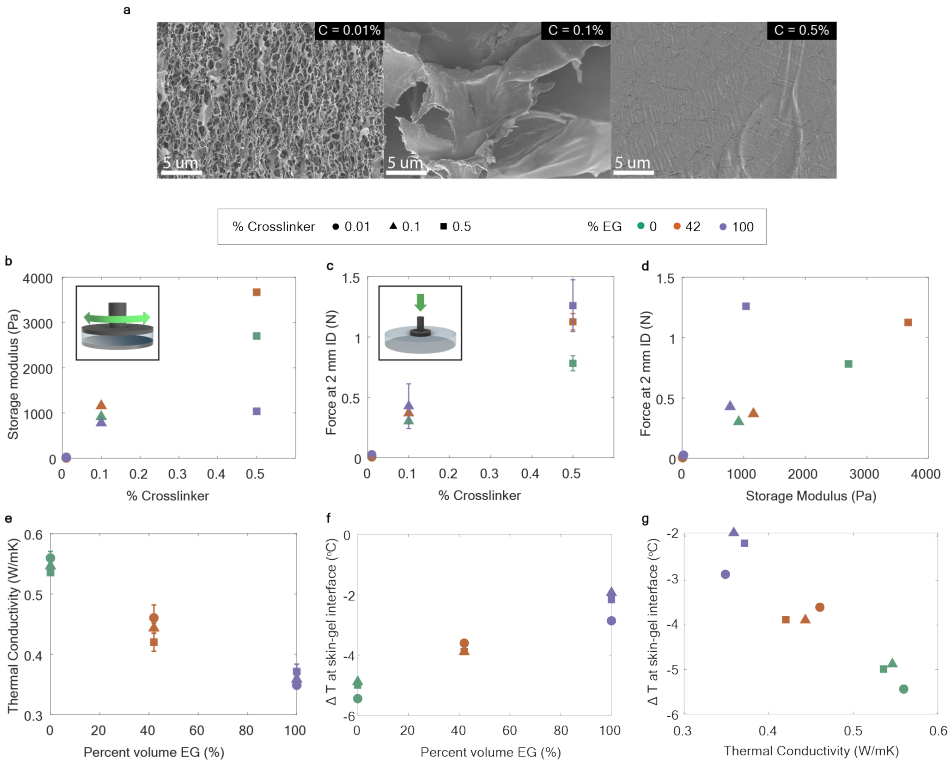


Figure 2.2. Material characterization a) SEM images of hydrogels of each crosslinking density (increasing crosslinking density from left to right). **b)** Storage modulus calculated from shear mechanical force across crosslinker content. **c)** The compression force from indenting the gel at 2 mm across crosslinker content. Center values are averages of the measurements on a different location for each sample and error bars were calculated using the corresponding standard deviation (n=3). **d)** Compression force at 2 mm ID as a function of storage modulus. **e)** Thermal conductivity of hydrogels as a function of EG content. Center values are averages of multiple measurements for each sample and error bars were calculated using the corresponding standard deviation (n=3). **f)** Change in temperature at the gel/skin interface upon stimulus contact as a function of EG content. **g)** Change in temperature at gel/skin interface as a function of thermal conductivity across all gels.

2.2 Results

2.2.1 Sample design and characterization

Stiffness modulation

The polyacrylamide hydrogel crosslinking densities were varied to create three different levels (0.01, 0.1, and 0.5%), calculated using Equation 3 from a previously published study on tuning polyacrylamide gel stiffness[80].

$$\%C = \frac{MBAA(g)}{Aam(g) + MBAA(g)} 100\%, \tag{2.3}$$

where %C is the percentage of crosslinker in the gel, MBAA(g) is the weight in grams of the crosslinker, N,N'-Methylenebisacrylamide, and Aam(g) is the weight in grams of the monomer, acrylamide, in the gel. After these ratios were combined, a catalyst (TEMED) and initiator (APS) were added to form the gel with deionized water (Figure 2.1c).

The resulting porosity both quantitatively (Figure A.7) and visually (Figure 2.2a) increased with decreasing percentage crosslinker. To quantify how the three solvents used in this study would affect the mechanical properties of the gels, storage modulus and compression force at 2 mm indentation depth (ID) were measured for each of the 9 gels after they were soaked in their solvents. Figure 2.2b and c show these parameters as a function of percent crosslinker. Interestingly, compression force at 2 mm indentation depth shows a more consistent trend for each crosslinker amount across soaking solvents compared to storage modulus (i.e. 100% ethylene glycol(EG) consistently had the highest compressive force and 0% EG had the lowest.) The reason for the discrepancy between mechanical measurement methods could arise from the modes of deformation utilized in the measurements. To measure storage modulus, the gels were placed between two parallel plates with a small amount of axial force and experience

shear oscillations at different frequencies. This method can have errors in measurement if the gels are not perfectly flat and flush with the parallel plates. The gels can also slip during oscillations due to residual solvent on the gel even after drying the outside. A movement that is more similar to the way a subject's finger would interact with a gel is compressive force upon indentation. This method also mitigates potential errors from slippage and the greater need for flush contact in rheological measurements, providing a more applicable physical variable to correlate with the psychophysical responses from participants. When plotting these two measurements against each other (Figure 2.2d), we observe a much lower modulus of the 0.5 %C gel with EG compared to the other two solvents, almost matching the modulus of the 0.1 %C gel with EG.

Thermal conductivity modulation

The EG dilutions chosen as the soaking solvents for the gels were selected based on a pilot experiment using 0.1%C hydrogels soaked in 5 different dilutions of glycerol. From a series of initial pilot psychophysical experiments (two-alternative forced choice (2-AFC)), a minimum TC difference of 0.125 W/mK that was detectable 50% of the time was measured at the corresponding abscissa and used as the minimum difference needed in the gel soaking solvents (Figure A.8). As we observed that glycerol content significantly affected the stiffness of the gel, we instead chose to use EG for all future experiments. Using thermal conductivity values from literature, three dilutions of EG in water were used to soak one gel of each crosslinker amount: 0, 42, and 100 vol% EG. These reported mixture thermal conductivities are 0.595, 0.429, and 0.251 W/mK, respectively[102], satisfying the threshold determined in the pilot experiment.

Nonetheless, we characterized the thermal conductivity of the gels soaked in the mixtures across all degrees of crosslinking (Figure 2.2e). The overall trend showed a non-overlapping distribution in thermal conductivities across EG content. Generally, a higher volumetric fraction of EG in the soaking solution produced lower thermal conductivity gels. This trend is consistent with the reported thermal conductivities of standard EG-water mixtures without gels [102].

Similar to the characterization techniques in the softness modulation, we sought to measure a thermal attribute more adjacent to the touch interaction felt by the user. Hence, the skin/gel thermal interaction was captured by fitting the characteristic cooling curve of the interface upon contact. We measured the temperature at the skin/gel interface over 20 s upon initial contact (Figure A.10) and fit an exponential (decay) regression to estimate the rate of temperature change and final temperature (Figure A.10). Figure 2.2f and g show the total temperature change at the interface for each gel and thermal conductivity as a function of %EG, respectively.

As crosslinker content, and therefore stiffness, decreased, the change in temperature at the skin-gel interface also decreased across all solvents. The increase in contact area at the interface with the softer gels allows for more thermal pathways with a higher contact area (A), increasing overall heat flux (Q) from the gel to the finger. Additionally, it has been psychophysically shown that temperature changes can be better resolved if the area of thermal stimulation increases [89]. Moreover, experimental measurements and molecular dynamic simulations have revealed that the thermal conductivity of PAam hydrogels is influenced by their crosslinking density, as demonstrated by Tang et al. in their study [103]. In particular, they examined a range of cross-linker concentrations (including those used in this study) and measured the thermal conductivities. The authors observed a rising trend in thermal conductivity for gels with crosslinker concentrations ranging from 0.016 to 0.099 mol%, which is likely attributed to the increase in thermal pathways resulting from the transition from van der Waals interactions to covalent bonds. However, at higher crosslinker concentrations (0.099-0.263 mol%), a decrease in thermal conductivity was noted, and this was attributed to an escalation in phonon scattering arising from an increase in side chains. In our results, we saw a general trend of lower crosslinking density correlating to higher thermal conductivity and vice versa, even for the gel that fell into the crosslinking range that should decrease in thermal conductivity according to Tang et al. The only exception to the trend was when 100% EG was used as the soaking solvent, causing the opposite effect (decreasing crosslinking density = decreasing thermal conductivity). The high EG content likely causes a different interaction between the

gel matrix and the surrounding medium, potentially reducing gaps in the matrix where solvent would be, resulting in a more dense, thermal insulating material.

2.2.2 Psychophysical studies

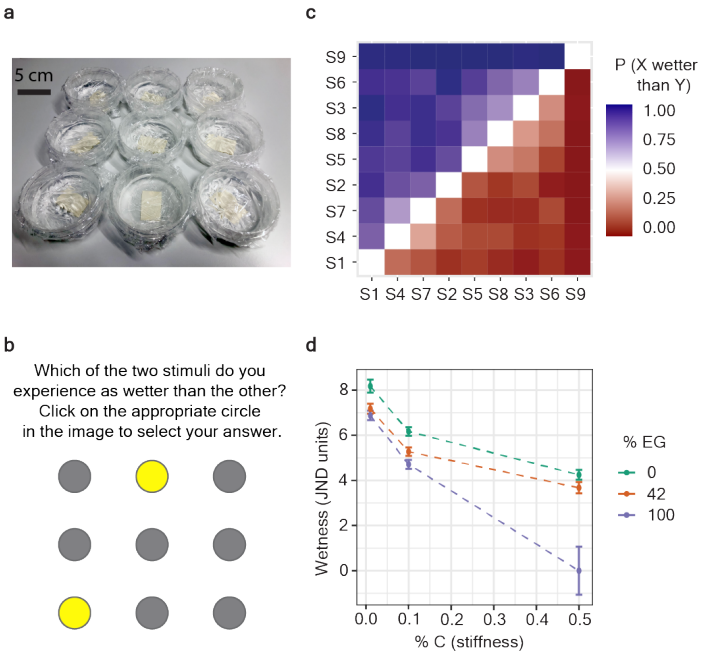


Figure 2.3. Psychophysical results a) Photo of gels in psychophysical test setup **b)** Graphical user interface for comparison instructions and stimulus selection **c)** Resulting transitivity matrix of all pairwise comparisons of stimuli **d)** Relationship between perceived wetness, and stimulus composition (percent crosslinker and percent EG) in the paired comparison psychophysics experiment (N=20 participants). Y-axis values are Bradley-Terry ability score parameters normalized to JND scale (divided by log(3)). Error bars are 95% confidence intervals on the parameter estimates.

The nine gels in the study were presented to each subject as shown in Figure 2.3a. Each gel in the matrix was covered with a thin layer of polymer film. Participants were instructed to compare two of the gels in each trial (2-AFC) and to select which of the two gels they experienced as being wetter using a computer interface (Figure 2.3b).

Figure 2.3c depicts all pairwise comparisons: the percentage of the time (across all participants) that Sample X was perceived as wetter than Sample Y. The stimuli have been arranged on the X and Y axis such that the left- (bottom-) most stimulus was perceived overall

(across all pairwise comparisons) to be the wettest stimulus, and the right- (top-) most stimulus was perceived overall to be the least wet stimulus. Crucially, this arrangement yields a plot in which all pairwise comparisons below the diagonal are $p < 0.5$, and all pairwise comparisons above the diagonal are $p > 0.5$. This property means that the data satisfies the criterion of weak stochastic transitivity: if Sample A is perceived as wetter than Sample B and Sample B is perceived as wetter than Sample C, then Sample A is also perceived as wetter than Sample C. Transitivity of wetness judgements is important because it implies that even though two different physical parameters were manipulated in our study, participants still experienced wetness on a unidimensional scale [104].

To more precisely characterize participants' perceptions, we used a Bradley-Terry model [105] to transform pairwise comparison data into a latent "wetness" variable that reflects the relative probability that a stimulus will be judged as wetter than another. Bradley-Terry parameters are in log odds units; therefore, dividing all strength estimates by log(3) yields a wetness scale in units of Just Noticable Difference (JND), such that when Stimulus A is one unit wetter than Stimulus B, it will be perceived as wetter 75 percent of the time. Figure 2.3d depicts the perceived wetness levels of each of the stimuli in our study, as a function of how much crosslinker-to-monomer content was used for each gel (x axis), and how much EG-to-water content there was in the soaking liquid (graph color).

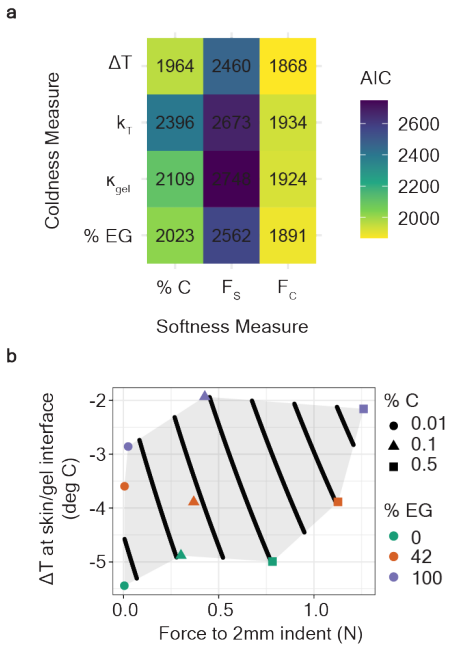


Figure 2.4. Psychophysical results a) Prediction model comparison (AIC values) across possible input parameters for coldness (ΔT is total change in interface temperature, k_T is the rate of change of interface temperature, κ_{gel} is the gel thermal conductivity, %EG is percent EG in the soaking solvent) and softness measures (%C is percent crosslinker of the gel, F_s is shear force, F_c is compression force) **b)** JND space from human-like physical properties with markers for stimuli recipe composition (%C and %EG) overlaid. The black lines represent distinct levels of wetness perception.

Qualitatively, it appears from Figure 2.3d that both stiffness and thermal conductivity influence human perceptual judgements of wetness. To quantify this observation, we fit a series of Bradley-Terry models in which the wetness of each stimulus depended (via a linear predictor) [106] on each possible combination of our measurements of stiffness (%C, F_s, F_c) and coldness (ΔT, k_T, κ_{gel}, %EG) and their interaction. In all 12 models, stiffness and coldness were highly significant predictors of the pairwise comparison results (Likelihood Ratio Tests, Bonferroni correction for multiple comparisons, all $p < 0.001$).

Each model can be compared using the Akaike Information Criterion (AIC), which quantifies the relative prediction error of each model (Figure 2.4a). Lower values of AIC indicate that one model is more predictive than other model; for example, the odds that the best model (AIC = 1868) is better than the second-best model (AIC = 1891) are 98716 to 1 (calculated

as $e^{(\Delta AIC/2)}$); an AIC difference of 10 is typically sufficient to establish that one model is significantly more predictive [107]. The strongest pattern in the AIC values was in choice of stiffness measurement: across all choices of coldness measurement, models using force to 2 mm indent as the measurement of stiffness were significantly better than models using crosslinker ratio or storage modulus. Furthermore, across all choices of stiffness measure, models using total change in skin temperature were significantly better than models using rate of change of skin temperature, thermal conductivity, or percent EG.

We next compared actual human judgements of wetness to the predictions of the best-fitting model (force to 2mm indent as the measurement of stiffness, total change in skin temperature as the measure of coldness). Receiver Operating Characteristics (ROC) analysis indicates that the model performed significantly better than chance, with an accuracy of 90.0% and an area under the curve (AUC) of 0.94 (bootstrapped 95% CI = [0.93,0.95]). To more rigorously test our model, and to estimate its out-of-sample generalizability, we re-fit the model on subsets of data in which a stimulus was removed, and tested the model's accuracy at predicting the stimulus it had not seen "Leave one out cross validation", LOOCV). When predicting human judgements for an unseen stimulus, the LOOCV model still performed significantly better than chance, with an accuracy of 79.8% and an AUC of 0.87 (bootstrapped 95% CI = [0.84,0.90]).

Finally, we used the parameters of the best-fitting model to generate predictions of human judgements across the gamut of possible physical parameters we can generate. This yielded a representation of perceptual space that can be used to recreate a particular level of perceived wetness using different combinations of physical stimulus parameters (Fig. 4b). The diagonal lines in Fig. 4b depict combinations of parameters yielding the same perceived wetness. For example, the sample with 0.1%C and 100%EG is perceived to be approximately as wet as the sample with 0.5%C and 0%EG, but these samples are perceived to be 1 JND drier (i.e., judged to be drier 75% of the time) than the sample with 0.1%C and 42%EG. Notice that there are at most 7 JND steps that fit within the perceptual space that can generated by the combination of physical parameters that our technique can produce. This means that the techniques developed in

this study are capable of developing stimuli with 7 different levels of wetness that can be reliably distinguished from each other.

2.3 Methods

2.3.1 Hydrogel synthesis

The hydrogels were synthesized using the following protocol. First, aqueous stock solutions were prepared in water for the synthesis, shown in Table 1.

Table 2.1. Stock solution concentrations for hydrogel synthesis

Solution	Concentration
Acrylamide (Aam)	0.5 g/mL
N,N'-Methylenebisacrylamide (MBAA)	0.025 g/mL
Ammonium persulfate (APS)	10 %wt/vol

Each gel consisted of 20.00 mL (7.034 M) acrylamide stock solution, 250 μL (0.438 M) of APS stock solution, and 25 μL of TEMED. The volume of MBAA stock solution (0.1622 M) used for each crosslinker amount is as follows: 0.04 mL (C = 0.01%), 0.2 mL (C = 0.05%), 0.4 mL (C = 0.1%), and 2 mL (C = 0.5%). The volume of water needed for the solution to reach a total volume of 50 mL per gel was added. Acrylamide, MBAA, and APS stock solutions were added to the appropriate volume of water in a 150 mL Erlenmeyer flask. The flask was swirled gently to promote mixing, then the TEMED was added. After another gentle swirl, the solution mixture was transferred to a petri dish. The petri dish was then placed under UV light (350 nm) to cure the gels. Once cured, the gels were placed in water to allow for gel expansion. After the gels had swelled, the water was replaced twice, once each subsequent day. On the third day, they were transferred to one of three solvent mixtures: pure water, 42% EG by volume, or pure EG. To ensure proper absorption of the solvent, the new solvents were switched out three times over the following days.

The gels were cut into circles using a circle-shaped cookie cutter with diameters of 6 cm

and had thicknesses of $\sim$1 cm. For the experiment, stimuli were presented in nine circle shaped polyethylene containers (diameter = 10 cm, height = 5 cm), each containing a polyacrylamide hydrogel submerged in the soaking solvent. A thin film of bisphenol A- free plastic wrap was placed over the gels in the containers. The leak-proof containers were labelled from S1 to S9 in a way that was not visible to the participants.

2.3.2 Hydrogel characterization

Rheology

A rheometer (TA Instrument Discover HR-30 Hybrid) was used to measure the storage modulus of all hydrogels. Each gel was cut to have a 38 - 40 mm diameter to match the area of the sandblasted Peltier parallel plate geometry. The outer layer of the gel was dried with a delicate task wipe to avoid slippage during measurements. Each gel underwent an amplitude sweep at 25°C with an angular frequency of 1 rad/s.

Force-indentation measurements

Mechanical properties of the gels were further investigated using compressive force at 2 mm indentation depth. A motorized compression test stand (Mark-10 ESM303) was used with a force gauge to measure the compression force from 0 mm to 2 mm indentation at a rate of $\sim$0.65 mm/min. The compression attachment making contact with the gels was a flat disc with a diameter of 12.7 mm. The samples were pat dry and the soaking solvents were removed from the containers for measurement to avoid slippage upon compression.

Porosity

To measure the porosity percentage of each gel crosslinker amount, small gel samples were cut and lyophilized (Labconco FreeZone freeze-dryer 2.5L, 115V, 60Hz) for 48 h. Each freeze-dried sample was weighed and then soaked in absolute ethanol for 48 hours. After soaking, the volume and weight of each sample were measured. The percentage porosity of each sample was then calculated using Equation 1, where M_1 and M_2 are the mass of the hydrogel sample

before and after soaking in absolute ethanol, ρ is the density of the absolute ethanol, and V is the volume of the hydrogel after swelling.

$$Porosity(\%) = \frac{M_1 - M_2}{\rho V} \times 100\%. \tag{2.4}$$

Scanning electron microscopy

One gel for each crosslinker amount (0.01, 0.05, 0.1, and 0.5%) was imaged via scanning electron microscopy (Zeiss Sigma 500). The gels were prepared by being placed on dry ice for 3 h until frozen and immediately transferred to lyophilizer (Labconco FreeZone freeze-dryer 2.5L, 115V, 60Hz) and were freeze-dried for 48 h. The gels were then sputtered with Iridium using a sputter coater (Emitech K575X) with 70% power intensity for 60 sec. After sputtering, the gels were imaged.

Temperature at gel-skin interface

The temperature profile at the gel-skin interface was measured using two K-type thermocouple probes connected to a USB temperature data logger (LASCAR EL-USB-TP-LCD). The probe was stripped so that the sensing portion of the wire was exposed and taped to the fingertip where contact would be made with the gel. The other probe tip was placed on the gel itself. Each measurement consisted of 10 s of baseline data before contact, followed by 30 s of temperature data from contact with the gel. The finger was submerged in the film-covered samples until the gel was felt with light force.

Thermal conductivity measurements

Thermal conductivity of each gel was measured using a thermal properties analyzer (METER TEMPOS) with a 6 cm single needle probe (KS-3). Each gel had a volume of 100 mL and was cured in a custom designed 3D-printed mold. The mold had an inner diameter of 42 mm and a height of 96 mm, and was designed specifically to meet the minimum radial distance of the

medium around the needle probe for accurate measurements. The gels were all initially soaked in water for 3 days, with the water switched out everyday. On the fourth day, the gels were then soaked in their respective EG-water mixtures for 3 days, with the solutions switched out each day. For a single measurement, the gel was removed from the solution and placed in a cylindrical glass dish to hold the gel in place. The probe was connected to the meter and the needle was fully inserted vertically into the top center of the gel. The measurements were done inside of a Styrofoam box to mitigate large heat fluctuations. Three measurements were taken per gel.

2.3.3 Psychophysical experimental design

Participants

20 participants (13 female; 18-50 years old; mean age = 24.71) were recruited from the University of Amsterdam. Participants volunteered (n=13) or received course credit (n=7). The experiments in this study were approved by an Ethics Review Board at the University of Amsterdam (ERB ID 2023-BC-15923). The methods were carried out in accordance to the ERB's guidelines and regulations. Informed consent was obtained from all participants in the study.

Procedure

Before participants arrived, the experimenter arranged the nine experimental stimuli in a 3x3 grid in front of the experiment computer (Fig. 3a). The placement of each stimulus within the grid was randomized (by computer algorithm) for each participant.

Upon arrival, participants used a sink in the experiment room to wash and dry their hands (to avoid fouling the experimental materials, and to reduce variations in skin moisture). They were then seated in front of the experimental setup, read and signed the consent form, and read the instructions for the experimental task.

The experimental task was a 2-AFC paired comparison procedure in which the difference in perceived wetness of each pair of stimuli was evaluated. On each trial, participants were

instructed to touch two of the nine stimuli simultaneously, using their left and right index fingers. Their task was to indicate which stimulus felt wettest to them by selecting the corresponding circle on a computer screen (Fig. 3b). There was no time constraint: participants could take as long as they wished to make each judgement. There were a total of 144 trials, divided into four blocks of 36 trials, one for each of the 36 possible pairwise comparisons (i.e., each pairwise comparison was judged a total of four times). Within each block, the trials were presented in randomized order. Between each block, participants were required to take a break of at least 30 seconds.

2.4 Discussion

In this study, we psychophysically tested human perception of wetness using an organic material with tunable mechanical and thermal properties. Our aim was to decouple the influences of coldness and softness on tactile wetness perception and to understand which aspects of the stimulus dominate in wetness judgment. Change in coldness was enabled by soaking the hydrogels in liquids of different thermal conductivities, changing the heat extraction rates from the finger into the gel. Softness was varied by changing the stiffness of the gel via number of crosslinks in the polymer matrix.

Our psychophysical analysis revealed a consistent trend—softer and colder properties elicited an enhanced perception of wetness, aligning with findings from prior studies[62, 65, 108, 71]. That is, decreased stiffness of the material and rapid dissipation of heat from the finger correlated with an increased perception of wetness. Notably, participants checked their fingers after experiment completion and reported being surprised their fingers were dry. Emphatic reporting of wetness even in the absence of direct liquid contact, echoed observations made by I.M. Bentley [69]. We found a predictable pattern in the participants' judgment of wetness by showing the transitivity across the different combinations of stiffness and coldness, implying that the perceptual relationships of these two parameters are not arbitrary.

Further analysis revealed that parameters directly measuring the mechanical and thermal experiences of the subjects (such as changes in temperature at the interface and compression force at a 2 mm indentation depth) yielded the most effective prediction model (AIC). These results are notable for at least two reasons. First, the most widely-accepted "gold standard" measurements of stiffness (storage modulus) and thermal conductivity were amongst the poorest predictors of wetness perception. Second, the best predictors of human perception were in some sense the most "human-adjacent" measurements, less closely related to intrinsic properties of the stimuli and more related to how they interact with a finger-like object when pressed. Additionally, the total change in interface temperature was a better predictor in coldness measure for wetness perception than the rate of change of interface temperature. This is interesting because a common trend in thermal perception literature claims that while the amplitude of temperature change is a factor in temperature perception, cooling rates deem more important[90]. While thermal perception may rely heavily on initial cooling rates in temperature discrimination, our model suggests that perhaps long-term thermal characteristics are more indicative of wetness, such as prolonged sensation of cooling after contact due to evaporative cooling on wet skin.

Given that wetness is a more complex sensation compared to temperature, humans may require more stimuli exploration time to judge wetness than needed to judge temperature. Filingeri et al. concluded that while skin cooling influences wetness perception, other sensing modalities, such as vision, can affect individual thresholds for complex sensations such as wetness [68]. Therefore, it is possible that the modulation of softness affected the temperature discrimination abilities in this study. Lastly, our temperature measurements, taken using a thermocouple taped to the finger, likely yielded more stable estimates of the asymptotic temperature. Since the final temperatures were recorded after collecting numerous data points to a quasi-steady state, these measurements are less susceptible to the noise typically associated with the rapid changes observed in initial cooling rates.

We leveraged the prediction model to predict combinations of change in interface temperature and compression force that yield approximately equal sensations of wetness (in Fig

4b, stimuli on the same black line), and combinations that yield sensations of wetness that are approximately one JND apart (in Fig 4b, stimuli on adjacent black lines). Given these material types and stimulus parameters, we can expect to perceive approximately 7 gradations of wetness levels. The ability to correlate hydrogel synthesis parameters/recipes with the 7 perception levels is useful, but the more impactful result, is the ability to correlate it to the interface stiffness and temperature profile. This will enable a much more broad application of wetness stimuli, not restricting it to parameters specific to hydrogels.

This study represents a significant advancement towards developing a versatile, all-in-one material for rendering technology. By inherently tuning both thermal and mechanical properties, this material effectively targets specific wetness sensations, offering multiple benefits. Thermally, the material's thermal conductivity eliminates the need for external temperature adjustments, allowing it to function optimally at room temperature. Mechanically, the material maintains a consistent macroscopic geometry while still enabling stiffness modulation, enhancing its utility and simplifying its application. In essence, our findings contribute both to the field of psychophysics and also hold implications for material design in human-machine interfaces, highlighting the intricate interplay between softness and coldness in shaping the perceptive experience of wetness.

2.5 Acknowledgements

Chapter 2, in full, has been submitted for publication of the material as it may appear in Nature Human Behaviour, 2024, Becerra, Laura L.; Root, Nicholas; Clark, Ainsley; Rafeedi, Tarek; Brown, William; Chen, Alexander X.; Qie, Yi; Blau, Rachel; Miller, Juliana; Kapadia, Kabir, Ng, Tse Nga; Rouw, Romke; Lipomi, Darren J. The dissertation author was the primary investigator and author of this paper.

Chapter 3

Enhanced Dye-Sensitized Mechanosensation utilizing Pulsed and Digitally Modulated Light

3.1 Introduction

Most experimental and commercial systems for stimulating the sense of touch require physical contact with an actuator embedded in, e.g., a smartphone, video game controller, or wearable device. However, there are many contexts—e.g., the laboratory, clinic, defense technologies, and consumer electronics—where it may be desirable to activate peripheral neurons remotely; that is, to "project" haptic signals onto the skin. Here, we used pulsed light from a range of sources, notably a conventional digital projector controlled using a laptop, to generate "photoacoustic" signals in the skin. In psychophysical experiments, a cohort of human participants perceived these optical signals as predominantly mechanical—as opposed to thermal or noxious. While a small number of research articles have demonstrated a similar effect using short ($ns - \mu s$), powerful bursts of focused coherent light from a laser[11, 15], this is the first time the effect has been demonstrated with desktop, easily available equipment.

3.1.1 The photoacoustic effect

The photoacoustic effect, discovered in the 1880s, involves the generation of pressure waves in condensed matter using pulsed light[12]. The effect has been used for decades in

materials research to measure dissipation and storage mechanisms in solids[109, 110, 111], and more recently to generate high-frequency ultrasound to image and map tissue using endogenous absorbers, e.g., hemoglobin, or exogenous absorbers [112, 113, 114]. The penetration depth of red or near-infrared (NIR) light, along with the lack of scattering experienced by acoustic waves in biological tissue, has made photoacoustic tomography a robust tool for imaging with high resolution at depths of centimeters[115].

Photoacoustic waves are initiated by a thermal expansion pulse, caused by absorption of optical energy and followed by rapid thermalization. The expansion pulse decays into a wide range of frequencies which depend in part on the width of the optical pulse (nanoseconds in biomedical imaging)[116, 117, 118, 119, 120]. In the context of biomedical imaging, the duty cycle is small enough—often substantially less than 1 percent—that fast dissipation of thermal energy limits accumulation of heat, and thus induces rapid thermal expansion and subsequent contraction[121]. The stress waves created by this event contain a range of frequencies in the tens of kHz to MHz regime, too high to be detected by afferents of the skin. However, the individual light pulses generating these waves can be repeated at rates that are well within the frequency range of detection of mechanoreceptors, i.e., 20 Hz to 1 kHz[122].

The physical phenomena governing thermoelastic pulses and photoacoustic waves in matter have been investigated in detail. In particular, modeling and simulation studies of this effect in tissue and skin have been examined extensively from the standpoint of biomedical imaging.[123, 124, 125]. Generating pressure waves in condensed matter depends on the optical and mechanical properties of the target, as well as the properties of the incident light. The pressure change at position $\mathbf{r}$ in such instances is given by

$$p_0(\mathbf{r}) = \frac{B\beta\mu_a(\mathbf{r})\psi(\mathbf{r})}{\rho c_p} \tag{3.1}$$

where B is the bulk modulus of the target, β is the thermal expansion coefficient, μ_a is the absorption coefficient, ψ is the pulse fluence, ρ and c_p are the density and the constant-pressure

specific heat capacity of the target, respectively [126]. Increasing the absorption coefficient for the target by the application of dye effectively increases the degree of thermalization of light which leads to a higher initial pressure generation. However, the aforementioned pressure description relies on the conditions of thermal confinement and acoustic stress confinement, described by the time constants:

$$\tau_a = \frac{L}{c} \tag{3.2}$$

$$\tau_{th} = \frac{L^2}{\alpha} \tag{3.3}$$

where L is the characteristic length of the illuminated target, c is the acoustic velocity in the medium, and α is the thermal diffusivity of the target medium. Achieving high-resolution imaging in photoacoustic tomography requires a pulse width that is smaller than the stress Equation (3.2) and thermal confinement Equation (3.3) time constants. Such pulse parameters (on the order of nanoseconds for human tissue) can be achieved using an optical parametric oscillator (OPO). However, Gao et al. demonstrated that creating a pressure pulse in a target is possible using pulse widths higher than the confinement parameters [127] and describe the dependence of pressure peaks on pulse width and confinement parameters in such cases.

3.1.2 Tactile perception and articulation

Mechanical forces exerted at the surface of the skin are translated to neural impulses by the cutaneous end organs and afferent fibers of the somatosensory system [128, 129]. Along this pathway, signals are integrated, encoded, and ultimately categorized as familiar conscious percepts, e.g., pressure, vibration, stretch, and pain. In natural environments, the mechanical force applied to the surface of the skin must cause sufficient deformation to initiate action potentials stemming from the end organ. Low-threshold mechanoreceptor axons are innervated by their end organs according to the forces and frequency of deformation. Mechanical signals with

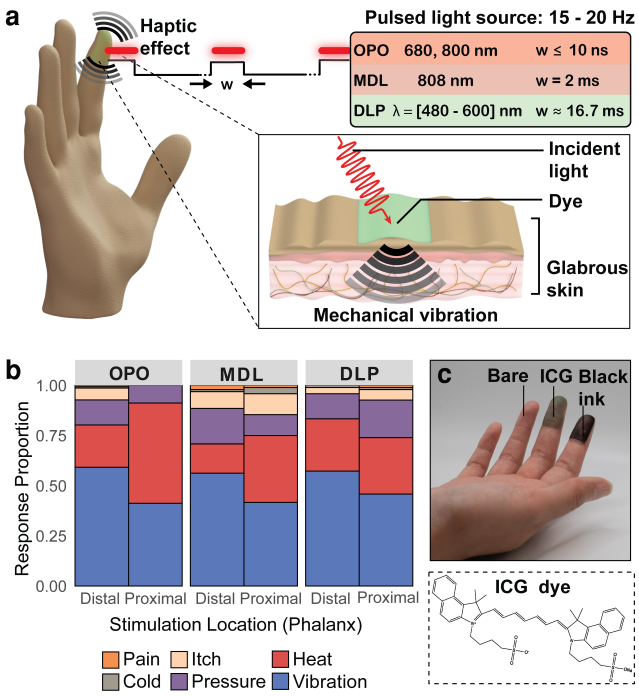


Figure 3.1. A brief overview of the effect and key result described in this work. a) Schematic diagram of the use of pulsed light to generate tactile sensations mediated by the photoacoustic effect. **b)** Summarized proportions of tactile sensations reported by human participants after applying the optical stimulus on the distal (fingertip) and the proximal phalanges. **c)** Photograph of a participant's fingertips coated with dyes used to sensitize the skin to the photoacoustic effect. The bottom panel shows the chemical structure of the IR-absorbing dye, indocyanine green (ICG).

frequencies below approximately 1000 Hz can in principle be detected by the mechanosensory neurons of the human skin. For example, the Pacinian corpuscle, primarily responsible for sensing vibrations on the skin, is most sensitive around 250 Hz extending to 1 kHz[128]. The Meissner's corpuscle, responsible in part for sensations of fine texture, is most sensitive in the tens of Hz, and the Merkel cell-neurite complex is sensitive at the level of a few Hz [130, 131].

Studies have explored various methods for delivering cutaneous tactile information without direct contact [10]. Primary approaches have included exerting mid-air pressure against the skin by air streams and air vortex rings. For example, Gurocak et al. employed air jets to create thrust forces on the hands of subjects to produce the sensation of weights of objects

in virtual reality[7]. Gupta et al. generated and tuned the formation of toroidal air vortices to direct tactile stimuli to different regions of the human body [132]. While these pressure generation methods have successfully delivered haptic feedback, they are limited by spatial and temporal resolution, as well as the distance over which the signals can be encoded. Alternatively, ultrasound haptic devices have been extensively investigated in their ability to evoke tactile sensations in mid-air. Focused ultrasound waves generate acoustic radiation pressure, enabling the transfer of haptic cues. This ultrasound-based approach facilitates applications such as haptic textures [133], localized haptic feedback [134], and haptic holography [135].

Lasers have recently emerged as candidates for generating cutaneous sensations. Historically, lasers were found to induce nociception and pain when applied directly to body surfaces [136, 137]. When mediated through air, laser light can create plasma and acoustic fields in mid-air and produce tactile sensations on human skin via shock waves [138, 8]. In the last decade, it has been demonstrated that pulsed single-wavelength lasers can evoke tactile sensations on the skin mediated by thermoelastic effects. Incident pulsed light is converted into thermal energy, inducing thermal expansion and subsequent relaxation. This process generates stress (acoustic) waves either directly on the skin or through an elastic medium (i.e., the photoacoustic effect [11, 15]). Despite the general understanding of the governing phenomenon, there has not been significant exploration in the parameters for irradiation and absorption that can drive the perception. Subsequently, there has been little refinement in characterizing the quality of mechanical, thermal, or noxious sensations. Here, we examine the effect of various light-source and optical absorbers (applied on the skin) in producing a robust tactile sensation, as shown in (Figure 3.1a, b). We evaluate the usability of several light source systems with different power, pulse, and wavelength specifications, including incoherent light from an inexpensive DLP projector. We perform psychophysical studies to examine the effects of applied dyes, the robustness of the mechanical sensation, and demonstrating the spatial localization or movement of the sensation.

3.2 Results

3.2.1 Psychophysical experimental design

We designed a sequence of psychophysical experiments to characterize the quality of perception (vibration vs. heat vs. pressure), different dye absorbers (Figure 3.1c), spatial effects (direction of movement of the stimulus), and light sources of different powers and wavelengths[3]. In contrast to the reports by Jun et al[11], pilot experiments with our system suggested that participants were unable to feel any effect from the pulsed light without the use of a dye. This may be due to the difference in divergence and absorptivity of the particular wavelengths. However, when applied to the fingers, a thin film of black ink from a marker or translucent indocyanine green (ICG) dye allowed the perception of a strong effect in most participants.

The safety concerns of light sources—particularly lasers—are related to potential damage to the retina, burning of the skin, and the generation of reactive oxygen species. The OPO and MDL laser sources had divergent beams and the exposure was below the safety threshold according to ANSI limits for skin exposure when the distance from the source to the skin surface was 1.5 cm. We verified safety of skin at 1.5 cm distance for the OPO laser by calculating a fluence of 13.3 mJ cm^{-2}, given the measured spot size of 2.7 cm^2 and technical specification of 45 mJ for peak energy. The safety of the MDL mechanically chopped and modulated was verified at 1.5 cm away with a calculated fluence of 3.56 mJ cm^{-2} and 3.28 mJ cm^{-2}, respectively. Note that in the mechanically chopped case, the fluence was comparable since the distance was 3 cm during examination, but had a larger pulse width. Lastly, the DLP projector fluence was estimated to be 10.3 mJ cm^{-2}.

Nanosecond pulse OPO laser experiments

For the first battery of experiments (Figure 3.2) the light source used was a nanosecond optical parametric oscillator (OPO) laser that is commonly used for photoacoustic imaging (Vevo F2 LAZR-X). The first experiment was a two-alternative forced choice (2-AFC) test in which

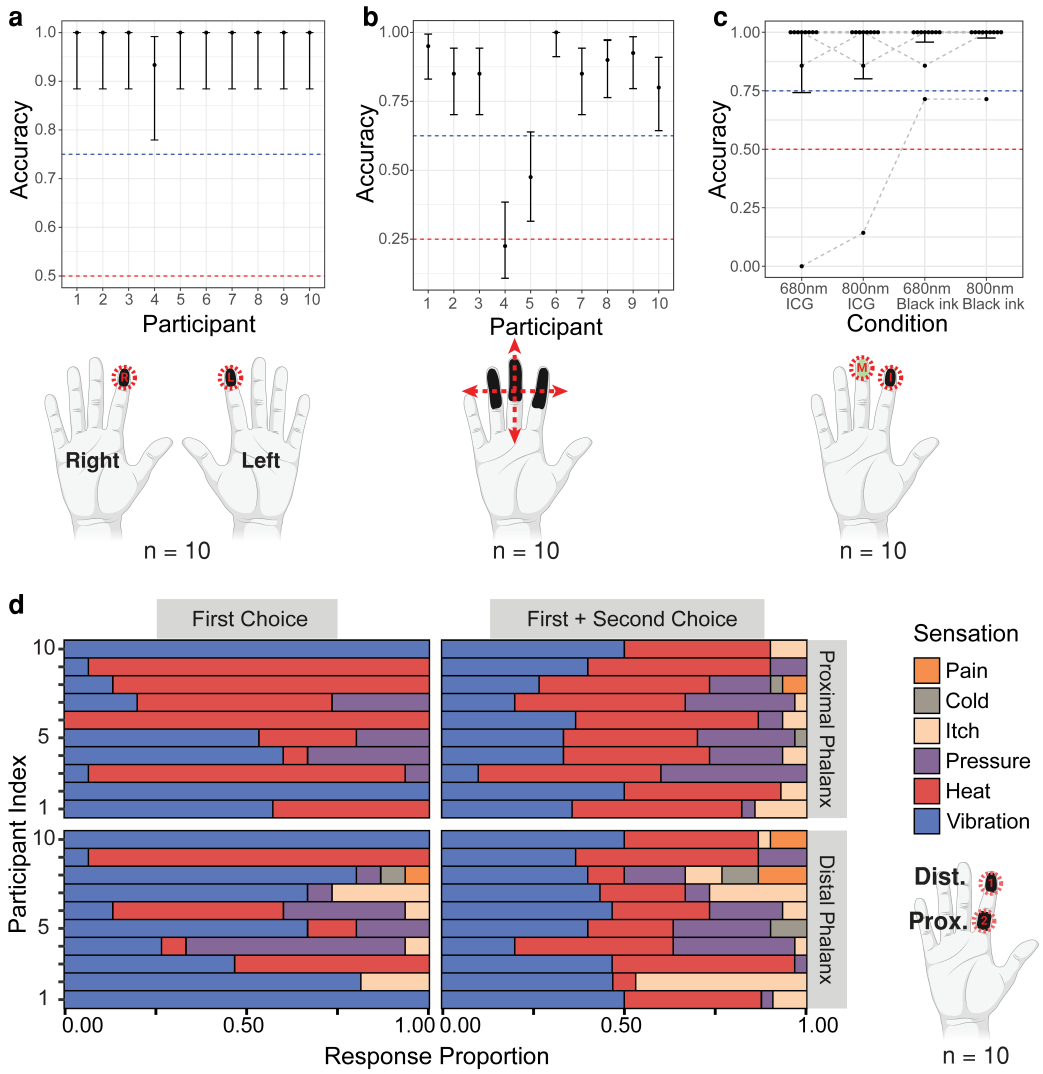


Figure 3.2. Perception accuracy of the effect in various conditions and effect categorization results produced using OPO system. **a)** Accuracy results of 2-AFC experiment to test for detection of stimulus on the index fingers marked with black ink. **b)** Accuracy of 4-AFC test for stimulus sweep in four different directions (red arrows) across distal and middle phalanges with black ink. **c)** Accuracy results for detection of stimulus with different wavelengths and ink types (GLMM estimated marginal means)(**Table A.4**). **d)** Proportion of responses for primarily perceived sensations by participants on the proximal and distal phalanges (left panels). Right panels show combination of primary and secondary perceived sensations for proximal and distal phalanges (top and bottom, respectively). Note: All error bars are 95% confidence intervals, which were back-transformed from the logit scale. The red dotted lines indicate chance performance, and the blue dotted lines depicts the 75% accuracy level typically used in 2-AFC (or 62.5% for 4-AFC) experiments to define the detection threshold.

black ink was applied to the index fingertips of both hands (Exp A) (Figure A.12a). On each trial, the marked regions of one of the two fingertips was irradiated with 680 nm wavelength stimulus, to test if participants could identify which finger (left or right hand) was stimulated. Overall, participants performed significantly better than chance (χ^2 (1) = 391.81, p <0.001; d' = 4.95, d' 95% CI [3.94,5.96]; more details on statistical analysis in the Experimental Section). We also characterized individual participant performance; of the ten participants, nine were 100% accurate, and the tenth was accurate on 93% of trials (Figure 3.2a). This performance is significantly higher than the 50% that would be expected by chance (all $p < 0.001$), and is also higher than 75% accuracy that is usually set by convention to correspond to the detection threshold in 2-AFC experiments.

Next, we tested the ability of participants to discern the direction of travel of the pulsed beam on the skin. On each trial, we swept the pulsed beam over an inked portion of the dominant hand in one of four directions, and prompted the participants to identify the direction (Exp B) (Figure A.12b). Overall, participants performed significantly better than chance (χ^2 (1) = 14.81, p <0.001; d' = 2.14, d' 95% CI [1.42,2.80]). We also characterized individual performance of each participant: of the ten participants, one was not significantly more accurate than chance ($p = 0.86$), one was significantly more accurate than chance ($p = 0.03$) but not more accurate than the typical detection threshold (62.5% for 4-AFC), and eight were significantly more accurate than chance (all $p < 0.001$) and also more accurate than the typical detection threshold (Figure 3.2b). The results from this experiment showed that participants could discern the direction of the sweep (i.e. left to right, front to back, etc.), suggesting that the relative position of the laser the stimulus can be spatially and temporally resolved [139, 140]. Additionally, the experiment demonstrated the ability of participants to detect stimulation across multiple areas of the finger (distal and middle phalanges) and across multiple fingers.

We then sought to investigate whether the stimulus could be perceived with an IR (i.e., nearly invisible) wavelength and a less conspicuous absorber than black ink. We thus turned to ICG, commonly used for tissue staining in biomedical imaging[141, 142], and compared

the effect of both absorbers at both 680 and 800 nm (Exp B) (Figure A.12c). While overall accuracy was higher with black ink (Wald $Z = 2.19$, $p = 0.03$), this effect appears to have been driven entirely by the results of a single participant (Figure 3.2c). When the participant's data are excluded, performance was not significantly influenced by the absorber, wavelength, or their interaction (all $p > 0.5$). Crucially, in all four conditions, participants detected the stimulus more often than would be predicted by chance (all $p < 0.05$; see Tables A.3, A.4), and in all four conditions all but one participant surpassed the conventional detection threshold of 75% accuracy. This it appears that the generation of this "phototactile" effect is amenable to a range of absorbers and wavelengths.

Pilot experiments and previous studies suggested that photoacoustic pulses could be perceived as a mechanical stimulus, rather than as, e.g., heat. However, the density of mechanoreceptors differs across different locations on the body [143]. We conducted an experiment to determine which sensation was perceived and determine whether this significantly differed by stimulation location (proximal and distal phalanges of the index finger). The relationship between stimulation location and reported sensation was highly significant ($\chi^2(5) = 34.3, p < 0.001$). When given a choice of pressure, vibration, itch, pain, heat, or cold, perceived by participants at the distal phalanx (fingertip), vibration was the most commonly reported sensation (Exp D) (Figure 3.2d and Figure A.12d). Post-hoc analysis of the Bonferroni-corrected chi-square residuals [144] suggests that at the distal phalanx (vs. proximal phalanx) there were significantly more reports of vibration (Z = 3.12, p_{adj} = 0.01) and itch (Z = 3.01, p_{adj} = 0.02), and significantly fewer reports of heat (Z = -5.24, $p_{adj} < 0.001$). We also asked participants for a secondary sensation they felt during stimulation. Heat was the most commonly reported secondary sensation for both distal (42.5%) and proximal (40.25%) phalanges.

3.2.2 Miniature diode laser (MDL) experiments

Mechanically chopped light sources

Given the expense (ca. $100,000) and inaccessibility of the medical OPO pulsed laser system, we investigated portable and less expensive light sources (Figure 3.3 and Figure 3.4). We pulsed two of the sources (a red laser pointer, 650 nm, and a more powerful miniature diode laser, MDL, 808 nm) at 20 Hz with 6.25 ms pulse width. Using a handheld setup (Figure 3.3 and Figure A.16), we first conducted a simple 2-AFC test on a cohort of 5 participants (Exp E) (Figure A.12e). Participants' accuracy was significantly higher than chance with the MDL (χ^2 (1) = 36.97, p <0.001; d' = 2.62, d' 95% CI [1.45,3.79]; Table A.5), but not with the red laser pointer (Figure 3.3b), probably due to its lower power. In the MDL condition, all but one participant was at or above 75%. For the chopped MDL source, we also added sham trials in which the non-inked finger was stimulated to verify that participants could only determine which hand was stimulated when stimulation was on the inked finger. Without ink, participants accuracy was no different than chance (p = 0.65; Table A.6), suggesting that chopped light from the MDL laser could not be felt without black ink (Figure A.17).

Modulated light source

The MDL source was then tested while being modulated, rather than mechanically chopped (Figure 3.4a). To modulate the light, we input a 20 Hz, 2 ms pulse width signal from a function generator with the MDL output in modulation mode, rather than continuous wave (CW) (Figure 3.4b). We performed a 2-AFC experiment on a new cohort of 12 participants.

We added sham trials in which the non-inked finger was stimulated to verify that participants could only determine which hand was stimulated when stimulation was on the inked finger. We first asked whether participants reported experiencing stimulation only when the inked finger was stimulated (i.e., detection accuracy). Participants' detection accuracy was significantly higher than chance (χ^2 (1) = 302.26, p <0.001; d' = 2.11, d' 95% CI [1.84,2.38]) (Figure 3.4c). We additionally characterized individual participant performance and found that

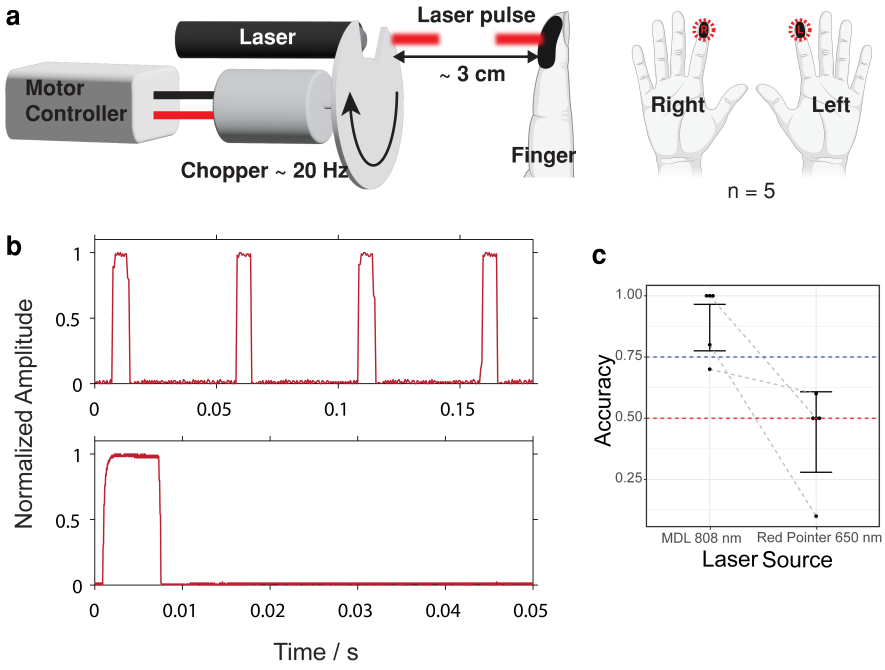


Figure 3.3. Perception accuracy of the effect using chopped low-power lasers (MDL and red laser pointer). a) The custom handheld mechanical chopper rotated at 20 Hz to output **b)** periodic pulses. **c)** Discrimination accuracy results of 2-AFC experiment of each source with inked fingers.

8/12 participants performed significantly better than chance (all p_{adj} <0.05), two participants performed significantly better than chance only when a multiple comparisons correction was not applied (p = 0.006 and p = 0.03), and two participants were not significantly better than chance (p = 0.19 and p = 0.47). The 8/12 participants whose performance was significantly better than chance also performed better than the 75% accuracy criterion. We next asked whether participants could report which hand was stimulated (i.e., discrimination accuracy) when the non-inked hand was stimulated; consistent with our expectations, participants' discrimination performance (left vs. right hand) was not significantly different from chance (χ^2 (1) = 0.01, p = 0.92; d' = 0.01, d' 95% CI [-0.29,0.32]) (Figure 3.4d). In contrast, when the inked hand was stimulated, (Exp F) (Figure A.12f), participants' discrimination accuracy was significantly better than chance (χ^2 (1) = 231.78, p <0.001; d' = 2.78, d' 95% CI [2.34,3.21]) (Figure 3.4c). We additionally characterized individual participant performance and found that 11/12 participants performed significantly better than chance (all p_{adj} <0.05), whereas one participant was not significantly better than chance (p = 0.84). Consistent with the detection data, the participant whose discrimination accuracy (left vs. right) was not significantly better than chance was one of the two participants whose detection accuracy (present vs. absent) was not significantly better than chance. Interestingly one participant was not significantly more accurate than chance on the detection task (60.4% accuracy, p = 0.19) but was significantly more accurate than chance on the discrimination task (83.3% accuracy, p = 0.002), suggesting that there were trials in which the participant reported not feeling stimulation, but could accurately guess the location of stimulation.

Lastly, we tested for sensation quality on the inked distal and proximal phalanges of the participant's dominant hand (Exp D) (Figure A.12d). There was a significant difference in the sensations reported at each stimulation location, $\chi^2(5)$ = 12.5, p = 0.03. Across all participants, the most commonly reported primary sensation at the distal phalanx was vibration (55.2%), followed by pressure (17.7%), and heat (14.6%). The most commonly reported primary sensation at the proximal phalanx was still vibration (41.7%), but with heat close behind it

(33.3%). Post-hoc analysis of the Bonferroni-corrected chi-square residuals [144] suggests that at the distal phalanx (vs. proximal phalanx) there were significantly fewer reports of heat (Z = -3.04, p_{adj} = 0.01). The most commonly reported secondary sensation at the distal phalanx was heat (44.79%) with pressure far behind (19.79%). Interestingly, the proximal phalanx had a near three-way tie between pressure (26.04%), vibration (25%), and itch (21.88%).

3.2.3 Incoherent light experiments

Given the brightness, availability, and ease of programming the light from a conventional light projector, we sought to investigate whether photoacoustic mechanosensation could be felt using incoherent light. To test this hypothesis, we used a commercial digital light processing (DLP) projector (i.e., a tabletop slide projector) with a Fresnel converging lens 17.8 cm away from the projector output lens (Figure 3.4e). The focal point was approximately 18 cm away from the Fresnel lens. With the projector oriented such that the beam was directed downward, the subject's finger was fixed at the focal distance. Black ink was used as an absorber on the skin and green pulsed light (15 Hz, 25% duty cycle) (Figure 3.4f) was played. Similar to the modulated MDL experiment, we added sham trials in which the non-inked finger was stimulated, to verify that participants could only determine which hand was stimulated when stimulation was on the inked finger. As expected for those trials, participant performance was not significantly different from chance ($\chi^2(1) < 0.01$, $p > 0.99$; d' = 0.00, d' 95% CI [-0.30,0.30]) (Figure 3.4g). Overall, 11/12 participants performed significantly better than chance and the 75% criterion in detection accuracy.

Next, we measured 2-AFC performance on the subset of data in which the inked finger was stimulated (Figure A.12f). Participants performed significantly better than chance (Likelihood Ratio Test, χ^2 (1) = 252.01, $p < 0.001$; d' = 2.99, d' 95% CI [2.52,3.46]) (Figure 3.4h). We looked at individual participant performance and found that 11/12 participants performed significantly better than chance (all p_{adj} <0.005), whereas one participant was not significantly better than chance (p = 0.54).

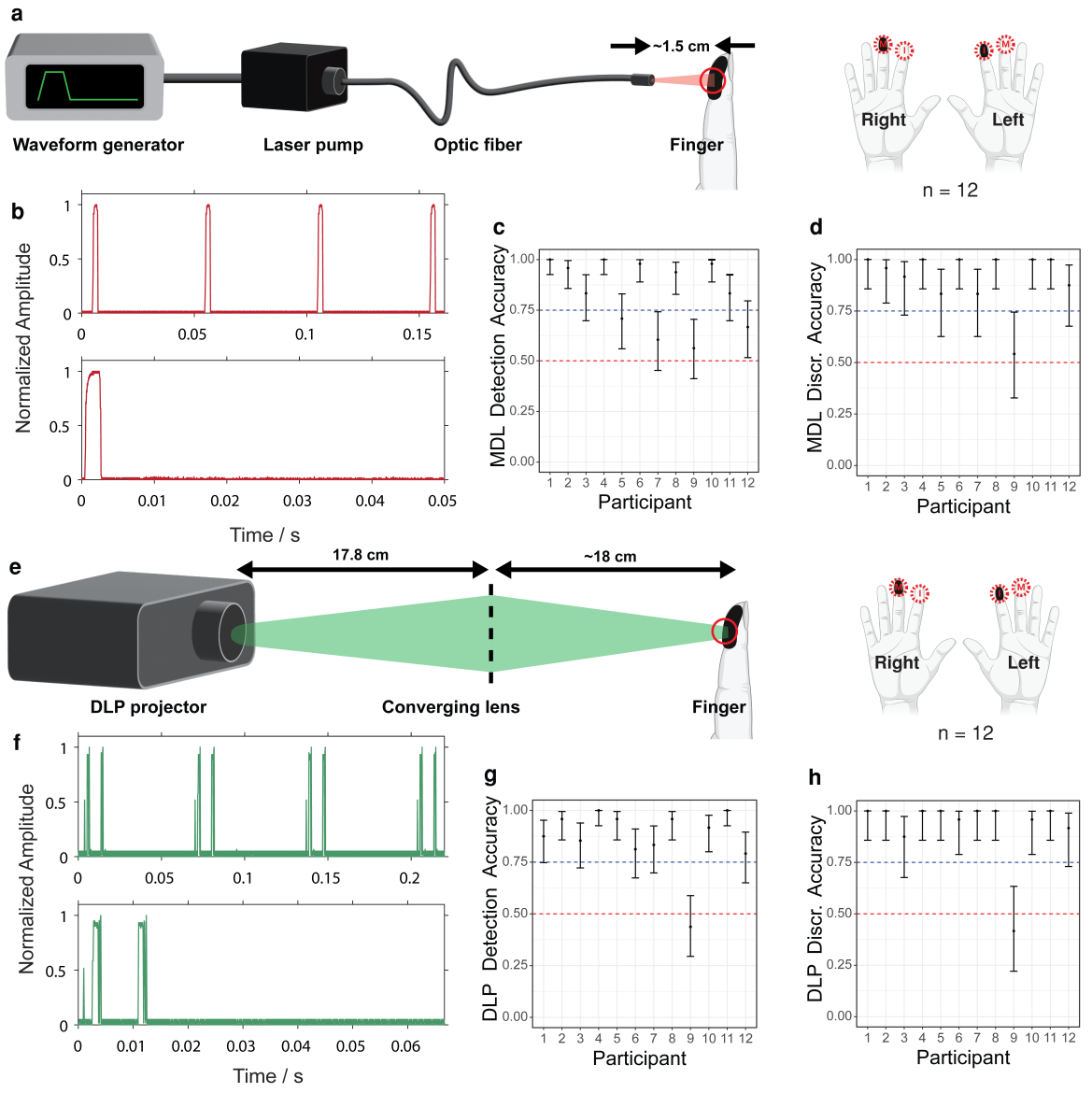


Figure 3.4. Schematics of the MDL laser and DLP projector systems, as well as the corresponding pulse characterization observed perception accuracy a) Schematic of the MDL set up **b)** Normalized amplitude of the optical output of the modulated MDL lasers showing typical pulse train and single pulse profile. **c)** Accuracy results for the 2-AFC detection of MDL stimuli. **d)** Accuracy results for the 2-AFC discrimination of MDL stimuli. **e)** Schematic of the DLP projector stimulation apparatus. **f)** Normalized amplitude of the optical output of the modulated DLP showing the pulse train of dual pulses produced by the DLP system.**g)** Accuracy results for the 2-AFC detection of DLP-generated stimuli. **h)** Accuracy results for the 2-AFC discrimination of DLP-generated stimuli. Note: All error bars are 95% confidence intervals on estimated marginal mean of accuracy per condition, back-transformed from the logit scale. The red dotted lines indicate chance performance, and the blue dotted lines depict the 75% accuracy level.

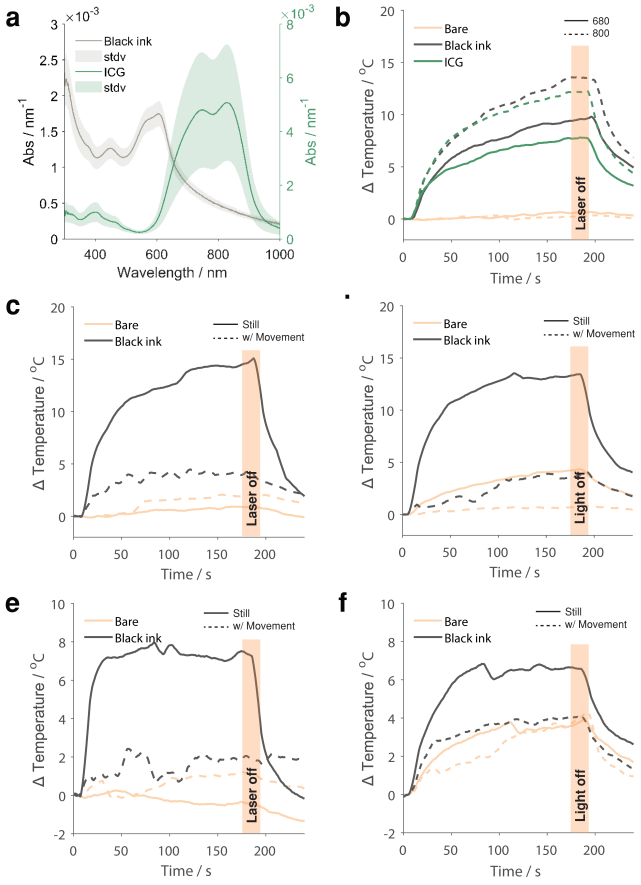


Figure 3.5. Characterization of dyes' light absorption. a) Absorbance spectra for ICG and black ink. **b-f** Thermographically measured temperature versus time with and without dyes with light stimulation: **b)** on the fingertip using OPO system **c)** on porcine skin samples using MDL source **d)** on porcine skin samples using DLP source **e)** on the fingertip using the MDL source **f)**, on the fingertip using the DLP source. MDL and DLP sources include stationary and moving light temperature profiles.

Finally, we tested for sensation quality on the inked distal and proximal phalanges of the participant's dominant hand (Exp D) (Figure A.12d). The primary sensation felt at the distal phalanx was selected as vibration 57% of the time across participants, followed by heat (26.0%). At the proximal phalanx, 44.8% of the responses for the primary sensation felt were vibration, while heat was selected 28.1% of the time. Like the modulated MDL and OPO, the highest proportion of reported secondary sensations was heat at the distal phalanx (33.33%). At the proximal phalanx, the projector source elicited mostly vibration (28.13%), pressure (25%), and heat (23.96%).

3.3 Discussion

The psychophysical results in this study have demonstrated a robust tactile sensation using all of the light sources, except for one, with the use of a dye as an optical absorber. The sources ranged from a high-cost and high-power photoacoustic imaging system to a low-cost commercially available DLP projector. The OPO laser experiments demonstrated a variety of capabilities amenable using haptic photoacoustics. Namely, we showed consistent detection of the stimulus on inked fingers, with 9 of the 10 participants scoring 100% accuracy. Participants were able to discern direction of travel of the beam across their skin, showing promising implications of using haptic photoacoustics as a means of encoding information, such as numbers, shapes, or letters. Also unique to the experiments with the OPO, we show the versatility of the light wavelength (680 nm, 808 nm) and optical absorber type (black ink, ICG), by showing that participants detect the stimulus more often than predicted by chance, without any significant influence from particular wavelengths or absorber types. This finding is also notable in that ICG and 808 nm light are both much less visible than the black ink and 680 nm light, which means that such photoacoustic haptic effects can be produced discreetly if need be.

When comparing the chopped MDL and red laser pointer, we found that there is some power threshold that determines whether or not the chopped light can be perceivable as a tactile

sensation. We know this because the chopping parameters were identical for each of these light sources, yet participants could perform significantly higher than chance in a 2-AFC test, while the same participants could not with the red laser pointer. Given the identical chopping parameters, this observation leads us to hypothesize that the difference in irradiance is what is responsible for discrepancies in detection of the stimuli.

We note some idiosyncrasies of the effects produced using different methods of pulsing the light. Anecdotal reports from the participants suggest that sensations from the chopped MDL were more likely to be perceived as heat than with the OPO system, possibly owing to a significantly longer duty cycle (i.e., dwell time) due to the homemade mechanical chopper: ca. 12.5% vs 0.00002%. In instances in which we chopped the light mechanically, the duty cycle has a dependency on the relative size of the optical window (e.g., between fan blades), which can cause some physical constraints in the design. Additionally for the same optical window, varying the duty cycle would require a change in frequency, introducing inconsistencies. To produce smaller and more consistent pulses, digital modulation was used for the next experiment.

While the DLP had two more participants that performed above the 75% accuracy criterion compared to the modulated MDL, neither detection nor discrimination accuracy were significantly different between the two sources (Detection: $\chi^2(2) = 3.46$, $p = 0.18$; Discrimination: $\chi^2(2) = 0.44$, $p = 0.80$). This is particularly interesting given the properties of the source. The DLP produced an incoherent spectrum of light modulated into two peaks per period Figure 3.4f. Given such parameters, we expected the DLP projector to be less effective in delivering perceivable tactile stimulation. However, the absorbance of the DLP light could have been enhanced by the intrinsic absorbance of the skin in the visible region. This observation could be seen as an increase in the temperature of DLP-illuminated bare skin (anecdotally shown in Figure 3.5d). The participant who was not significantly more accurate than chance at reporting left vs. right in the DLP projector experiments was the participant whose detection performance was not significantly better than chance—and was also the participant with at-chance performance with the MDL laser. The high detection accuracy experiments for both sources further support

the necessity to place dye on the skin to increase the absorption, thermalization, and subsequent tactile sensation. With the demonstrated efficacy of both black ink and ICG (Figure 3.5a) in the OPO experiments, the options for optical absorbers and corresponding light wavelengths can potentially be vast.

To qualitatively evaluate what types of sensations were being detected, we looked at sensation quality across three of the main light source types in this study: OPO, modulated MDL, and the DLP projector. Across all three sources, we consistently saw more reports of vibration as the primary sensation at the distal phalanx (55-58%) vs. the proximal phalanx (41-44%). Heat was the most commonly reported secondary sensation for both distal and proximal phalanges for all three sources, with the exception of the proximal phalanx for the MDL and DLP projector; in this case, pressure and vibration were reported as secondary sensations more often than heat. For the OPO laser, heat was the most commonly reported secondary sensation at both locations compared to the other sensations. This is likely due to the higher power of the OPO laser, and the fact that the beam was not moved around during stimulation as quickly as the modulated MDL and DLP projector were, since the larger rectangular beam of the OPO covered most of the finger during stimulation. The acoustic waves generated are mediated by transient absorption and thermalization of the optical energy, and thus the possibility remained that the effect could be perceived as thermal. This difference in perception may be explained by the reduced concentration of mechanosensory neurons—particularly the Meissner's corpuscles sensitive to frequencies in the range of the 20 Hz repetition rate of the laser—closer to the palm[145].

Consistent with OPO and MDL stimulation, vibration was reported more often across all participants for the DLP projector. However, unlike with the OPO and MDL stimulation, there was no significant difference in the sensations reported at each stimulation location, $\chi^2(5) = 4.00$, $p = 0.55$. The absence of a statistically significant difference in sensations between the distal and the proximal phalanges here might be due to the light source and pulsing parameters of the DLP system. As shown in Figure 3.4f, the DLP projector produces a double peak pulse train which is

due to the superimposition of the DLP system's frame rate and the digital commands given by the computer. Additionally, the non-monochromatic nature of the green DLP light (see Figure A.15) and its interaction with the black ink may have produced inconsistent or indiscernible sensations among participants. Further investigation is required to better understand the discrepancies observed in sensation quality between the DLP and the coherent light sources.

3.4 Conclusion

The in situ conversion of optical stimulus into a mechanical sensation, while based on a century-old effect, represents a potentially powerful modality of neural activation in humans. The effect explored here is robust and highly tolerant of a range of physical parameters such as wavelength, pulse rate, pulse width, and dye sensitizer. The use of a thin layer of optical absorber on the skin can not only enhance the mechanical sensation but will also reduce the overall light energy penetrating the skin due to thermalization.

A key advantage of a system based on in situ generation of mechanical forces in the skin include the ability to project the stimuli without physical contact. Moreover, the use of optical signals opens the door to the simultaneous stimulation of multiple types of afferent fibers. For example, by using overlaid variations in frequency and pulse width, it may be possible to activate multiple types of mechanically and thermally responsive neurons. Using existing DLP projector technology, where changes in light intensity and pulsing can easily be digitally controlled, makes generating this effect significantly more accessible and amenable to modifications. The DLP system also demonstrates the additional low-cost and optical safety advantages of using cheap, incoherent light sources in photoacoustic mechanosensation.

Advancing such abilities can facilitate the development of "tactile holography" which could have applications in medical training, physical therapy, pain management, complementary healthcare, remote operation, consumer electronics, and various applications of virtual and augmented reality. Moreover, such techniques are potentially applicable to mechanobiology in

applying high-precision forces to cells and tissues in vitro, as current micro poking tools require high precision manipulation to make physical contact and exert forces on cells[146, 147]. In particular, in the neurobiology and neuropsychology of touch and interoception, the ability to activate mechanically responsive cells and tissues without genetic engineering (i.e., optogenetics) or physical contact may open the door to new kinds of assays both in vitro and in vivo.

3.5 Experimental Section

3.5.1 Psychophysical design

All participants gave informed written consent and this study was approved by the Institutional Review Board of UC San Diego (#804228). The first set of experiments (Experiments A-D) were conducted using a commercial nanosecond optical parametric oscillator (OPO) laser for photoacoustic imaging (Vevo F2 LAZR-X). The applied stimulus had a pulse width of 10 ns with a pulse frequency of 20 Hz. All four experiments used a wavelength of 680 nm, except for Experiment B, in which 800 nm was also used.

Experiments E and F were conducted using the chopped MDL source using the handheld chopper (Figure A.16). The 6.25 ms pulses of light were at a frequency of 20 Hz. There were five participants for experiments E and F using the handheld chopper. The modulated MDL source was used on 12 additional participants for experiments D and F. The pulses of light were still at 20 Hz, but with a pulse width of 2 ms. The DLP projector was also used on the same 12 participants as the modulated MDL experiments. Experiments D and F were repeated using the DLP projector, with a pulse width of 16.7 ms and a frequency of 20 Hz. The light that was pulsed from the projector was the standard color green.

The psychophysical designs for all of the experiments conducted in this study are shown in Figure A.12. All participants were blindfolded and wearing foam earplugs with noise-cancelling headphones. For each experiment, participants were given the question to be asked prior to the start of the experiment and were prompted to answer the question with a tap on the shoulder at

the end of each trial.

- **Experiment A**: The initial experiment design (Figure A.12a) is a 2-alternative forced-choice test aimed at detecting the stimulus using black ink applied to both index fingers. During each trial, the optical stimulus was presented on one of the index fingers. Participants completed a total of 30 trials. On each trial, they were asked, "On which finger did you feel a sensation?" The only acceptable answers were "left index" or "right index". The trial order was randomized for each participant.

  Analysis: To characterize overall participant performance, we fit a logistic mixed effects regression with dependent variable of participant response (left or right), fixed effect of stimulation location (left or right), and random effect of participant. Participant accuracy was assessed using a Likelihood Ratio Test to compare the full model to a nested model in which the stimulation location term was removed. D-prime estimate and confidence interval were derived from the independent variable coefficient using the method described in [148]. To characterize individual participant performance, we used a separate binomial test for each participant, with a 95% confidence interval determined via the Clopper-Pearson method [149]. A Bonferroni correction was applied for multiple comparisons.

- **Experiment B**: In this experiment, we employed a 4 alternative forced choice paradigm to examine the identification of motion direction elicited by the applied stimulus. The dominant hand's distal and middle phalanges were marked with black ink. To assess the participant's perception, the investigator swept the stimulus in four distinct directions (Figure A.12b): front to back, back to front, left to right, and right to left.

  Each participant underwent ten iterations of the four possible directions, presented in a random order using a block design (n = 40 trials per participant). After the stimulus application in each trial, participants were asked, "In which direction did you feel the

stimulus sweep?" This procedure allowed us to explore the motion perception patterns effectively.

Analysis: To characterize overall participant performance, we fit a logistic random effects regression with dependent variable of trial outcome (correct or incorrect), and random effect of participant. Participant accuracy was assessed using a Likelihood Ratio Test to compare the full model to a nested model in which the intercept term was removed (fixed to chance performance). D-prime estimates and confidence intervals were derived from the model estimate of accuracy using the table in [150]. To characterize individual participant performance, we used a separate binomial test for each participant, with 95% confidence intervals determined via the Clopper-Pearson method. A Bonferroni correction was applied for multiple comparisons

- **Experiment C**: An experiment was conducted to investigate the impact of different ink types and wavelengths on stimulus detectability (Figure A.12c). Two inks were tested: black ink and indocyanine green (ICG) dye suspended in ethanol (4 mg mL^{-1}). The experiment also explored two wavelengths: 680 nm and 800 nm.

  For each participant, ICG ink was applied to the distal phalanx of their middle finger, while black ink was applied to the distal phalanx of their index finger, both on their dominant hand. With the two wavelengths, four stimulus conditions were established, representing all possible ink/wavelength combinations: ICG with 680 nm, ICG with 800 nm, black ink with 680 nm, and black ink with 800 nm.

  Each participant experienced seven iterations of the four stimulus conditions in a block design, which were randomly ordered, resulting in a total of 28 trials per participant. After each stimulus application, the participants were asked, "On which finger did you feel the sensation?" Acceptable answers were "middle finger" or "index finger."

  Analysis: To characterize the effect of ink type and wavelength on participant performance,

we fit a logistic mixed-effects regression model with dependent variable of trial outcome (correct or incorrect), fixed effects of ink type (Black ink vs. ICG), wavelength (680nm vs. 800nm), and their interaction, and a random effect for participant. The effect of choice of ink and wavelength was assessed using a Wald Z test of each model coefficient (Table A.3). Participant accuracy was assessed using Z tests of the estimated marginal means of accuracy for each combination of ink and wavelength.

- **Experiment D**: An experiment was conducted to discern the types of sensations experienced by the participants (Figure A.12d). To achieve this, we marked each participant's dominant hand's distal and proximal phalanges with black ink. The stimulus was then randomly applied to either the distal or proximal phalanx in a total of 30 trials. During each trial, the participants were asked "What was the primary sensation you felt?" followed by "What was the secondary sensation you felt?" after the stimulus application. They had six possible sensations to choose from: heat, cool, pressure, vibration, itch, and pain.

  Analysis: We computed response proportions separately for primary and secondary sensations within each sensation type. Subsequently, we combined the proportions of primary and secondary responses and calculated overall response proportions for each sensation type encompassing both primary and secondary sensations. To determine whether the reported sensations significantly differed by stimulation location, we ran three 2 (proximal/distal) x 6 (vibration/heat/pain/cold/itch/pressure) chi-squared tests of independence. To characterize the contribution of each sensation to the omnibus chi-squared statistic. We conducted post-hoc, Bonferroni-corrected Z tests of the chi-square residuals using the method described in [144].

- **Experiment E**:

  To determine whether participants could detect stimulation with different lasers (MDL

808 nm 2 W and red pointer 650 nm), we conducted an experiment to apply two different laser stimuli on the participants' inked fingers (Figure A.12e). The MDL 808 nm laser and red pointer 650 nm laser are referred to as laser 1 and laser 2, respectively. The participant's distal phalanges of their index fingers were marked with black ink. There were four possible stimulus conditions: left index with laser 1, right index with laser 1, left index with laser 2, and right index with laser 2. The four conditions were counterbalanced in a total of 20 trials.

Analysis: For the chopped MDL and red laser pointer (Figure 3.3), we fit a logistic mixed effects regression on sham trials only with dependent variable of trial outcome (correct/incorrect), fixed effect of laser (MDL 808 nm vs. red pointer 650 nm), and random effect of participant. The effect of choice of laser was assessed using a Wald Z test of the model coefficient. Participant accuracy was assessed using Z tests of the estimated marginal means of accuracy for each laser.

- **Experiment F**:

  We conducted an experiment to determine whether participants could detect stimulation without ink. We used the MDL 808 nm laser with the handheld chopper, modulated MDL, and DLP projector for this experiment. The participant's middle and index fingers on both of their hands were used for the experiment (Figure A.12f). Each hand had one of the two fingers marked with black ink (distal phalanx) and the other one bare. The four possible ink placements were counterbalanced across participants, with one participant condition repeated since we had five total participants. The stimulus was applied to each of the four fingers in random order for a total of 8 blocks (n = 32 total trials). After applying the stimulus, the participant was instructed to answer two questions: (1) "Did you feel a sensation?" and (2) "On which hand was the sensation felt?" Even if the answer was "no" to the first question, an answer had to be given for the second question.

Analysis: For the chopped MDL and red laser pointer (Figure A.17), we fit a logistic mixed effects regression with dependent variable of trial outcome (correct/incorrect), fixed effect of ink (present/absent), and random effect of participant. The effect of choice of laser was assessed using a Wald Z test of the model coefficient. Participant accuracy was assessed using Z tests of the estimated marginal means of accuracy for each laser.

For the modulated MDL and DLP projector (Figure 3.4), to test whether participants could detect presence or absence of stimulation, we fit a logistic mixed effects regression on all trials, with dependent variable of participant response (stimulation present vs. absent), fixed effect of stimulation (inked vs. non-inked; i.e., stimulation vs. no stimulation), and random effect of participant. To verify that participants could not perceive stimulation of the non-inked finger (i.e., that it was truly analagous to "no stimulation"), we fit a logistic mixed effects regression on the sham (non-inked) trials only, with dependent variable of participant response (left or right), fixed effect of stimulation location (left or right), and random effect of participant. To test whether participants could identify which finger was stimulated on the stimulation (inked) trials, we fit a logistic mixed effects regression on the stimulation (inked) trials only, with dependent variable of participant response (left or right), fixed effect of stimulation location (left or right), and random effect of participant. Participant accuracy was assessed using a Likelihood Ratio Test to compare the full model to a nested model in which the stimulation location term was removed. D-prime estimate and confidence interval were derived from the independent variable coefficient using the method described in [148]. To characterize individual participant performance, we used a separate binomial test for each participant, with 95% confidence intervals determined via the Clopper-Pearson method. A Bonferroni correction was applied for multiple comparisons.

Experimental setup

- OPO experiments (Experiments A-D):

  A chair and bench top were prepared for the human subject, fitted with a platform to place their hands on. The optical parametric oscillator laser of a VisualSonics Vevo F2 LAZR-X was connected to the medium size fiber optic cable. The two ends of the cable were taped together for easier handling. It delivered 10 ns pulses of 680 or 800 nm wavelength at a repetition rate of 20 Hz (duty cycle = 0.00002%). The diverging beam was spread to illuminate a rectangular area of 2.7 cm^2 when held 2 cm from a surface. Participants were seated and blindfolded. Audible frequencies emanating from the skin (Figure A.11) during the experiments were blocked with foam earplugs combined with noise-canceling headphones.

  The subjects were asked to place in foam earplugs and a blindfold. The subjects' hands were cleaned from any residues and the dye was applied corresponding to each experiment. Two coats of ICG dye were applied using a cotton swab and allowed to dry between coats. The black ink was directly applied onto the subjects' finger/s using a permanent marker (Sharpie Fine Point - Black). Noise-canceling headphones (RUNOLIM WH301A) were placed on the subjects' ears.

  A Python script was used to randomize the stimulation parameters.

- MDL experiments:

  The participant preparation for the MDL experiments was identical to that of the OPO experiments.

  - Mechanically chopped light (Experiments E-F):

    The mechanical laser chopper setup was built using a simple DC motor controlled using an Arduino microcontroller fitted with a motor control shield. Parts were designed in a 3D CAD software and printed on an FDM 3D printer using polylactic

acid (PLA) and flexible thermoplastic polyurethane (TPU) filaments. The laser socket was made to fit the various laser sizes examined allowing for easy swapping during the experiment. For thin fiber optic cables custom adapters were made to ensure a tight fit and minimize deviation.

  - Modulated light (Experiments D,F):

    The laser modulation signal was from a functional waveform generator (SIGILENT SDG 2042X) connected to the input of the MDL power supply. The MDL power supply was set to modulation mode, rather than CW. The fibre optic cable coming out of the MDL laser was fixed using a laboratory stand with a clamp attachment, so that the output of the fibre optic was pointed vertically downwards. The participant's hand was placed so that the palm was faced upwards on top of a piece of foam for comfort. The height of the fibre optic cable output was positioned so that it was 1.5 cm above the surface of the participant's fingers.

- DLP projector experiments (Experiments D,F):

  The participant preparation for the DLP projector experiments was identical to that of the OPO and MDL experiments.

  The DLP projector (OPTOMA HD146X) was fixed to a lab jack with 3D-printed parts to hold the projector to shine vertically downwards. The projector was strapped to the stand using large velcro straps. The fresnell lens was fixed at a distance of 17.8 cm from the output of the projector using 3D-printed parts. The lens captured less than half of the projected area at the used distance. A standard green projection was played as a video that was generated using Python OpenCV library. The color was chosen to reduce the time average intensity of the output; white (combination of all colors) light being the most intense. The height of the projector, determined by the height of the lab jack, was set so that the focal point of the lens landed on the surface of the participant's fingers. The participant's hand was placed so that the palm was faced upwards on top of a piece of

foam for comfort.

3.5.2 Characterization

Dye absorbance

ICG solid was dissolved into ethanol (4 mg ml^{-1}), and filtered through a 0.45 μm, 13 mm filter to remove aggregates. For a controlled comparison, black ink was extracted from a permanent marker (Sharpie Fine Point - Black) by placing the tip of a fresh marker into a vial of ethanol (20 ml) overnight. Glass slides (1" x 1") were cleaned in a sonication bath using the following wash sequence (Alconox solution, water, isopropanol). The slides were then dried and treated in a plasma cleaner (400 mTorr air, 3 minutes, 30 W) to activate the surface. The solution was spun on the glass slides at 600 rmp and 300 rpm s^{-1} (Figure A.13). Three samples were prepared of each dye.

The absorption spectra of each sample were obtained between 300 nm and 1000 nm (Aligent Cary UV-Vis Spectrophotometer). The thickness of the samples was evaluated at two points using ellipsometery (J.A. Woollam M-2000D Spectroscopic Ellipsometer). The thickness was used to normalize the absorption spectra. The absorption spectrum of a permanent marker drawn on a glass slide was also obtained to rule out any inadvertent changes to the marker ink during extraction (Figure A.14).

Audio measurements

A willing subject's index, middle, and ring finger were prepared in a manner similar to the thermography experiments. The hand was placed in a box padded with noise insulation. A lapel microphone without a pop filter was placed inside the box behind the location of the laser to avoid any photoacoustic effects on the microphone surface. The audio jack of the microphone was connected to a SONY Alpha 7R camera. The laser was applied on the different dyes and bare finger while the audio was recording. This experiment was repeated for bare and inked

(ICG and black ink) fingers for both wavelengths. To capture the ambient noise generated by the laser, the laser probe was pointed away from the subject and held far away ($>$ 1 m) from any surfaces. The audio was collected from the video recordings. A 10kHz high pass filter (24 dB) was applied to the audio data to remove the background machine noise.

Thermography

A willing subject's index and ring fingers were coated with black ink and ICG respectively, the middle finger was set as the control (bare). A thermographic camera (HIKMICRO Pocket 2) was affixed on a stand to measure the temperature of the finger tip at the laser's area of incidence. The ambient temperature was input into the camera settings and the emissivity was validated by comparing the temperature with a thermocouple output (Fluke t3000 FC). Each finger was illuminated with the laser source using the OPO with identical wavelengths and pulse settings used in the psychophysical experiments for ca. 3 minutes. The laser was then turned off to observe the cooling effect. The thermographic data was extracted from the video footage using MATLAB Image Processing Toolbox and Computer Vision Toolbox. The data was smoothed using a moving mean (20 samples) and plotted against the time signature of the frame.

OPO power measurements

To first measure pulse frequency, an oscilliscope (TDS2022C) was connected to a biased photodetector (Thorlabs DET10A2 200 - 1100 nm). The OPO laser was pointed directly at the center of the detector sensor and was set to pulse 680 nm wavelength light. The oscilloscope captured the sensor power readings (Figure A.18). Confirmed by the manufacturer, the OPO laser, while at a 20 Hz pulse repetition rate, skips a pulse every 4 pulses, resulting in 16 pulses every second. To calculate a peak fluence, we measured a beam spot at 1.5 cm away from the target of 2.7 cm^2, and calculated a peak fluence of 13.3 mJ cm^{-2} given the technical specification of 45 mJ peak energy for a 20 Hz 4-6 ns pulse, provided by the OPO manufacturer.

MDL power and pulse measurements

The output power of the MDL laser, immediately after exiting the optical laser, was calculated to be approximately 2.29 W. This calculation was based on a maximum source power of 2.5W, with an estimated power loss of 9.95 % through the optical fiber. To observe the pulse profiles for the chopped and modulated MDL light, a digital power meter (Thorlabs PM100D) and a compatible photodiode sensor (Thorlabs S120VC) were fixed on an optical platform, in the direct line of sight of the optic fiber cable output. The modulation or chopping were started, and laser energized. The output signal was observed and collected using a digital oscilloscope (RIGOL DS1054 Z) and then normalized by the maximum power. Modulation was varied from the parameters used for stimulation to ensure the chosen modulation frequency did not affect maximum power.

The beam diameter was estimated at $\frac{1}{e^2}$ of the maximum intensity. The beam was approximated to have a near-gaussian distribution with speckle observed. To obtain the $\frac{1}{e^2}$ beam diameter, the fiber optic beam was placed 1.5 cm away from the photodiode, and the current setting was lowered to avoid sensor damage. An optical chopper wheel was used to scan the beam (Thorlabs MC2000B) at 20Hz. The blade (Thorlabs MC1F10HP) was placed in between the beam and sensor and an intensity profile was obtained. The intensity profile was then used to calculate the diameter (1.28 cm). The fluence was calculated using the pulse parameters and beam diameter.

DLP projector power and pulse measurements

All measurement components were secured to an aluminum optical breadboard with the projector-to-lens distance and lens-to-photodiode distances set to 17.8 cm. To avoid input saturation, a neutral density filter (NE60A) with an optical density of 6.0 was attached to the diode input. The power meter's attenuation was adjusted to 60.00 dB to correct for the attenuation from the ND filter. Given that the photodiode exhibits a linear responsivity curve within the visible light regime, the measurement was set to be at a wavelength of 540 nm on the power meter,

corresponding to the central wavelength of the UV-vis absorption spectrum of the projector's green color filter (Figure A.15). During data acquisition, the projector was set to a standard green screen, and the average power reading was recorded. A "continuous" green screen showed a pulsing pattern consistent with the DLP refresh rate which was averaged by the power meter. For digital pulse characterization, the projector and photodiode were positioned 35.6 cm apart, with no other optical components interposed. The pulse waveforms were captured on an oscilloscope connected to the output of the power meter for both "continuous" and pulsed light (operating at 15 Hz with a pulse width of 16.7 ms). The photodiode power sensor, digital power meter, and oscilloscope used for these measurements were identical to those mentioned previously. Using the power measured for the "continuous" DLP projector light (310 mW), we calculated a peak fluence of 10.3 mJ cm^{-2} using the 15 Hz pulse repetition rate, 16.7 ms pulse width, and measured beam spot (~ 0.5 cm^2).

3.6 Acknowledgements

Chapter 3, in full, has been submitted for publication of the material as it may appear in Advanced Science, 2024, Rafeedi, Tarek*; Becerra, Laura L.*; Root, Nicholas; Qie, Yi; Brown, William; Qi, Baiyan; Fu, Lei; Esparza, Guillermo; Sasi, Lekshmi; Kapadia, Kabir; Rouw, Romke; Jokerst, Jesse; Lipomi, Darren J. The dissertation author was one of the co-primary investigators and author of this paper, along with Tarek Rafeedi, who was an equal contributor. The dissertation author and Tarek Rafeedi both contributed to the design and execution of the experiments, processed the data, and wrote this chapter.

Appendix A

Appendix

A.1 Chapter 1 Supplementary Information

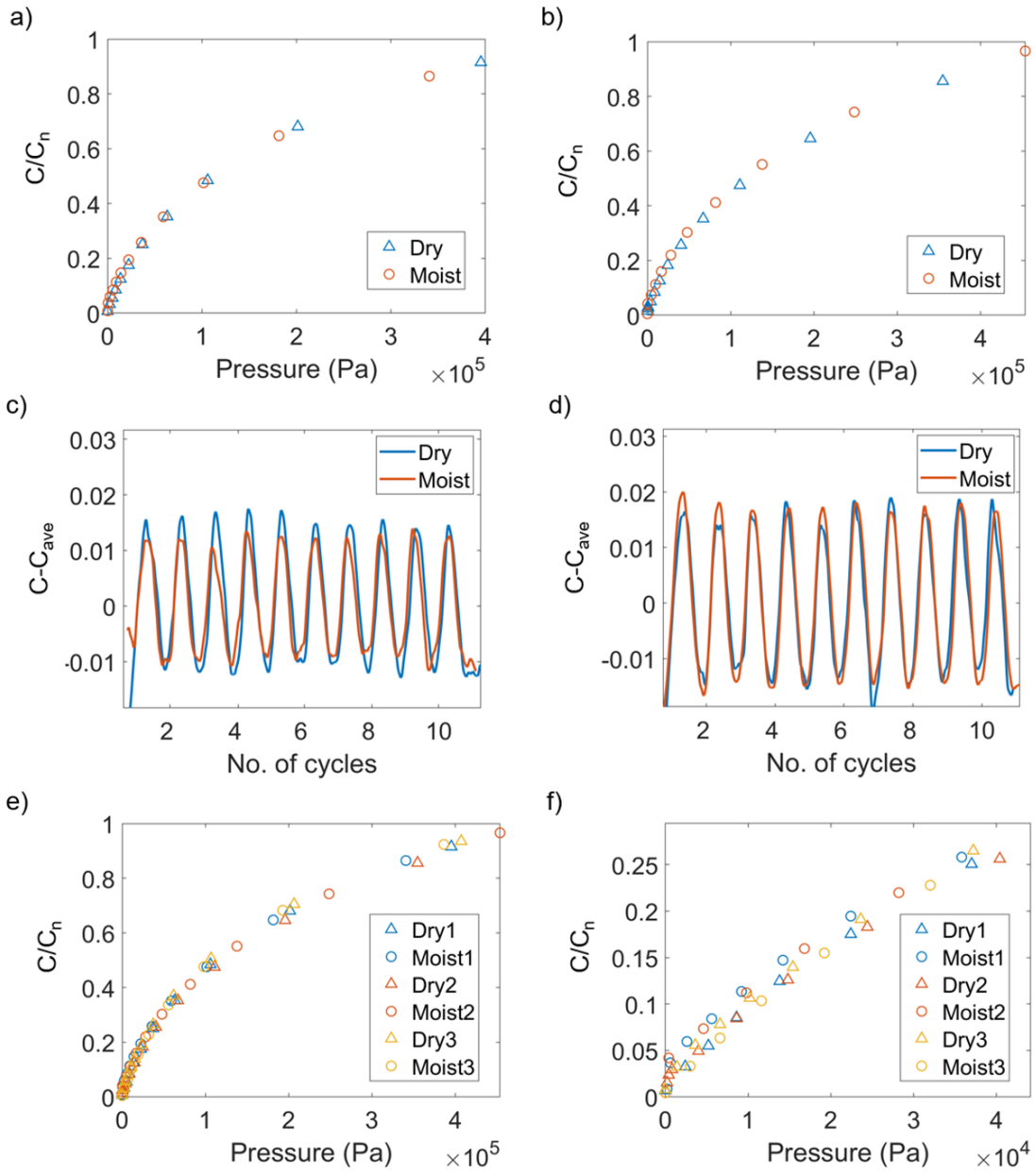


Figure A.1. Sensor performance with humidity exposure a) and **b)** show the calibration curves for two different sensors before and after they were exposed to 40-88% humidity for 30 minutes. **c)** and **d)** are 10 cycles of compression for the same sensors in **a)** and **b)** before and after humidity exposure. **e)** shows overlapping calibration curves for 3 sensors before and after humidity exposure. **f)** shows a zoomed-in plot from **e)**.

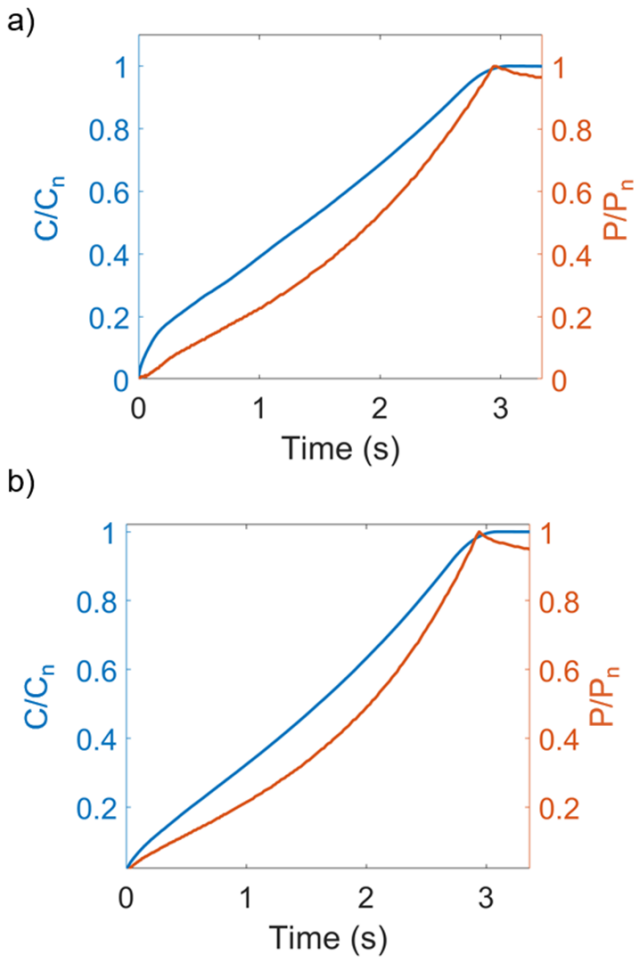


Figure A.2. Sensor response time a) and **b)** show capacitance readout of a sensor overlapped with the pressure being applied to the sensor as it is being compressed.

Table A.1. Commercial peak flow meter data (Microlife PF100)

Trials	Peak expiratory flow measurement (L min^{-1})	Peak expiratory flow measurement (L s^{-1})	Deep breathing peak measurement (L min^{-1})	Deep breathing peak measurement (L s^{-1})
1	420	7.00	249	4.15
2	413	6.88	238	3.97
3	426	7.10	229	3.82
4	449	7.48	214	3.57
5	442	7.37	166	2.77
6	462	7.70	228	3.80
7	437	7.28	236	3.93
8	471	7.85	234	3.90
9	427	7.12	239	3.98
10	447	7.45	247	4.12
Average	**439**	**7.32**	**228**	**3.80**
Standard deviation	**18.5**	**0.31**	**23.95**	**0.40**

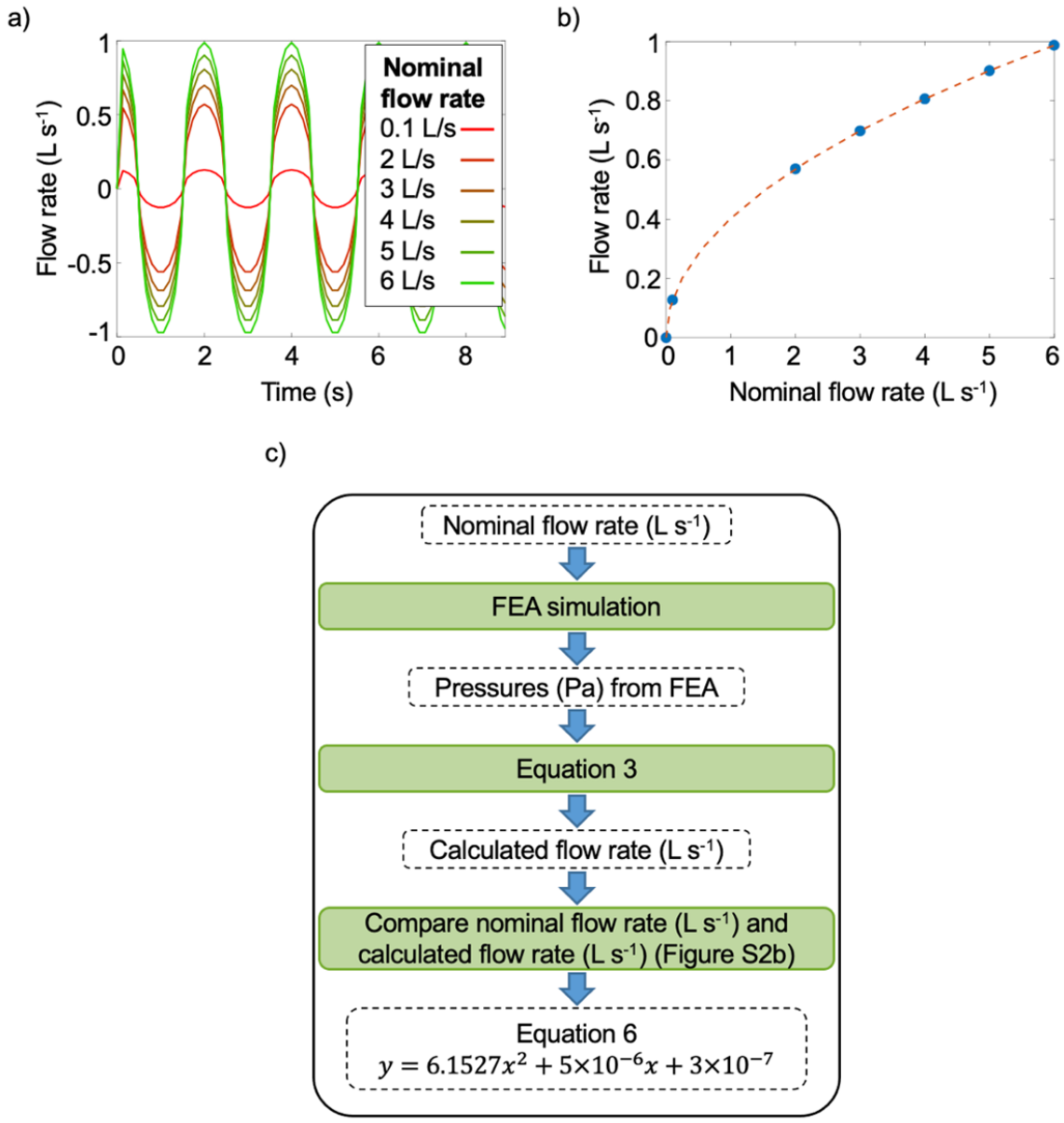


Figure A.3. a) Flow rates over time from simulation pressures plugged into Equation 1.3 in the main text for each corresponding nominal flow rate. **b)** Output flow rate as a function of nominal flow rate. **c)** Flow diagram for flow rate adjustment.

Figure 1.7 a and b show the calculated flow rates using Equation 1.3 from the pressures at the sensor locations and the nominal flow rates as the input. This discrepancy was corrected for using the methods illustrated in Figure 1.9. Equation 1.6 was found from comparing the relationship between the nominal flow rates to the calculated flow rates from Equation 1.3. Figure

1.8 shows an image the fluid density throughout the tube in simulation. Since the acoustics module used assumes compressibility, this causes variable density throughout the tube, while Bernoulli's principle in Equation 1.3 assumes incompressibility. This is another likely reason for the necessity of the flow rate scale factor (S_f).

Table A.2. Simulation values of FEA differential pressure peaks

Inlet flow rate (L min^{-1})	Inhale peak pressure (Pa)	Exhaled peak pressure (Pa)
0.1	0.06	0.06
2	1.14	1.19
3	1.72	1.78
4	2.29	2.37
5	2.86	2.97
6	3.43	3.56

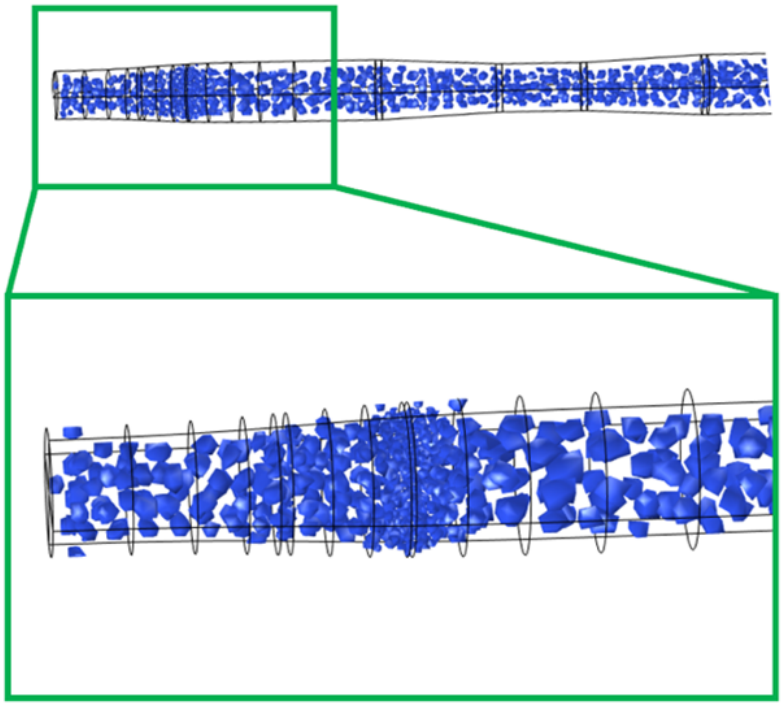


Figure A.4. Fluid density of spirometer tube in simulation.

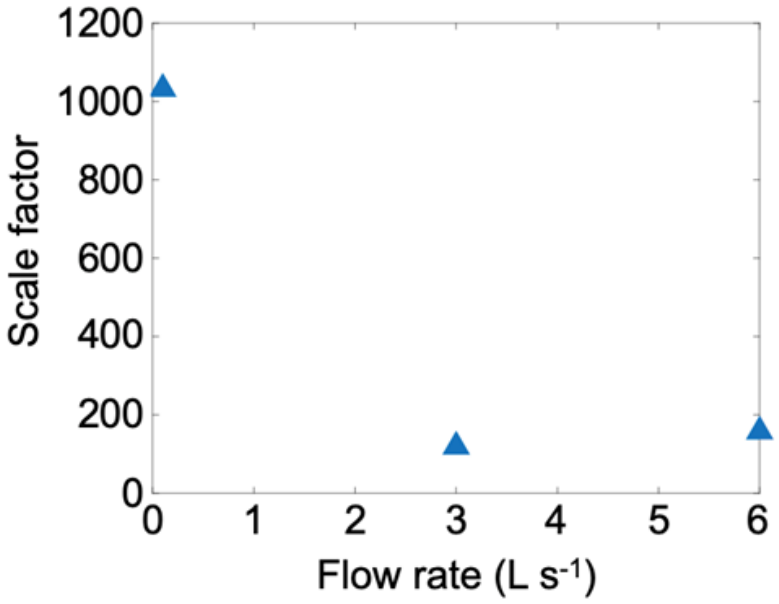


Figure A.5. The ratio of experimental differential peak pressure to simulated differential peak pressure are plotted against the flow rates corresponding to the expected flow rates for tidal, deep, and PEFR breathing measurements. The ratios are an average for inhale and exhale differential pressure signals.

To determine the differential pressure scale factor, we calculated the peak pressure values for each inhale and exhale pressure signal for the six flow rates shown in Table A.2. Figure 1.4 in the main text shows the pressure peaks (inhale and exhale values averaged together for each flow rate) against flow rates. The linear fits allowed us to extrapolate the expected pressure peaks for the average peak expiratory flow rate (PEFR) value from Table A.1 measured with the commercial peak flow meter. We used Equation 1.7 to apply the same adjustment factor to each tidal and deep-breathing dataset. For the PEFR flow rate, we used the linear trendline function Equation 1.7 to calculate the corresponding pressure peaks for inhalation and exhalation data for the average PEFR value in Table A.1, (7.3233 L s^{-1}). Figure A.5 visually summarizes the scaling factor input and output differential pressure peak plots, determined from the previously described methods. Figure 1.9 shows the scale factors as a function of flow rate for the three types of breathing (tidal, deep, and PEFR measurement).

Minimum tube length before first sensor to ensure fully developed turbulent flow:

$$L = Re^{0.25} \times 1.359 \times D \tag{A.1}$$

L = tube length before first sensor (m) D = diameter of inlet (m)

For tidal breathing:

$$L = 2600^{0.25} \times 1.359 \times 0.02 \tag{A.2}$$

$L = 19.14m$

For deep breathing and PEFR measurements:

$$L = 13200^{0.25} \times 1.359 \times 0.02 \tag{A.3}$$

$L = 29.13cm$

A.2 Chapter 2 Supplementary Information

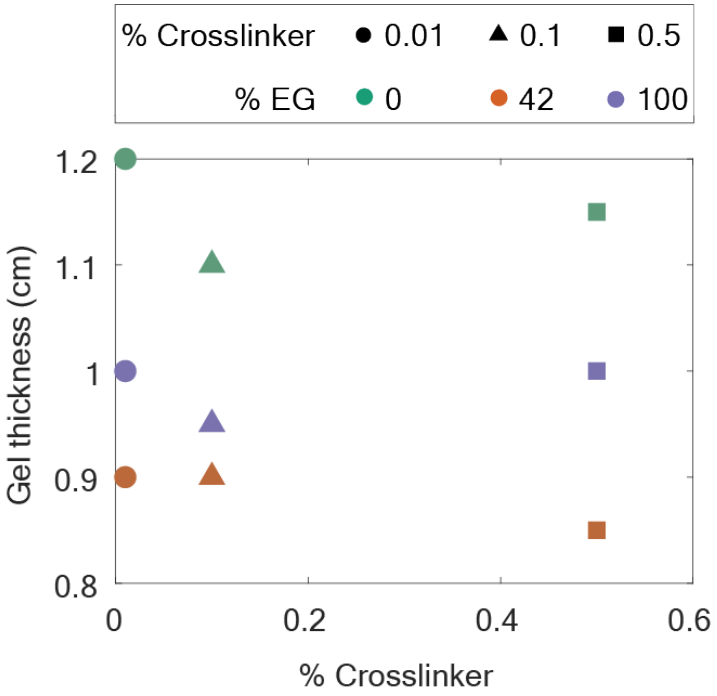


Figure A.6. Gel thickness measurements. NOTE: Legend information is taken from Figure 2.2 of the main text.

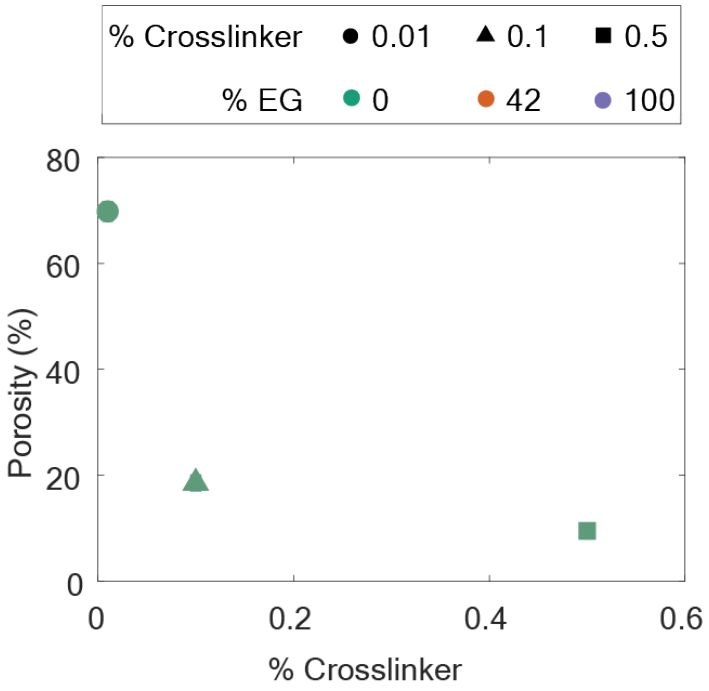


Figure A.7. Gel porosity. NOTE: Legend information is taken from Figure 2.2 of the main text.

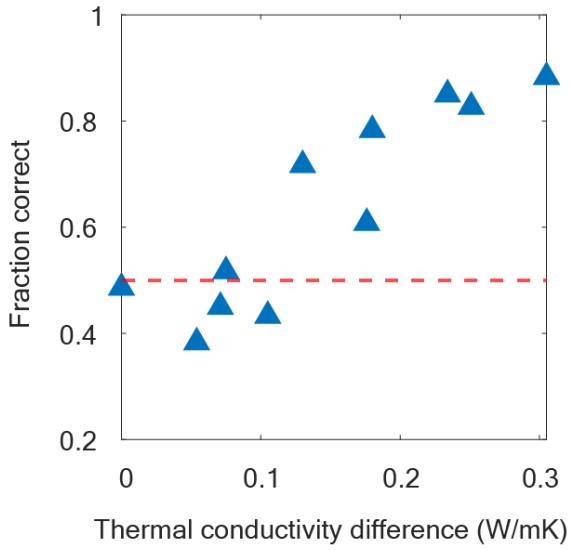


Figure A.8. Pilot experiment for thermal conductivity threshold.

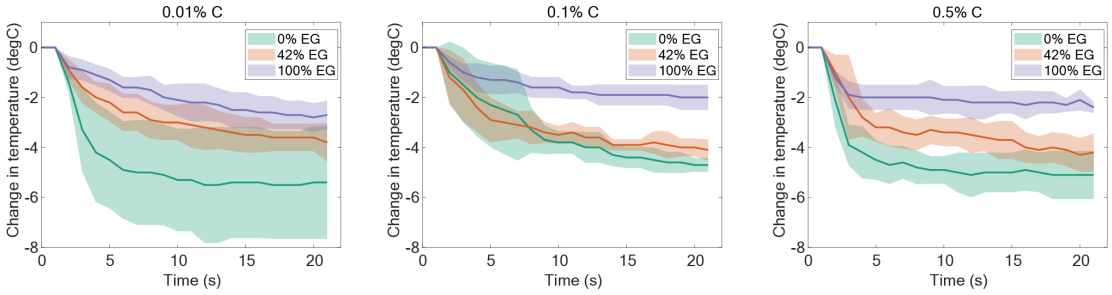


Figure A.9. Skin-gel temperature curves.

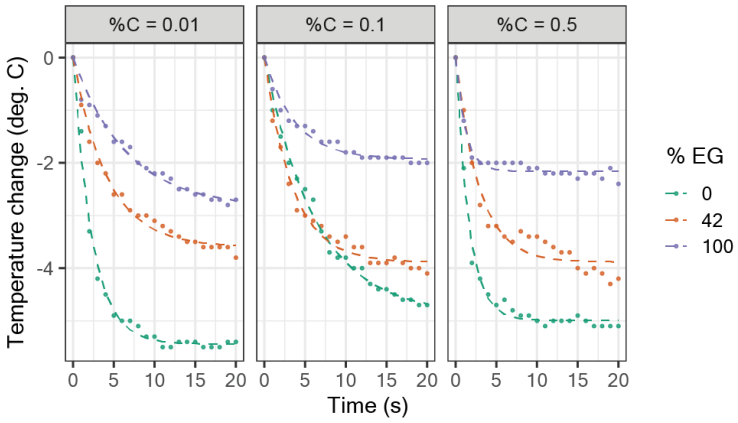


Figure A.10. Function-fitted skin-gel temperature curves.

A.3 Chapter 3 Supplementary Information

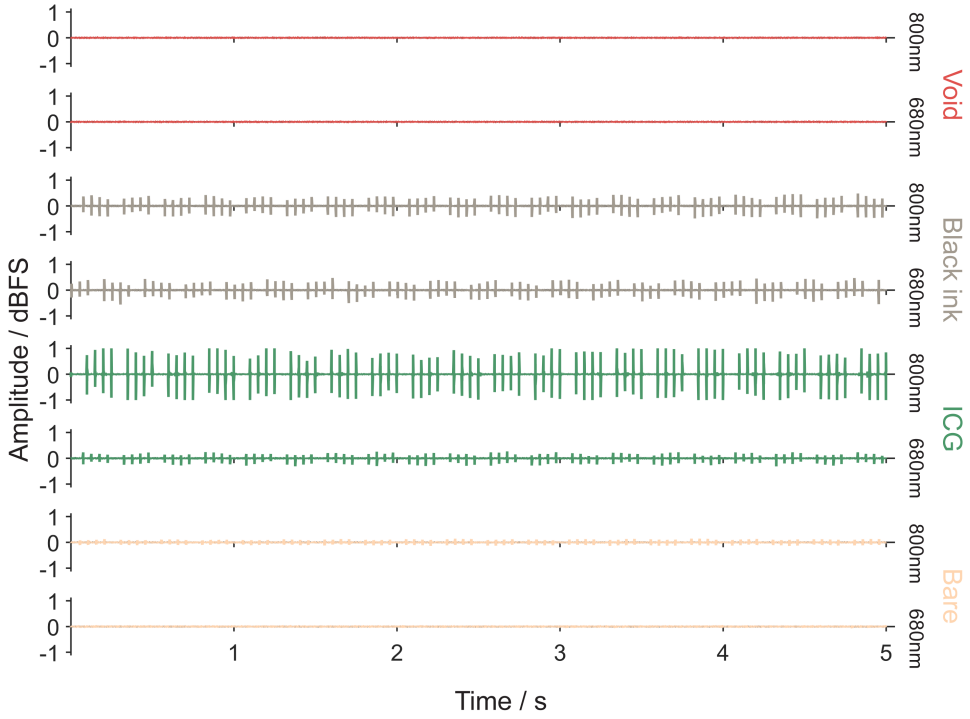


Figure A.11. Graphical representation of the audio signals generated by OPO pulses (800 nm and 680 nm) incident on inked (black ink and ICG) fingers, bare finger, and void. Note: The OPO laser skips a pulse every 4 pulses (16 pulses per second), though still pulsing at 20 Hz (see Figure A.18).

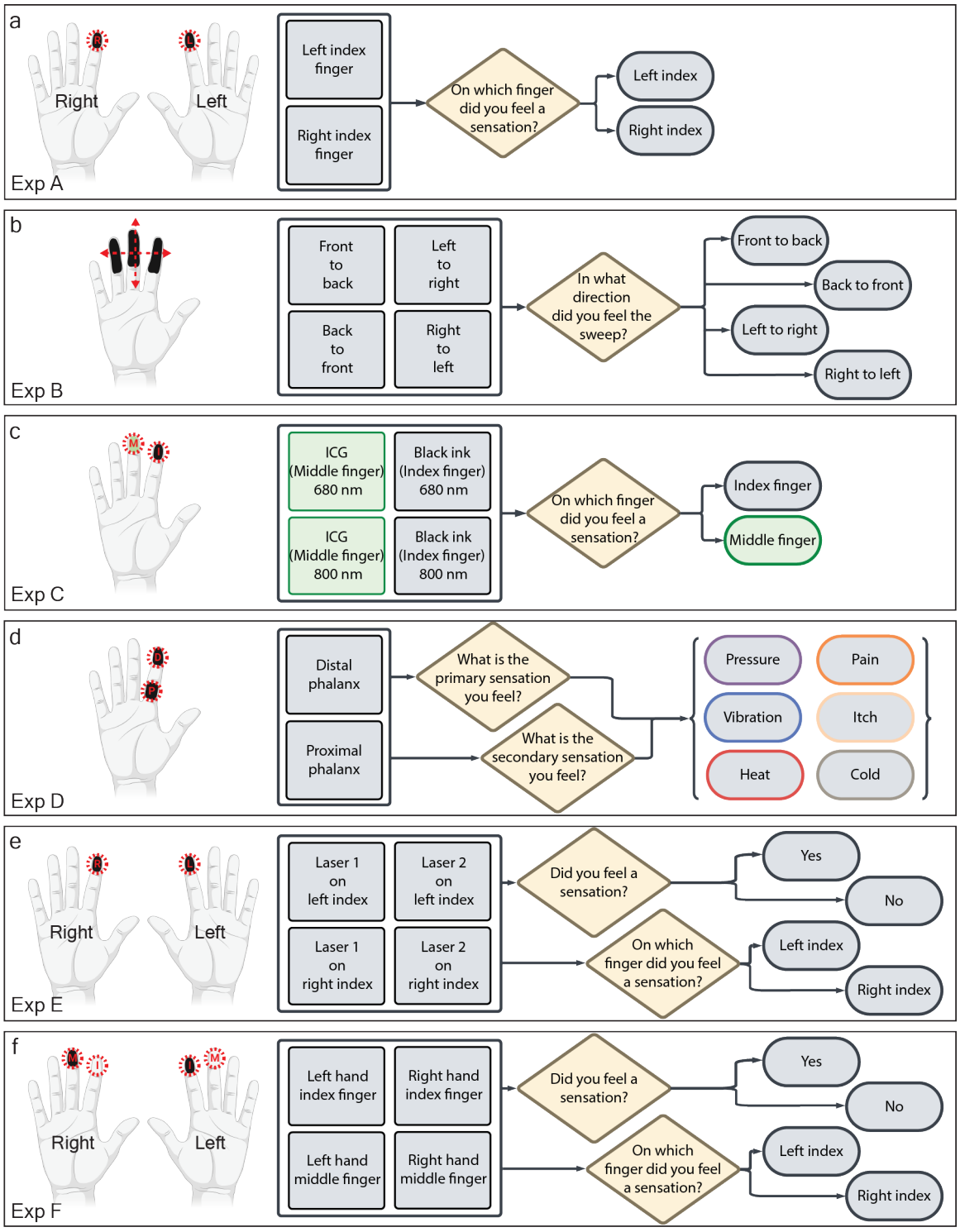


Figure A.12. Schematic (left) and flowchart (right) description of laser experiments for: a) Experiment A (OPO) **b)** Experiment B (OPO) **c)** Experiment C (OPO) **d)** Experiment D (OPO, MDL (modulated), DLP) **e)** Experiment E (MDL chopped) **f)** Experiment F (MDL (chopped and modulated), DLP).

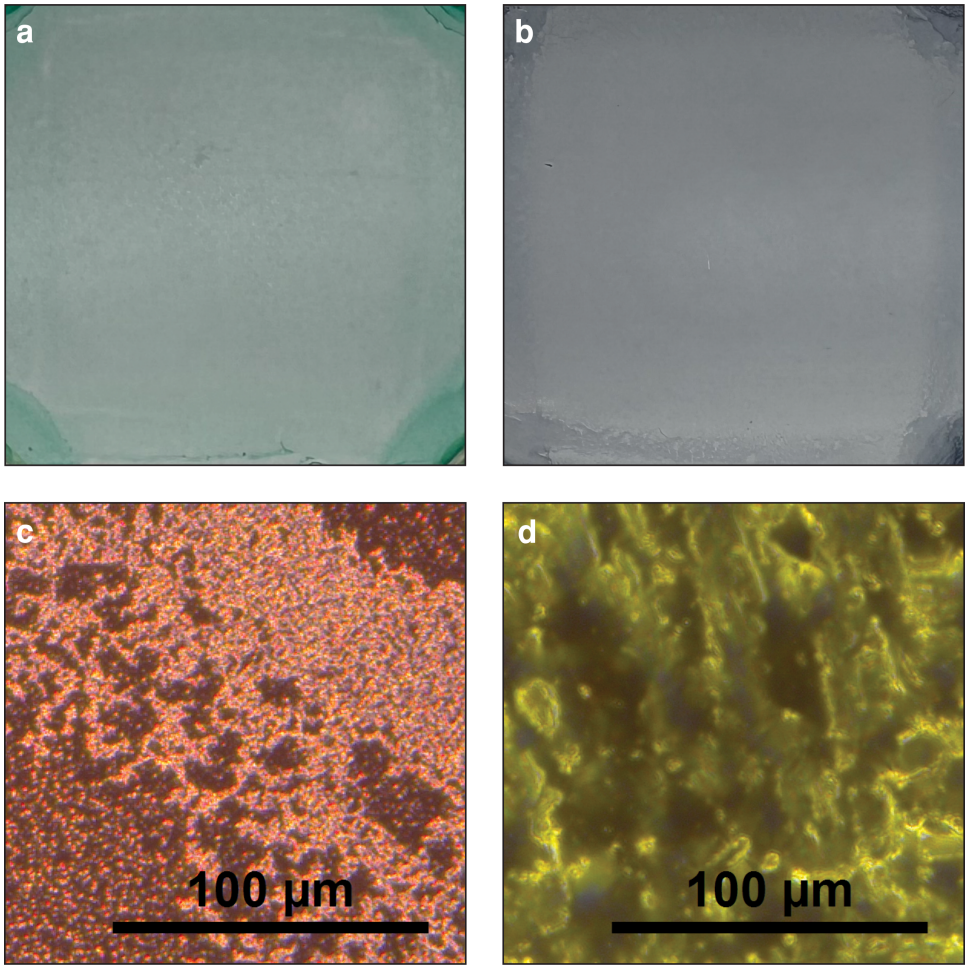


Figure A.13. Photographic and optical microscopy images of spin-cast dye films. **a)** Photograph of ICG film on glass substrate. **b)** Photograph of black ink film on glass substrate. **c)** Corresponding ICG film dark field optical microscopy image. **d)** Corresponding black ink film dark field optical microscopy image.

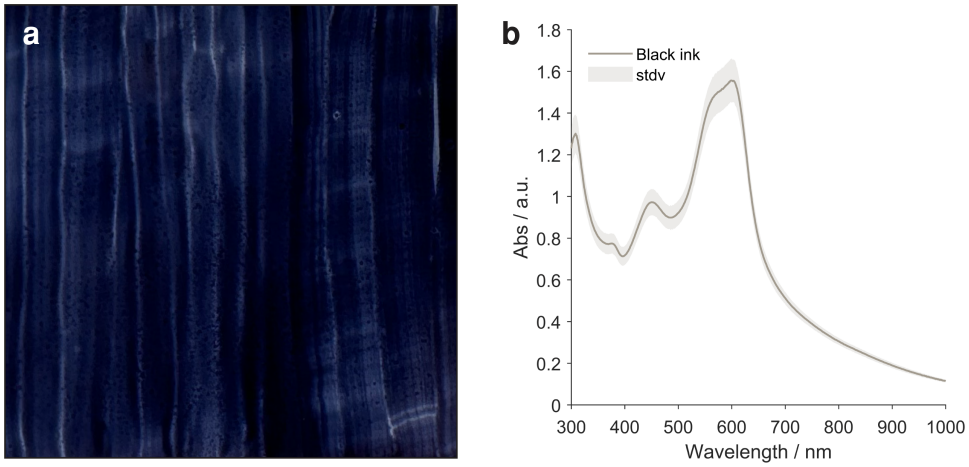


Figure A.14. Photographic and absorbance spectrum representations of black ink drawn on a glass slide. a) Photograph of black ink film hand drawn on glass substrate. **b)** Absorbance spectrum of black ink drawn film not normalized by thickness.

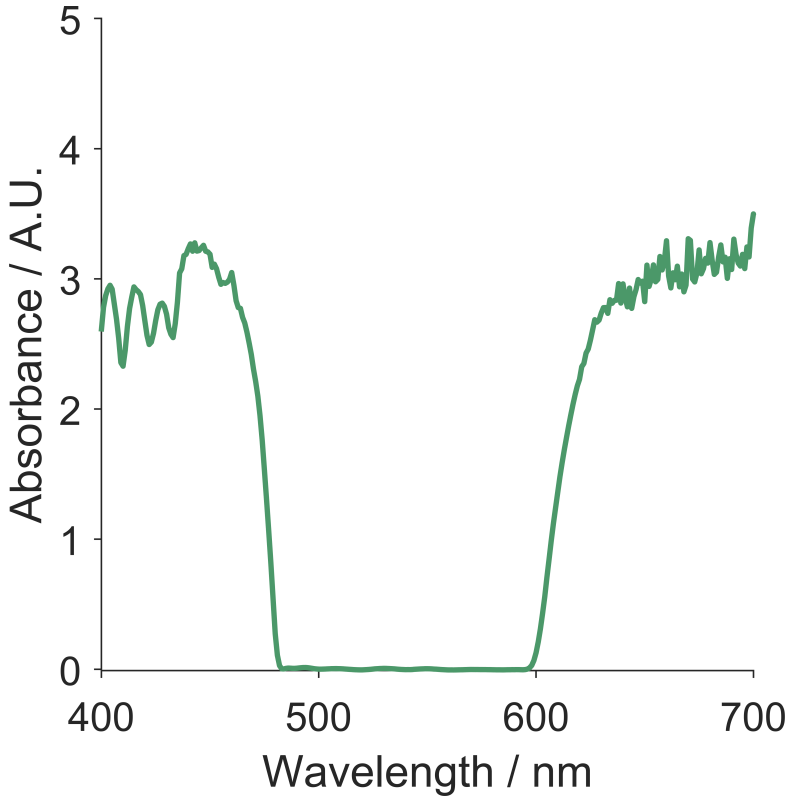


Figure A.15. Absorbance spectra of DLP projector green light.

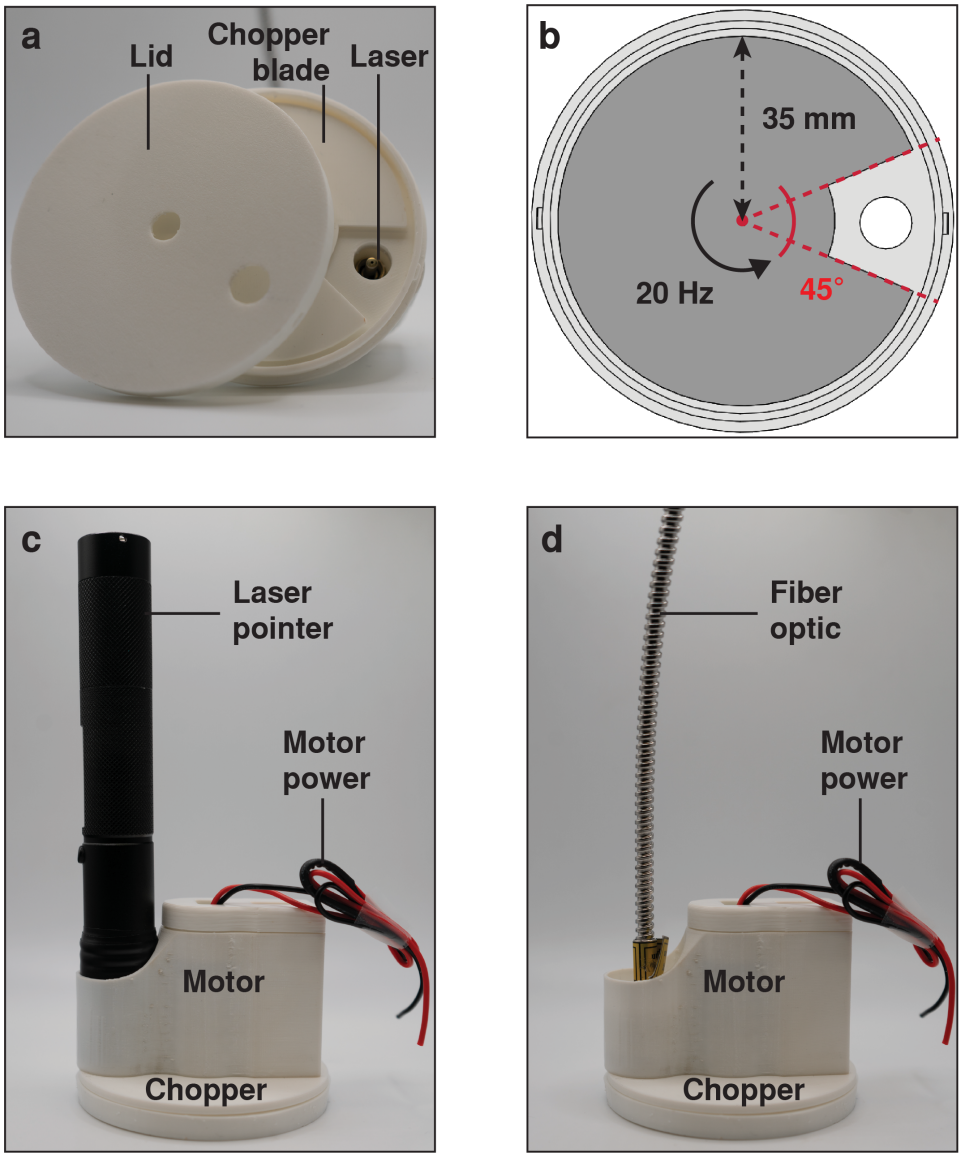


Figure A.16. Photographic and schematic details of the hand-held laser chopper. **a)** Chopper assembly showing the laser aperture, chopper blade, and protective lid. **b)** Chopper blade schematic showing the angle of the chopper window (aligned with aperture) and the diameter of the blade. **c)** Handheld chopper assembled with laser pointer in the socket. **d)** Handheld chopper assembled with fiber optic cable in the socket.

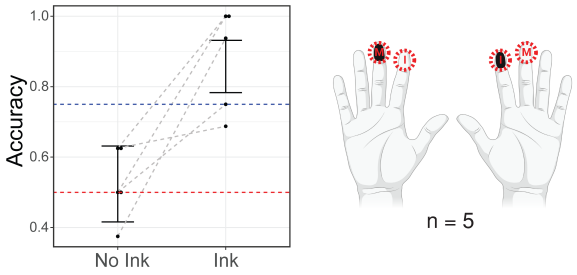


Figure A.17. Accuracy of participants' ability to detect the haptic effect with and without ink using chopped MDL light. Error bar confidence intervals and chance performance are the same as those for Figure 3.3c

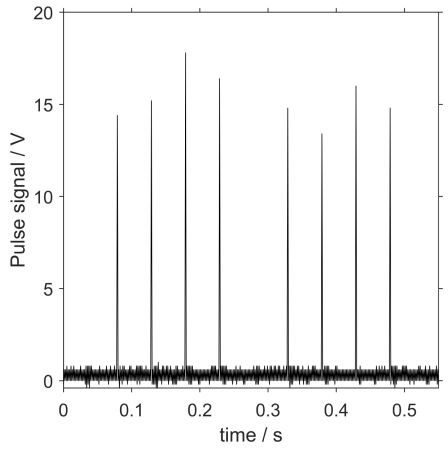


Figure A.18. OPO laser power pulse signal.

Table A.3. Exp. C: General Linearized Mixed Model (GLMM) results.

Term	Coefficient	Std. Err.	Wald Z	p value
Intercept	7.37	3.22	2.29	0.02
Wavelength (800 nm)	0.47	0.98	0.48	0.63
Ink (Black)	2.52	1.15	2.19	0.03
Ink * Wavelength	0.15	1.49	0.10	0.92

Table A.4. Exp. C: GLMM Estimated Marginal Means (EMMs) of each condition. Values are back-transformed from the logit scale. Tests are performed on the logit scale

Wavelength	Ink	Accuracy EMM	Accuracy EMM 95%CI	Wald Z	p value
680	ICG	>0.99	[0.74, 1.00]	2.29	0.02
800	ICG	>0.99	[0.80, 1.00]	2.38	0.02
680	Black ink	>0.99	[0.96, 1.00]	2.86	0.004
800	Black ink	>0.99	[0.98, 1.00]	3.01	0.003

Table A.5. Exp. E: GLMM Estimated Marginal Means (EMMs) of each condition. Values are back-transformed from the logit scale. Tests are performed on the logit scale.

Laser	Accuracy EMM	Accuracy EMM 95%CI	Wald Z	p value
MDL 808 nm	0.91	[0.78, 0.97]	4.30	< 0.001
Laser pointer	0.44	[0.28, 0.61]	0.72	0.47

Table A.6. Exp. F (Mechanically chopped): GLMM Estimated Marginal Means (EMMs) of each condition. Values are back-transformed from the logit scale. Tests are performed on the logit scale.

Laser	Accuracy EMM	Accuracy EMM 95%CI	Wald Z	p value
No ink	0.53	[0.42, 0.63]	0.45	0.65
Ink	0.88	[0.78, 0.93]	5.76	$<$0.001

Table A.7. Spin-cast dye film thicknesses obtained by ellipsometry. Each film sample was measured at two separate points denoted by the header: "thickness".

	Thickness 1 (nm)	Thickness 2 (nm)	Mean thickness (nm)
		ICG	
Sample 1	76.52	60.09	68.31
Sample 2	65.79	71.03	68.41
Sample 3	48.44	45.07	46.76
		Black ink	
Sample 1	86.05	68.63	77.34
Sample 2	68.26	57.26	62.76
Sample 3	65.37	68.37	66.87

Table A.8. Total rectangular area of OPO laser beam projected over different distances.

Distance (mm)	Area (mm^2)
20	ca. 270
100	ca. 990

Bibliography

[1] L. E. Flinterman, A. I. González-González, L. Seils, J. Bes, M. Ballester, J. Bañeres, S. Dan, A. Domagala, K. Dubas-Jakóbczyk, and R. Likic, "Characteristics of medical deserts and approaches to mitigate their health workforce issues: A scoping review of empirical studies in western countries," *International Journal of Health Policy and Management*, vol. 12, p. 7454, Aug 2023.

[2] A. Kaushik and M. A. Mujawar, "Point of care sensing devices: Better care for everyone," *Sensors*, vol. 18, no. 12, 2018.

[3] G. A. Gescheider, *Psychophysics: The Fundamentals*. Lawrence Erlbaum Associates, Inc., 3 ed., 1997.

[4] M. Shibahara and K. Sato, "Illusion of wet sensation by controlling temperature and softness of dry cloth," in *Haptics: Perception, Devices, Control, and Applications* (F. Bello, H. Kajimoto, and Y. Visell, eds.), (Cham), pp. 371–379, Springer International Publishing, 2016.

[5] C. Fan and Z. Zhang, "Comparison of reality and illusion of wetness on soft materials and the multisensory perceptual space of wetness illusion," *Textile Research Journal*, p. 00405175241226619, Jan. 2024.

[6] H. Culbertson, S. B. Schorr, and A. M. Okamura, "Haptics: The present and future of artificial touch sensation," *Annual Review of Control, Robotics, and Autonomous Systems*, vol. 1, no. Volume 1, 2018, pp. 385–409, 2018.

[7] H. Gurocak, S. J. , B. P. and, and U. Jayaram, "Weight sensation in virtual environments using a haptic device with air jets," *Journal of Computing and Information Science in Engineering*, vol. 3, pp. 130–135, 6 2003.

[8] Y. Ochiai, K. Kumagai, T. Hoshi, S. Hasegawa, and Y. Hayasaki, "Cross-field aerial haptics," pp. 3238–3247, ACM, 5 2016.

[9] X. Lu, Y. Yan, B. Qi, H. Qian, J. Sun, and A. Quigley, "Contactless haptic display through magnetic field control," *IEEE Transactions on Haptics*, vol. 15, no. 2, pp. 328–338, 2022.

[10] I. Rakkolainen, E. Freeman, A. Sand, R. Raisamo, and S. Brewster, "A survey of mid-air ultrasound haptics and its applications," *IEEE Transactions on Haptics*, vol. 14, pp. 2–19, 1 2021.

[11] J.-H. Jun, J.-R. Park, S.-P. Kim, Y. Min Bae, J.-Y. Park, H.-S. Kim, S. Choi, S. J. Jung, S. Hwa Park, D.-I. Yeom, G.-I. Jung, J.-S. Kim, and S.-C. Chung, "Laser-induced thermoelastic effects can evoke tactile sensations," *Scientific Reports*, vol. 5, p. 11016, June 2015.

[12] C. S. Sunandana, "Physical applications of photoacoustic spectroscopy," *Physica Status Solidi (a)*, vol. 105, pp. 11–43, 1988.

[13] H.-S. Kim, J.-S. Kim, G.-I. Jung, J.-H. Jun, J.-R. Park, S.-P. Kim, S. Choi, S.-J. Park, M.-H. Choi, and S.-C. Chung, "Evaluation of the possibility and response characteristics of laser-induced tactile sensation," *Neuroscience Letters*, vol. 602, pp. 68–72, 2015.

[14] M.-H. CHOI, H.-S. KIM, J.-H. JO, J.-S. KIM, J.-H. JUN, J.-R. PARK, and S.-C. CHUNG, "Interaction effect between beam diameter and energy density in laser-induced tactile perception," *Journal of Mechanics in Medicine and Biology*, vol. 18, p. 1840011, Nov 2018.

[15] H. Lee, J.-S. Kim, J.-Y. Kim, S. Choi, J.-H. Jun, J.-R. Park, A.-H. Kim, H.-B. Oh, J.-H. Baek, S.-J. Yang, H.-S. Kim, and S.-C. Chung, "Mid-air tactile stimulation using indirect laser radiation," *IEEE Transactions on Haptics*, vol. 9, no. 4, pp. 574–585, 2016.

[16] D. Hoesterey, N. Das, W. Janssens, R. G. Buhr, F. J. Martinez, C. B. Cooper, D. P. Tashkin, and I. Barjaktarevic, "Spirometric indices of early airflow impairment in individuals at risk of developing copd: Spirometry beyond fev1/fvc," *Respiratory Medicine*, vol. 156, pp. 58–68, 2019.

[17] B. P. Yawn, P. L. Enright, R. F. Lemanske, E. Israel, W. Pace, P. Wollan, and H. Boushey, "Spirometry can be done in family physicians' offices and alters clinical decisions in management of asthma and copd," *Chest*, vol. 132, no. 4, pp. 1162–1168, 2007.

[18] M. C. McCormack and D. A. Kaminsky, "Pulmonary function laboratories: Advice regarding covid-19."

[19] B. L. Graham, I. Steenbruggen, M. R. Miller, I. Z. Barjaktarevic, B. G. Cooper, G. L. Hall, T. S. Hallstrand, D. A. Kaminsky, K. McCarthy, M. C. McCormack, C. E. Oropez, M. Rosenfeld, S. Stanojevic, M. P. Swanney, and B. R. Thompson, "Standardization of spirometry 2019 update. an official american thoracic society and european respiratory society technical statement," *American Journal of Respiratory and Critical Care Medicine*, vol. 200, no. 8, pp. e70–e88, 2019. PMID: 31613151.

[20] K. M. Gulla and S. K. Kabra, "Peak Expiratory Flow Rate as a Monitoring Tool in Asthma," *The Indian Journal of Pediatrics*, vol. 84, pp. 573–574, Aug. 2017.

[21] R. Patil, S. N, and V. Veena, "Peak flow meter and digital spirometer: A comparative study of peak expiratory flow rate values," *National Journal of Physiology, Pharmacy and Pharmacology*, vol. 10, p. 508–510, May 2020.

[22] Fung, Tan, Duong, Schivo, Littlefield, Delplanque, Davis, and Kenyon, "Design and Benchmark Testing for Open Architecture Reconfigurable Mobile Spirometer and Exhaled Breath Monitor with GPS and Data Telemetry," *Diagnostics*, vol. 9, p. 100, Aug. 2019.

[23] T. Z. Rondinel, I. F. Corrêa, L. M. Hoscheidt, M. H. Bueno, L. M. C. D. Silva, C. T. Reppold, and P. Dal Lago, "Incentive spirometry combined with expiratory positive airway pressure improves asthma control and quality of life in asthma: a randomised controlled trial," *Journal of Asthma*, vol. 52, pp. 220–226, Feb. 2015.

[24] R. Bastin, J.-J. Moraine, G. Bardocsky, R.-J. Kahn, and C. Mélot, "Incentive spirometry performance: A reliable indicator of pulmonary function in the early postoperative period after lobectomy?," *Chest*, vol. 111, no. 3, pp. 559–563, 1997.

[25] A. Sinharay, R. Rakshit, A. Khasnobish, T. Chakravarty, D. Ghosh, and A. Pal, "The Ultrasonic Directional Tidal Breathing Pattern Sensor: Equitable Design Realization Based on Phase Information," *Sensors*, vol. 17, p. 1853, Aug. 2017.

[26] T. Koutsis, P. Pikasis, A. Psyrris, and G. Kaltsas, "A thermal flow sensor with a 3d printed housing for spirometry applications," *Microelectronic Engineering*, vol. 226, p. 111286, 2020.

[27] M. Beyaz, S. Habibiabad, H. Yıldız, U. Göreke, and K. Azgın, "A turbine-based mems sensor for spirometry with wearable devices," *IEEE Sensors Journal*, vol. 19, no. 19, pp. 8612–8617, 2019.

[28] T. Yoshida, Y. Hamada, S. Nakamura, Y. Kurihara, and K. Watanabe, "Spirometer Based on Vortex Whistle to Monitor Lung Disorders," *IEEE Sensors Journal*, vol. 22, pp. 11162–11172, June 2022.

[29] C. W. Carspecken, C. Arteta, G. D. Clifford, B. Engineering, and E. Science, "TELESPIRO : A LOW-COST MOBILE SPIROMETER FOR RESOURCE-LIMITED SETTINGS Department of Medical Education , Harvard Medical School , Boston MA , United States," *Point-of-Care Healthcare Technologies (PHT), 2013 IEEE*, pp. 16–18, 2013. Publisher: IEEE.

[30] K. Adamski, B. Kawa, and R. Walczak, "3D Printed Flowmeter Based on Venturi Effect with Integrated Pressure Sensors," *Proceedings*, vol. 2, no. 13, pp. 1509–1509, 2018.

[31] B. Zhou, A. B. Costa, and P. Lukowicz, "Accurate spirometry with integrated barometric sensors in face-worn garments," *Sensors (Switzerland)*, vol. 20, no. 15, pp. 1–22, 2020.

[32] B. Zhang, Y. Tang, R. Dai, H. Wang, X. Sun, C. Qin, Z. Pan, E. Liang, and Y. Mao, "Breath-based human–machine interaction system using triboelectric nanogenerator," *Nano Energy*, vol. 64, p. 103953, Oct. 2019.

[33] M. Wang, J. Zhang, Y. Tang, J. Li, B. Zhang, E. Liang, Y. Mao, and X. Wang, "Air-Flow-Driven Triboelectric Nanogenerators for Self-Powered Real-Time Respiratory Monitoring," *ACS Nano*, vol. 12, pp. 6156–6162, June 2018.

[34] J. C. Alvarez, C. Raymundo, G. Zapata, J. Ronceros, M. Flores, and F. Ruiz, "Patented portable spirometer based on fluid mechanics and low energy consumption to monitor rehabilitation of Covid-19 patients," *Energy Reports*, vol. 6, no. June, pp. 179–188, 2020. Publisher: Elsevier Ltd.

[35] R. Carta, D. Turgis, B. Hermans, P. Jourand, R. Onclin, R. Puers, and K. U. Leuven, "A differential pressure approach to spirometry," *Conference Proceedings - IEEE Biomedical Circuits and Systems Conference Healthcare Technology, BiOCAS2007*, pp. 5–8, 2007.

[36] P. Sridevi, P. Kundu, T. Islam, C. Shahnaz, and S. A. Fattah, "A Low-cost Venturi Tube Spirometer for the Diagnosis of COPD," *IEEE Region 10 Annual International Conference, Proceedings/TENCON*, vol. 2018-Octob, no. October, pp. 723–726, 2019. Publisher: IEEE.

[37] J. X. Zhang, "Analysis on the effect of venturi tube structural parameters on fluid flow," *AIP Advances*, vol. 7, p. 065315, June 2017.

[38] M. Tsirlis and N. Michailidis, "Low-pressure gas atomization of aluminum through a Venturi nozzle," *Advanced Powder Technology*, vol. 31, no. 4, pp. 1720–1727, 2020. Publisher: Society of Powder Technology Japan.

[39] L. Latif and J. Macdonald, "Suction devices," *Anaesthesia and Intensive Care Medicine*, vol. 19, no. 1, pp. 16–19, 2018. Publisher: Elsevier Ltd.

[40] R. L. Wegel and R. R. Riez, "Measurement of the Constants of a Single Reed Wind Vibrator," *The Journal of the Acoustical Society of America*, vol. 1, no. 2A, pp. 171–171, 1930.

[41] K. M. Soto-Ruiz, W. F. Peacock, and J. Varon, "The men and history behind the venturi mask," *Resuscitation*, vol. 82, no. 3, pp. 244–246, 2011.

[42] P. Titheradge and R. Robergs, "Static and dynamic performance of a venturi airflow sensor," *Flow Measurement and Instrumentation*, vol. 73, no. July 2019, pp. 101725–101725, 2020. Publisher: Elsevier Ltd.

[43] V. Mitchell and K. Cheesman, "Gas, tubes and flow," *Anaesthesia and Intensive Care Medicine*, vol. 11, no. 1, pp. 32–35, 2010. Publisher: Elsevier Ltd.

[44] B. E. Rapp, "Fluids," in *Microfluidics: Modelling, Mechanics and Mathematics*, pp. 243–263, Elsevier, 2017.

[45] S. Cortés, D. Güemes, and R. Ávila, "Low Reynolds Number Flow Around a Flying Saucer Micro Air Vehicle," *COMSOL Conference*, pp. 1–7, 2013.

[46] M. R. Mhetre and H. K. Abhyankar, "Human exhaled air energy harvesting with specific reference to PVDF film," *Engineering Science and Technology, an International Journal*, vol. 20, no. 1, pp. 332–339, 2017. Publisher: Karabuk University.

[47] Hermann Schlichting, *Boundary Layer Theory*. New York: McGraw-Hill, 7 ed., 1979.

[48] N. D. Katopodes, *Viscous Fluid Flow*. 2019. Pages: 426 Publication Title: Free-Surface Flow.

[49] M. A. Russo, D. M. Santarelli, and D. O'Rourke, "The physiological effects of slow breathing in the healthy human," *Breathe*, vol. 13, pp. 298–309, Dec. 2017.

[50] Y. Zhai, Z. Wang, K. Kwon, S. Cai, D. J. Lipomi, and T. N. Ng, "Printing Multi-Material Organic Haptic Actuators," *Advanced Materials*, vol. 33, p. 2002541, May 2021.

[51] E. Mansour, R. Vishinkin, S. Rihet, W. Saliba, F. Fish, P. Sarfati, and H. Haick, "Measurement of temperature and relative humidity in exhaled breath," *Sensors and Actuators B: Chemical*, vol. 304, p. 127371, Feb. 2020.

[52] J. Azarnoosh, K. Sreenivas, and A. Arabshahi, "CFD Investigation of Human Tidal Breathing through Human Airway Geometry," *Procedia Computer Science*, vol. 80, pp. 965–976, 2016.

[53] J. D. Pleil, M. Ariel Geer Wallace, M. D. Davis, and C. M. Matty, "The physics of human breathing: flow, timing, volume, and pressure parameters for normal, on-demand, and ventilator respiration," *Journal of Breath Research*, vol. 15, p. 042002, Oct. 2021.

[54] J. J. Lofrese, C. Tupper, D. Denault, and S. L. Lappin, "Physiology, Residual Volume," in *StatPearls*, Treasure Island (FL): StatPearls Publishing, 2022.

[55] S. R, "The Peak Expiratory Flow Rate (PEFR): the Effect of Stress in a Geriatric Population of Chennai- A Pilot Study," *JOURNAL OF CLINICAL AND DIAGNOSTIC RESEARCH*, 2013.

[56] D. P. Johns, C. M. Ingram, S. Khov, P. D. Rochford, and E. H. Walters, "Effect of breathing circuit resistance on the measurement of ventilatory function," *Thorax*, vol. 53, pp. 944–948, Nov. 1998.

[57] Y. A. Çengel and J. M. Cimbala, *Fluid mechanics: fundamentals and applications*. New York, NY: McGraw-Hill Education, fourth edition ed., 2018.

[58] D. Filingeri, D. Fournet, S. Hodder, and G. Havenith, "Body mapping of cutaneous wetness perception across the human torso during thermo-neutral and warm environmental exposures," *Journal of Applied Physiology*, vol. 117, no. 8, pp. 887–897, 2014. PMID: 25103965.

[59] J. Dargahi and S. Najarian, "Human tactile perception as a standard for artificial tactile sensing—a review," *The International Journal of Medical Robotics and Computer Assisted Surgery*, vol. 1, no. 1, pp. 23–35, 2004.

[60] H. P. Saal and S. J. Bensmaia, "Touch is a team effort: interplay of submodalities in cutaneous sensibility," *Trends in Neurosciences*, vol. 37, no. 12, pp. 689–697, 2014.

[61] A. Handler and D. D. Ginty, "The mechanosensory neurons of touch and their mechanisms of activation," *Nature Reviews Neuroscience*, vol. 22, pp. 521–537, Sept. 2021.

[62] D. Filingeri and G. Havenith, "Human skin wetness perception: psychophysical and neurophysiological bases," *Temperature*, vol. 2, no. 1, pp. 86–104, 2015. PMID: 27227008.

[63] W. M. Bergmann Tiest, "Tactual perception of liquid material properties," *Vision Research*, vol. 109, pp. 178–184, 2015. Perception of Material Properties (Part I).

[64] C. Merrick, R. Rosati, and D. Filingeri, "The role of friction on skin wetness perception during dynamic interactions between the human index finger pad and materials of varying moisture content," *Journal of Neurophysiology*, vol. 127, no. 3, pp. 725–736, 2022. PMID: 35044853.

[65] M. Raccuglia, S. Hodder, and G. Havenith, "Human wetness perception in relation to textile water absorption parameters under static skin contact," *Textile Research Journal*, vol. 87, no. 20, pp. 2449–2463, 2017.

[66] M. Raccuglia, K. Pistak, C. Heyde, J. Qu, N. Mao, S. Hodder, and G. Havenith, "Human wetness perception of fabrics under dynamic skin contact," *Textile Research Journal*, vol. 88, no. 19, pp. 2155–2168, 2018.

[67] D. Filingeri, B. Redortier, S. Hodder, and G. Havenith, "Warm temperature stimulus suppresses the perception of skin wetness during initial contact with a wet surface," *Skin Research and Technology*, vol. 21, no. 1, pp. 9–14, 2015.

[68] D. Filingeri, B. Redortier, S. Hodder, and G. Havenith, "The role of decreasing contact temperatures and skin cooling in the perception of skin wetness," *Neuroscience Letters*, vol. 551, pp. 65–69, Sept. 2013.

[69] I. M. Bentley, "The Synthetic Experiment," *The American Journal of Psychology*, vol. 11, no. 3, pp. 405–425, 1900.

[70] W. M. Bergmann Tiest, N. D. Kosters, A. M. Kappers, and H. A. Daanen, "Haptic perception of wetness," *Acta Psychologica*, vol. 141, pp. 159–163, Oct. 2012.

[71] D. Filingeri, B. Redortier, S. Hodder, and G. Havenith, "Thermal and tactile interactions in the perception of local skin wetness at rest and during exercise in thermo-neutral and warm environments," *Neuroscience*, vol. 258, pp. 121–130, 2014.

[72] Y. Nonomura, T. Miura, T. Miyashita, Y. Asao, H. Shirado, Y. Makino, and T. Maeno, "How to identify water from thickener aqueous solutions by touch," *Journal of The Royal Society Interface*, vol. 9, pp. 1216–1223, June 2012.

[73] A. M. West, J. Tarrier, S. Hodder, and G. Havenith, "Sweat distribution and perceived wetness across the human foot: the effect of shoes and exercise intensity," *Ergonomics*, vol. 62, pp. 1450–1461, Nov. 2019.

[74] E. Jeon, S. Yoo, and E. Kim, "Psychophysical determination of moisture perception in high-performance shirt fabrics in relationtosweating level," *Ergonomics*, vol. 54, pp. 576–586, June 2011.

[75] H.-N. Ho, "Material recognition based on thermal cues: Mechanisms and applications," *Temperature*, vol. 5, pp. 36–55, Jan. 2018.

[76] G. Sennakesavan, M. Mostakhdemin, L. Dkhar, A. Seyfoddin, and S. Fatihhi, "Acrylic acid/acrylamide based hydrogels and its properties - A review," *Polymer Degradation and Stability*, vol. 180, p. 109308, Oct. 2020.

[77] P. Xu, C. Wang, B. Zhao, Y. Zhou, and H. Cheng, "A high-strength and ultra-stable halloysite nanotubes-crosslinked polyacrylamide hydrogel electrolyte for flexible zinc-ion batteries," *Journal of Power Sources*, vol. 506, p. 230196, Sept. 2021.

[78] R. Tong, G. Chen, D. Pan, H. Qi, R. Li, J. Tian, F. Lu, and M. He, "Highly Stretchable and Compressible Cellulose Ionic Hydrogels for Flexible Strain Sensors," *Biomacromolecules*, vol. 20, pp. 2096–2104, May 2019.

[79] Y. Wang and D. Li, "Creating Complex Polyacrylamide Hydrogel Structures Using 3D Printing with Applications to Mechanobiology," *Macromolecular Bioscience*, vol. 20, p. 2000082, July 2020.

[80] A. K. Denisin and B. L. Pruitt, "Tuning the Range of Polyacrylamide Gel Stiffness for Mechanobiology Applications," *ACS Applied Materials & Interfaces*, vol. 8, pp. 21893–21902, Aug. 2016.

[81] X. Zhou, C. Li, L. Zhu, and X. Zhou, "Engineering hydrogels by soaking: from mechanical strengthening to environmental adaptation," *Chemical Communications*, vol. 56, no. 89, pp. 13731–13747, 2020.

[82] S. Hirai and N. Miki, "A thermal tactile sensation display with controllable thermal conductivity," *Micromachines*, vol. 10, no. 6, 2019.

[83] M. F. Tritsch, "The veridical perception of object temperature with varying skin temperature," *Perception & Psychophysics*, vol. 43, pp. 531–540, Dec. 1988.

[84] K. O. Johnson, I. Darian-Smith, and C. LaMotte, "Peripheral neural determinants of temperature discrimination in man: a correlative study of responses to cooling skin.," *Journal of Neurophysiology*, vol. 36, pp. 347–370, Mar. 1973.

[85] C. Sarathchandran and S. Ilangovan, "Chapter 18 - carbon aerogels: Synthesis, properties, and applications," in *Handbook of Carbon-Based Nanomaterials* (S. Thomas, C. Sarathchandran, S. Ilangovan, and J. C. Moreno-Piraján, eds.), Micro and Nano Technologies, pp. 739–781, Elsevier, 2021.

[86] J. Meseguer, I. Pérez-Grande, and A. Sanz-Andrés, "10 - mechanical interfaces," in *Spacecraft Thermal Control* (J. Meseguer, I. Pérez-Grande, and A. Sanz-Andrés, eds.), pp. 157–173, Woodhead Publishing, 2012.

[87] G. B. Arfken, D. F. Griffing, D. C. Kelly, and J. Priest, "chapter 23 - heat transfer," in *International Edition University Physics* (G. B. Arfken, D. F. Griffing, D. C. Kelly, and J. Priest, eds.), pp. 430–443, Academic Press, 1984.

[88] M.-S. Kim, I.-Y. Kim, Y.-K. Park, and Y.-Z. Lee, "The friction measurement between finger skin and material surfaces," *Wear*, vol. 301, no. 1, pp. 338–342, 2013. Wear of Materials 2013.

[89] L. Jones and M. Berris, "The psychophysics of temperature perception and thermal-interface design," in *Proceedings 10th Symposium on Haptic Interfaces for Virtual Environment and Teleoperator Systems. HAPTICS 2002*, pp. 137–142, 2002.

[90] W. M. Bergmann Tiest and A. M. L. Kappers, "Tactile perception of thermal diffusivity," *Attention, Perception, & Psychophysics*, vol. 71, pp. 481–489, Apr. 2009.

[91] D. R. Kenshalo, C. E. Holmes, and P. B. Wood, "Warm and cool thresholds as a function of rate of stimulus temperature change," *Perception & Psychophysics*, vol. 3, pp. 81–84, Mar. 1968.

[92] S. Oss, "A simple model of thermal conduction in human skin: temperature perception and thermal effusivity," *European Journal of Physics*, vol. 43, p. 035101, feb 2022.

[93] M. Di Luca, ed., *Multisensory Softness: Perceived Compliance from Multiple Sources of Information*. Springer Series on Touch and Haptic Systems, London: Springer London, 2014.

[94] A. Pasqualotto, M. Ng, Z. Y. Tan, and R. Kitada, "Tactile perception of pleasantness in relation to perceived softness," *Scientific Reports*, vol. 10, p. 11189, July 2020.

[95] C. Dhong, R. Miller, N. B. Root, S. Gupta, L. V. Kayser, C. W. Carpenter, K. J. Loh, V. S. Ramachandran, and D. J. Lipomi, "Role of indentation depth and contact area on human perception of softness for haptic interfaces," *Science Advances*, vol. 5, p. eaaw8845, Aug. 2019.

[96] A. Metzger and K. Drewing, "Haptic aftereffect of softness," in *Haptics: Perception, Devices, Control, and Applications* (F. Bello, H. Kajimoto, and Y. Visell, eds.), (Cham), pp. 23–32, Springer International Publishing, 2016.

[97] M. A. Srinivasan and R. H. LaMotte, "Tactual discrimination of softness," *Journal of Neurophysiology*, vol. 73, pp. 88–101, Jan. 1995.

[98] E. P. Scilingo, M. Bianchi, G. Grioli, and A. Bicchi, "Rendering Softness: Integration of Kinesthetic and Cutaneous Information in a Haptic Device," *IEEE Transactions on Haptics*, vol. 3, pp. 109–118, Apr. 2010.

[99] Z. Shao, J. Wu, Q. Ouyang, C. He, and Z. Cao, "Multi-Layered Perceptual Model for Haptic Perception of Compliance," *Electronics*, vol. 8, p. 1497, Dec. 2019.

[100] A. M. Kappers and W. M. Bergmann Tiest, "Haptic perception," *WIREs Cognitive Science*, vol. 4, pp. 357–374, July 2013.

[101] L. Cacopardo, N. Guazzelli, R. Nossa, G. Mattei, and A. Ahluwalia, "Engineering hydrogel viscoelasticity," *Journal of the Mechanical Behavior of Biomedical Materials*, vol. 89, pp. 162–167, 2019.

[102] A. Huang, Y. Bao, H. Li, Y. Liu, X. Zheng, and G. Qin, "Thermal conductivity of ethylene glycol and water binary mixtures at evaluated temperature and pressure," *The Journal of Chemical Thermodynamics*, vol. 175, p. 106900, Dec. 2022.

[103] N. Tang, Z. Peng, R. Guo, M. An, X. Chen, X. Li, N. Yang, and J. Zang, "Thermal Transport in Soft PAAm Hydrogels," *Polymers*, vol. 9, p. 688, Dec. 2017.

[104] D. J. Navarick and E. Fantino, "Stochastic transitivity and unidimensional behavior theories.," *Psychological Review*, vol. 81, p. 426–441, Sep 1974.

[105] R. Luce, "The choice axiom after twenty years," *Journal of Mathematical Psychology*, vol. 15, no. 3, pp. 215–233, 1977.

[106] A. Springall, "Response Surface Fitting Using a Generalization of the Bradley-Terry Paired Comparison Model," *Journal of the Royal Statistical Society Series C: Applied Statistics*, vol. 22, pp. 59–68, Dec. 2018. _eprint: https://academic.oup.com/jrsssc/article-pdf/22/1/59/48612586/jrsssc_22_1_59.pdf.

[107] K. P. Burnham and D. R. Anderson, "Multimodel inference: Understanding aic and bic in model selection," *Sociological Methods & Research*, vol. 33, no. 2, pp. 261–304, 2004.

[108] D. Filingeri, B. Redortier, S. Hodder, and G. Havenith, "Warm temperature stimulus suppresses the perception of skin wetness during initial contact with a wet surface," *Skin Research and Technology*, vol. 21, no. 1, pp. 9–14, 2015.

[109] A. C. Bento, N. Cella, S. M. Lima, L. A. Nunes, L. H. Andrade, J. R. Silva, V. S. Zanuto, N. G. Astrath, T. Catunda, A. N. Medina, J. H. Rohling, R. F. Muniz, J. W. Berrar, L. C. Malacarne, W. R. Weinand, F. Sato, M. P. Belancon, G. J. Schiavon, J. Shen, L. C. Miranda, H. Vargas, and M. L. Baesso, "Photoacoustic and photothermal and the photovoltaic efficiency of solar cells: A tutorial," *Journal of Applied Physics*, vol. 131, 4 2022.

[110] F. Giorgianni, C. Vicario, M. Shalaby, L. D. Tenuzzo, A. Marcelli, T. Zhang, K. Zhao, Y. Chen, C. Hauri, and S. Lupi, "High-efficiency and low distortion photoacoustic effect in 3d graphene sponge," *Advanced Functional Materials*, vol. 28, 1 2018.

[111] K. L. Muratikov, A. L. Glazov, D. N. Rose, and J. E. Dumar, "Photoacoustic effect in stressed elastic solids," *Journal of Applied Physics*, vol. 88, pp. 2948–2955, 9 2000.

[112] I. Steinberg, D. M. Huland, O. Vermesh, H. E. Frostig, W. S. Tummers, and S. S. Gambhir, "Photoacoustic clinical imaging," *Photoacoustics*, vol. 14, pp. 77–98, 6 2019.

[113] A. B. E. Attia, G. Balasundaram, M. Moothanchery, U. S. Dinish, R. Bi, V. Ntziachristos, and M. Olivo, "A review of clinical photoacoustic imaging: Current and future trends," *Photoacoustics*, vol. 16, 12 2019.

[114] D. Das, A. Sharma, P. Rajendran, and M. Pramanik, "Another decade of photoacoustic imaging," *Physics in Medicine and Biology*, vol. 66, 3 2021.

[115] L. V. Wang and J. Yao, "A practical guide to photoacoustic tomography in the life sciences," *Nature Methods*, vol. 13, pp. 627–638, 7 2016.

[116] G. Ku, X. Wang, G. Stoica, and L. V. Wang, "Multiple-bandwidth photoacoustic tomography," *Physics in Medicine and Biology*, vol. 49, pp. 1329–1338, 4 2004.

[117] T. Agano, M. Kuniyil Ajith Singh, R. Nagaoka, and K. Awazu, "Effect of light pulse width on frequency characteristics of photoacoustic signal-an experimental study using a pulse-width tunable led-based photoacoustic imaging system," *International Journal of Engineering and Technology*, vol. 7, pp. 4300–4303, 12 2018.

[118] S. W. Cho, S. M. Park, B. Park, D. Y. Kim, T. G. Lee, B. M. Kim, C. Kim, J. Kim, S. W. Lee, and C. S. Kim, "High-speed photoacoustic microscopy: A review dedicated on light sources," *Photoacoustics*, vol. 24, 12 2021.

[119] M. Erfanzadeh and Q. Zhu, "Photoacoustic imaging with low-cost sources; a review," *Photoacoustics*, vol. 14, pp. 1–11, 2019.

[120] L. Lin and L. V. Wang, "The emerging role of photoacoustic imaging in clinical oncology," *Nature Reviews Clinical Oncology*, vol. 19, pp. 365–384, June 2022.

[121] R. Gao, Z. Xu, Y. Ren, L. Song, and C. Liu, "Nonlinear mechanisms in photoacoustics—powerful tools in photoacoustic imaging," *Photoacoustics*, vol. 22, p. 100243, 2021.

[122] P. K. Upputuri and M. Pramanik, "Fast photoacoustic imaging systems using pulsed laser diodes: a review," *Biomedical Engineering Letters*, vol. 8, pp. 167–181, 5 2018.

[123] S. Rajagopal and B. T. Cox, "Modelling laser ultrasound waveforms: The effect of varying pulse duration and material properties," *The Journal of the Acoustical Society of America*, vol. 149, pp. 2040–2054, 3 2021.

[124] S. Qu and K. Nakamura, "Selection of laser pulse width for efficient generation of photoacoustic signals in liquid-filled thin capillary embedded in soft material," *AIP Advances*, vol. 11, 6 2021.

[125] N. Cao, Y. Li, R. Zhang, S. Liu, Y. Xiong, and H. Cao, "Theoretical analysis of photoacoustic effects in a multilayered skin tissue model," *AIP Advances*, vol. 13, 3 2023.

[126] I. J. Bigio and S. Fantini, *Photoacoustic Imaging*, p. 526–532. Cambridge University Press, 2016.

[127] F. Gao, X. Feng, R. Zhang, S. Liu, R. Ding, R. Kishor, and Y. Zheng, "Single laser pulse generates dual photoacoustic signals for differential contrast photoacoustic imaging," *Scientific Reports*, vol. 7, p. 626, Apr. 2017.

[128] L. A. Jones and A. M. Smith, "Tactile sensory system: Encoding from the periphery to the cortex," *Wiley Interdisciplinary Reviews: Systems Biology and Medicine*, vol. 6, pp. 279–287, 2014.

[129] A. Handler and D. D. Ginty, "The mechanosensory neurons of touch and their mechanisms of activation," *Nature Reviews Neuroscience*, vol. 22, pp. 521–537, 9 2021.

[130] G. S. Harrington and J. H. D. III, "Fmri mapping of the somatosensory cortex with vibratory stimuli is there a dependency on stimulus frequency?," 2001.

[131] C. P. Ryan, G. C. Bettelani, S. Ciotti, C. Parise, A. Moscatelli, and M. Bianchi, "The interaction between motion and texture in the sense of touch," *Journal of Neurophysiology*, vol. 126, pp. 1375–1390, 10 2021.

[132] S. Gupta, D. Morris, S. N. Patel, and D. Tan, "Airwave," pp. 419–428, ACM, 9 2013.

[133] D. J. Meyer, M. Wiertlewski, M. A. Peshkin, and J. E. Colgate, "Dynamics of ultrasonic and electrostatic friction modulation for rendering texture on haptic surfaces," pp. 63–67, IEEE, 2 2014.

[134] D.-B. Vo and S. A. Brewster, "Touching the invisible: Localizing ultrasonic haptic cues," pp. 368–373, IEEE, 6 2015.

[135] G. Reardon, B. Dandu, Y. Shao, and Y. Visell, "Shear shock waves mediate haptic holography via focused ultrasound," *Science Advances*, vol. 9, 3 2023.

[136] L. Arendt-Nielsen and P. Bjerring, "Laser-induced pain for evaluation of local analgesia: A comparison of topical application (emla) and local injection (lidocaine)," *Anesthesia Analgesia*, vol. 67, 1988.

[137] C. E. Moore and W. Schady, "Cutaneous localisation of laser induced pain in humans," *Neuroscience Letters*, vol. 193, pp. 208–210, 7 1995.

[138] H.-S. Kim, K. B. Kim, J.-H. Lee, J.-J. Jung, Y.-J. Kim, S.-P. Kim, M.-H. Choi, J.-H. Yi, and S.-C. Chung, "Mid-air tactile sensations evoked by laser-induced plasma: A neurophysiological study," *Frontiers in Neuroscience*, vol. 15, 10 2021.

[139] A. I. Weber, H. P. Saal, J. D. Lieber, J.-W. Cheng, L. R. Manfredi, J. F. Dammann, and S. J. Bensmaia, "Spatial and temporal codes mediate the tactile perception of natural textures," *Proceedings of the National Academy of Sciences*, vol. 110, no. 42, pp. 17107–17112, 2013.

[140] J. Dargahi and S. Najarian, "Human tactile perception as a standard for artificial tactile sensing - a review," *International Journal of Medical Robotics and Computer Assisted Surgery*, vol. 01, p. 23, 2004.

[141] M. B. Reinhart, C. R. Huntington, L. J. Blair, B. T. Heniford, and V. A. Augenstein, "Indocyanine green :historical context, current applications, and future considerations," *Surgical Innovation*, vol. 23, pp. 166–175, 4 2016.

[142] Z. Starosolski, R. Bhavane, K. B. Ghaghada, S. A. Vasudevan, A. Kaay, and A. Annapragada, "Indocyanine green fluorescence in second near-infrared (nir-ii) window," *PLoS ONE*, vol. 12, 11 2017.

[143] G. Corniani and H. P. Saal, "Tactile innervation densities across the whole body," *REVIEW — Sensory Processing J Neurophysiol*, vol. 124, pp. 1229–1240, 2020.

[144] P. L. MacDonald and R. C. Gardner, "Type i error rate comparisons of post hoc procedures for i j chi-square tables," *Educational and Psychological Measurement*, vol. 60, no. 5, pp. 735–754, 2000.

[145] J. Ciano and B. L. Beatty, "Regional variation in the density of meissner's corpuscles in human fingers," *Annals of Anatomy*, vol. 243, 8 2022.

[146] D.-H. Kim, P. K. Wong, J. Park, A. Levchenko, and Y. Sun, "Microengineered platforms for cell mechanobiology," *Annual Review of Biomedical Engineering*, vol. 11, no. 1, pp. 203–233, 2009. PMID: 19400708.

[147] F. Melo-Fonseca, O. Carvalho, M. Gasik, G. Miranda, and F. S. Silva, "Mechanical stimulation devices for mechanobiology studies: a market, literature, and patents review," vol. 6, no. 3, pp. 340–371.

[148] L. T. DeCarlo, "Signal detection theory and generalized linear models.," *Psychological Methods*, vol. 3, no. 2, pp. 186–205, 1998. Place: US Publisher: American Psychological Association.

[149] C. J. Clopper and E. S. Pearson, "The use of confidence or fiducial limits illustrated in the case of the binomial," *Biometrika*, vol. 26, no. 4, pp. 404–413, 1934.

[150] M. J. Hacker and R. Ratcliff, "A revised table of d' for M-alternative forced choice," *Perception & Psychophysics*, vol. 26, pp. 168–170, Mar. 1979.